CONSTRUCTION AND TESTING OF A LOW TEMPERATURE DIFFERENTIAL STIRLING ENGINE FOR POWER GENERATION 2

A thesis submitted in partial fulfilment of the requirements for the Degree

of Master of Engineering

in the University of Canterbury

by P. A. Postles

University of Canterbury

2015

ABSTRACT

This thesis presents the design and construction of a low temperature differential (LTD) Stirling engine for electric power generation. The target energy sources were geothermal, industrial waste heat or solar heated water. These sources would supply a source temperature of around 90 °C. Assuming that the sink is kept at around 20 °C, the engine was designed based on a temperature difference of approximately 70 °C. The initial design and basic structure of the engine was completed in a previous project utilising first order design methods. The goal was to develop a low cost prototype engine capable of producing up to 500W electrical output power. A novel gamma type engine was proposed utilising a rotary reciprocating displacer and industrial steam piping to form a low cost pressurised chamber. This project concentrated on advancing the design and construction towards completion with particular emphasis on the electrical control, measurement/instrumentation components, and gas flow through the regenerator.

At the completion of this project the displacer piston actuation system has been redesigned. In order to achieve the displacer's specified $2\,Hz$ actuation, both the displacer's structure and the actuation system were altered. The displacer's aluminium shell and foam centre were removed and replaced with a pine superstructure coated in depron foam, reducing the moment of inertia from $0.4488\,kg \cdot m^2$ to $0.0984\,kg \cdot m^2$. A secondary motor was added to the actuation system to increase the actuation power. The gearing ratio was also altered from 10:1 to 2:1 to increase the peak displacer speed.

The regenerator was designed and built to suit the unusual wedge shape requirements of the original design. A ribbed structure was conceived to allow fluid flow to be manipulated within separate sections, producing an even pressure drop over varying regenerator lengths. Simulations were run to optimise both the number of sections and the mass of wire wool to be placed in each segment. The final regenerator design has axial ribs placed at radii of 93, 134, 192, 276 and 392mm, creating four sections. These sections are filled with 0.68, 0.97, 1.40 and 1.90kg of #0 mild steel wire wool.

As Stirling engines are not self-starting the generator was required to be run as a motor when starting the Stirling engine. To achieve bidirectional flow of current within the starter motor/generator control system, a field oriented control (FOC) inverter from Texas Instruments was purchased and set up to run the 1kW, 3 phase, permanent magnet generator in both motor and generation modes. This will allow the Stirling engine to be brought up to speed with the generator operating as a motor and then switch to generation mode when the motoring current falls below a set limit.

Both pressure and temperature measurement systems were developed, constructed and tested in order to collect information about the performance of the engine under operation. Three pressure transducer circuits were designed and constructed with measurement ranges of $10\ kPa$, $\pm 0.99\ kPa$ and $\pm 6.66\ kPa$. These circuits were integrated with a PiocLog1012 analog to digital converter and PicoLog recording software. Eight K-type thermocouples were used for temperature recording. These were sampled with a Pico Technology TC-08 temperature thermocouple data logger which in turn was connected, via USB, to a computer running PicoLog Recorder software.

Thus far all component testing has been carried out with test rigs that model the relevant parts of the engine. The displacer actuation system and phase angle control of the displacer and power piston has been tested. Temperature and pressure measurement systems have been independently tested. Motor/generator speed control and switching has been simulated and tested. Unfortunately completion of the engine assembly was not achieved within the scope of this project and therefore fully integrated testing of all components was not carried out. Once mechanical assembly is completed fully integrated testing of displacer actuation, piston position, generator speed control and measurement systems can be achieved.

CONTENTS

LIST OF FIGURES

LIST OF TABLES

NOMENCLATURE

Symbol	Description	Units
A_{ff}	Cross−sectional flow area	m^2
a	Wire radius	m
α	Friction factor coefficient	
B_n	Beale number	
C	Inertial coefficient	
C_p	Specific heat at constant pressure	$J/kg \cdot K$
C_v	Specific heat at constant volume	$J/kg \cdot K$
C_1	Regenerator geometric parameter	
C_2	Regenerator geometric parameter	
d_h	Hydraulic diameter	m
δ	Friction factor coefficient	
f_k	Matrix friction factor	
f	Engine operating frequency	Hz
H_r	Height of the regenerator	m
h	Convective heat transfer coefficient	$W/m^2 \cdot K$
K	Regenerator permeability	m^2
$k_p = V_p/V_d$	Swept volume ratio	
$k_s = V_s/V_d$	Dead space volume ratio	
L	Length of regenerator	m
m	Mass of working fluid	kg
M	Mass flow rate per second	Kg/s
M_o	Mass flow rate	kg
M_{wire}	Wire mass	kg
n	Number of moles	
N_{re}	Reynolds number	
N_{reK}	Permeability based Reynolds number	
N_{pr}	Prandtl number	
NTU	Number transfer units	
η	Engine efficiency	%

η_{max}	Maximum Stirling cycle efficiency	%
η_{carnot}	Carnot efficiency	%
η_{reg}	Regenerator effectiveness	
P	Mean or average cycle pressure	N/m^2, bar
P_{max}	Maximum pressure attained during cycle	N/m^2
P_o	Engine shaft power output	W
ρ_{wire}	Density of regenerator packing material	kg/m^3
P_{drop}	Pressure drop	Pa
ρ	Density of working fluid	kg/m^3
ρ_{wire}	Wire density	kg/m^3
P_{loss}	Power loss	W
dp/dx	Pressure drop per unit length	Pa
q_{in}	Heat input or useful input energy	J
q_{loss}	Extra heat required to overcome losses	J
R	Ideal gas constant	
R_h	Hydraulic radius	m
S_{reg}	Heat transfer surface area of regenerator	m^2
T_H	The hot space working fluid temperature	K
T_C	The cold space working fluid temperature	K
T	Temperature of working fluid	K
μ	Dynamic viscosity of the working fluid	$kg/m \cdot s$
V	Volume	m^3
V_d	Displacer swept volume	m^3
V_p	Power piston swept volume	m^3
V_s	Dead space volume	m^3
V_e	Expansion space volume	m^3
V_{reg}	Volume of the regenerator	m^3
v	Working fluid velocity	m/s
V_{max}	Maximum working fluid volume	m^3
V_{min}	Minimum working fluid volume	m^3
W	Work produced per cycle	Nm
W_{net}	Net indicated work per cycle	Nm

$W_{Schmidt}$	Indicated work per cycle using Schmidt analysis	Nm
W_{rs}	Width of regenerator segment	m
γ	Friction factor coefficient	
$\emptyset$	Regenerator porosity	$\%$
$\emptyset_c$	Porosity percolation threshold	

ACRONYMS AND ABBREVIATIONS

Acronym	Expansion
LTD	Low temperature differential
CHP	Combined heat and power
GHG	Greenhouse gas
IPCC	Intergovernmental Panel on Climate Change
AR5	Fifth assessment report
UNFCCC	United Nations Framework Convention on Climate Change
GMST	Global mean surface temperature
ORC	Organic Rankine cycle
PTFE	Polytetrafluorethylene
TDC	Top dead centre
BDC	Bottom dead centre
con-rod	Connecting rod
AMS	Advanced Micro Systems
NV	Non-volatile
EEPROM	Electrically erasable programmable read only memory
IO	Input/output
dc	Direct current
PVC	polyvinyl chloride
PMSM	Permanent magnet synchronous motor
FOC	Field oriented control
TI	Texis Instruments
CCS	Code Composer Studio
VSD	Variable speed drive
PWM	Pulse width modulation
PI	Proportional integral
MOSFET	Metal oxide semiconductor field effect transistor
ADC	Analog to digital converter
IR	Infrared
NPT	National pipe thread
LED	Light emitting diode

1. INTRODUCTION

1.1 MOTIVATION

One of the major challenges facing humanity in the next few generations is the stabilisation of the Earth's climate by controlling anthropogenic greenhouse gas (GHG) emissions. Ice core samples show that the concentration of carbon dioxide in the atmosphere over the past 400,000 years has not surpassed $300\,ppm$ and yet since the beginning of the industrial revolution the amount of CO_2 in the atmosphere has risen to nearly $400\,ppm$ [1]. According to the Intergovernmental Panel on Climate Change's (IPCC) fifth assessment report (AR5) "It is extremely likely that human activities caused more than half of the observed increase in GMST (global mean surface temperature) from 1951 to 2010." [2]. In general the effects of unabated GHG emissions include increased climate related weather extremes such as, heat waves, floods, droughts, cyclones, snow storms and wildfires, as well as coastal flooding, erosion and ocean acidification. These events have the potential to impact both natural ecosystems and human systems. Despite recent initiatives such as the Kyoto protocol and United Nations Framework Convention on Climate Change (UNFCCC) emissions are still increasing. Since the year 2000 GHG emissions have grown at a rate of 2.2% per year [3].

IPCC AR5 determines that the energy sector is the biggest producer of GHG emissions, contributing 35% of the total anthropogenic emissions in 2010. This figure includes all energy extraction, conversion, storage, transmission, and distribution processes. Due to the low efficiency of conversion (just 37% for fossil fuel to electricity [4]), the supply sector itself is the largest energy user. To reduce the effects of climate change, the rate at which anthropogenic GHG is emitted must be reduced. Vast improvements could be made by reducing the demand for power with energy efficient devices, as well as increased efficiency of fuel extraction and energy conversion, transmission and distribution [4]. In the long term however, it seems the most promising course of action is to invest in the development of low GHG technologies such as nuclear, wind, hydro, solar and geothermal electricity generation.

1.1 LOW ENTHALPY POWER GENERATION

Geothermal energy has many advantages as a renewable resource. Estimates of worldwide electricity generating potential of geothermal energy vary from 1.5 to $60\,TW$ [5]. The electricity output from geothermal power plants provides a very stable base load power source; this complements the intermittent supply renewable energy sources such as wind and solar produce. Binary cycle plants also have very low carbon emissions and a relatively small plant footprint [6]. Globally about $530\,MW$ of geothermal power came online in 2013 to bring the global installed capacity to just over $12{,}000\,MW$. This constituted a net capacity growth of 4% compared to an average annual growth rate of 3% for the two previous years (2010–12) [7]. With advances in technology lower temperature geothermal energy sources can be utilised to produce clean sustainable electricity.

Currently the main technology used to produce electricity from low enthalpy geothermal sources is the Binary cycle [8]. There are two main technologies that utilise this cycle, the organic Rankine cycle (ORC) and the Kalina cycle. A basic representation of the ORC is depicted in Figure 1.1 [8]. This cycle can utilise geothermal water with a temperature in the range of 75 to 150°C. The geothermal water is pumped through an evaporator, as shown in Figure 1.1 ①. This transfers the heat into an organic working fluid, such as isobutene or isopentane, through the use of a heat exchanger. Because the working fluid has a lower boiling temperature than water it transitions into a high pressure vapour. The working fluid is then expanded through a turbine which powers a generator to produce electricity (Figure 1.1 ②). The gaseous working fluid is then passed through another heat exchanger, called a condenser, as shown in Figure 1.1 ③. This cools the working fluid below its boiling temperature and it condenses back into a liquid form. A pump then transfers the working fluid back to the evaporator (Figure 1.1 ④), and the cycle repeats.

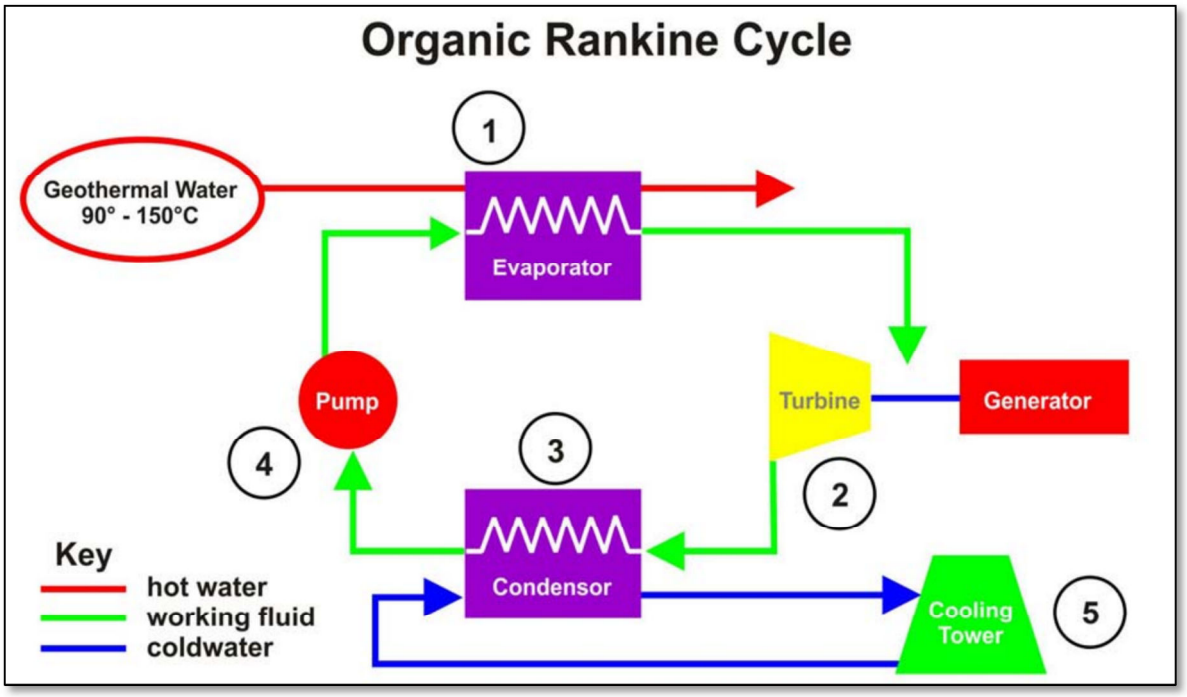

Figure 1.1: General configuration of an organic Rankine cycle power station [8]

The Kalina cycle is a more recent technology with up to 40% increase in the conversion efficiency over the ORC under certain operating conditions [9]. This efficiency is achieved by utilising a mixture of two working fluids, most commonly water and ammonia. By manipulating the concentration of the working fluids at different stages of the cycle and utilising heat recovery. The Kalina cycle also provides more flexibility of working temperatures because of the ability to adjust the concentrations of the working fluids. Despite being the dominant technology for low enthalpy power generation, a 2013 review shows that the average conversion efficiency of binary plants operating with inlet temperatures of less than $135°C$ was 2.5%, as shown by Figure 1.2.

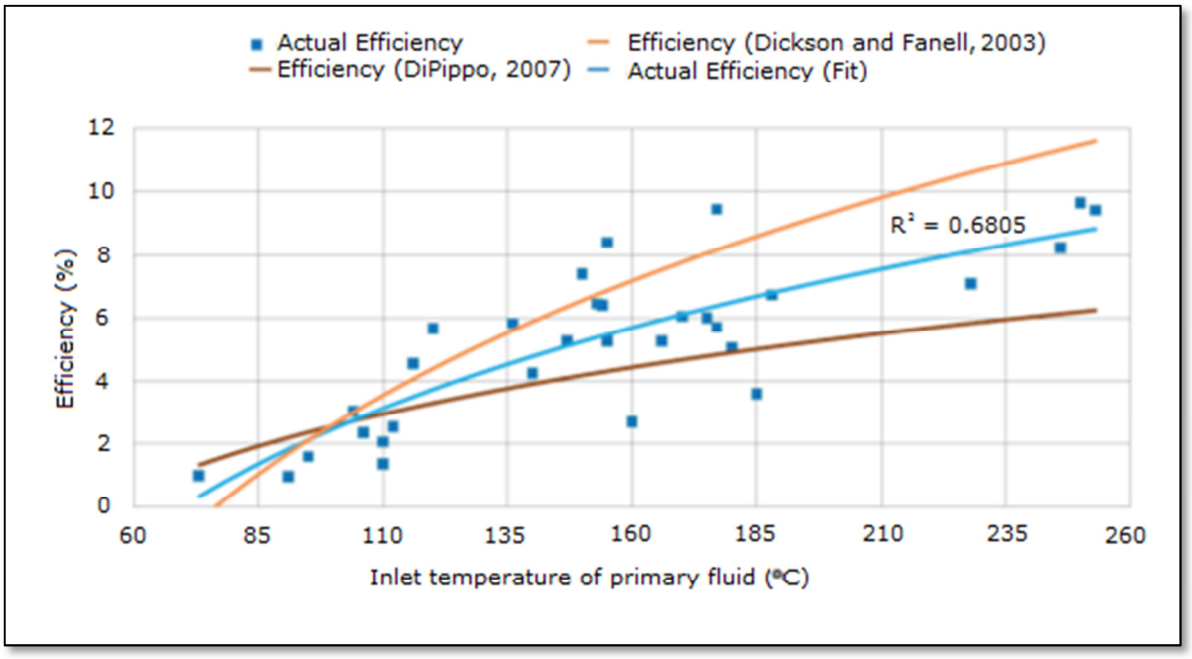

Figure 1.2: Calculated conversion efficiency of active binary geothermal power stations for given inlet temperature [10]

The main limitation of binary cycle power plants is the capital costs involved. Estimates place the capital cost of binary developments at between 1500 and 5900 USD/kW_e [11, 12]. These capital costs are generally made up of $10-15\%$ exploration and resource confirmation costs, $20-35\%$ drilling costs, $10-20\%$ surface facilities costs, and $40-60\%$ power plant costs [11]. This means that the plant payback time can range from 6-13 years depending on electricity prices [12]. Stirling engine technology may provide a lower cost alternative, especially for low enthalpy geothermal resources. Both Stirling and binary technologies have the potential to reach similar levels of efficiency [13], however it has been estimated that the plant footprint of Stirling power unit would be significantly smaller than that of a corresponding ORC unit [13], and therefore plant costs could be reduced.

1.2 Concept

The concept for this project was to evaluate the feasibility of using low temperature differential （LTD） Stirling engines for electric power production, or combined heat and power （CHP） systems, through the use of a prototype design. The Stirling engine utilises a difference in temperature to expand and contract a working gas and produce mechanical output power. One of the main advantages of the Stirling engine is that it can run off

multiple fuels without reconfiguration. Such sources include solar-thermal arrays, geothermal heat and industrial waste heat. Stirling engines also have the potential to be a low cost, and low level technology which can reduce capital costs and simplify maintenance requirements. A previous Masters project completed the design and manufacture of many of the engine components [14]. This project continues the design and construction of the engine with a particular focus on the electrical actuation, control and instrumentation, and regenerator gas flow aspects.

Chapter 2 will cover the background, including theory, basic operating principals of the Stirling engine and the design developed in a previous project. Chapter 3 will describe the design and implementation of the displacer and displacer actuation system. Chapter 4 will outline the regenerator design and construction. Chapter 5 will cover the design and testing of the generator setup. Chapter 6 will describe the instrumentation setup and testing. Chapter 7 will outline the general assembly of the prototype engine and the testing undertaken to validate the concept. Chapter 8 discusses issues discovered throughout the design and build process, as well as potential obstacles to completion. Chapter 9 summarises and states conclusions on the present state of completion of all components included in this project.

2. BACKGROUND

This chapter outlines the basic operating principals of the Stirling engine. Section 1.1 includes an explanation of the thermodynamic cycle utilised by Stirling engines. The basic engine components and the purpose of each are described in section 1.2. Section 1.3 outlines the three main engine classifications, alpha, beta and gamma, including a description of the operating cycle of each. The theoretical power produced and efficiency limits are discussed in section 1.4, as well as real output power estimation techniques. The major characteristics of the LTD are outlined in section 1.5; including techniques for improving power output and four examples of existing larger scale LTD Stirling engines. Finally the design of the engine for this project is described in section 1.6, including all major components.

2.1 THEORY

The Stirling engine is a type of heat engine; this means that its energy source is a difference in temperature from one side of the engine to the other. One great advantage of this is that it does not matter how the temperature difference is created. Stirling engines can therefore be run from many fuel sources, leading to their characterisation as a multi fuel engine. The Stirling engine is also characterised as a closed cycle engine because the working fluid is sealed inside. No fuel or working fluid physically enters or leaves the engine and therefore there is no need for valves or injectors. It is additionally characterised as an external combustion engine because the fuel source is external to the working fluid cylinder and the energy is transmitted to the working fluid via heat transfer through the engine wall or through heat exchangers [15].

When thought of intuitively, a Stirling engine works in the following manner. There are four distinct processes that make up a single cycle of the engine; these consist of heating, expansion, cooling and compression. The working fluid (gas) is heated from an initial colder temperature, generally characterised as T_C, to a higher temperature T_H. This causes an increase in pressure and an expansion of the working fluid producing usable work, which can be converted into mechanical work via movement of a power piston. The

working fluid is then cooled back down from T_H to T_C and compressed back to its original volume (with the reverse movement of the power piston), thus the process can be repeated. The heating and cooling of the working gas is achieved through bulk movement of the gas over heat exchanging surfaces, which is carried out by other mechanical elements of the engine (detailed in the following sections of this Chapter).

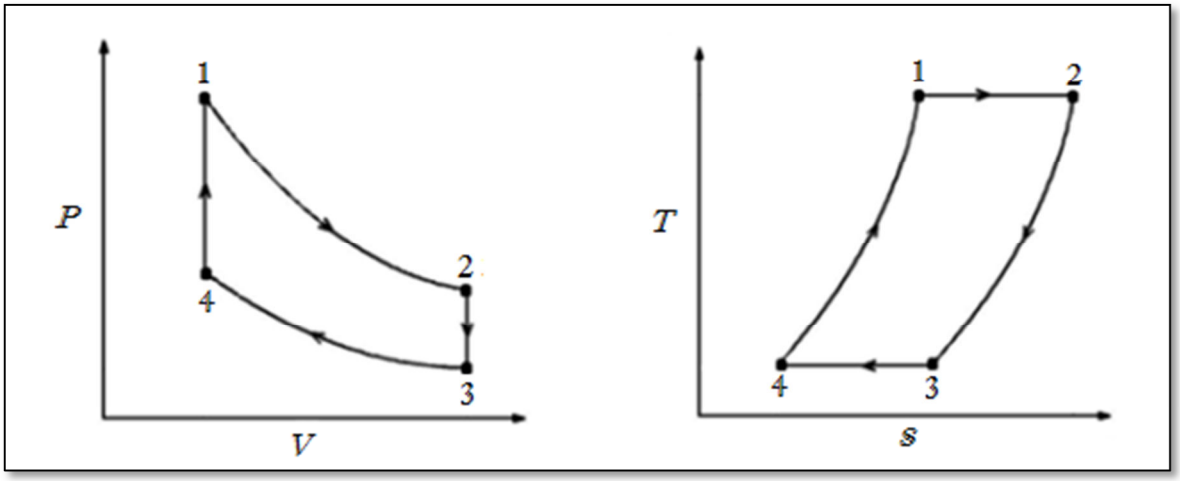

Figure 2.1: Pressure verses volume (left) and temperature verses entropy (right) for the idealised Stirling cycle [16]

Figure 2.1 is generally provided to illustrate the idealised Stirling cycle [16]. The illustration on the left is a $p-V$ plot, where p is the gas pressure and V is the total gas volume. The illustration on the right is a $T-s$ plot, where T is the gas temperature, and s is the gas entropy. There are two Isochoric processes and two Isothermal processes which form a closed loop. An Isochoric process, or constant volume process, is a thermodynamic process that takes place in a closed system during which the volume remains constant. An Isothermal process is a process during which the temperature remains constant throughout. Transition 4→1 in Figure 2.1 represents an isochoric addition; this is where the working fluid is heated from T_C to T_H, increasing in pressure whilst maintaining a constant volume (no movement of the power piston). Transition 1→2 represents an isothermal expansion; this is where the working fluid is in contact with the hot side and remains at a constant hot temperature whilst its volume expands (power piston moves to allow expansion). Transition 2→3 is an isochoric removal; in this process the working fluid flows from the hot to the cold side, decreasing in temperature while maintaining a constant volume (power piston is again stationary, but at the expanded position). Transition 3→4 is an

isothermal compression; this is where the working fluid is at the cold side and remains at the cold temperature as the fluid is compressed (power piston moves back to allow compression).

2.2 Engine components

Although many engine configurations are possible, most contain many of the same basic components. This section briefly describes the purpose of each component and lists some of the major operating characteristics. The engine components described below are illustrated with reference to Figure 2.2, the Stirling engine design which is the subject of this thesis. Full details of the original design may be found in section 2.6 Lloyd's Engine Design.

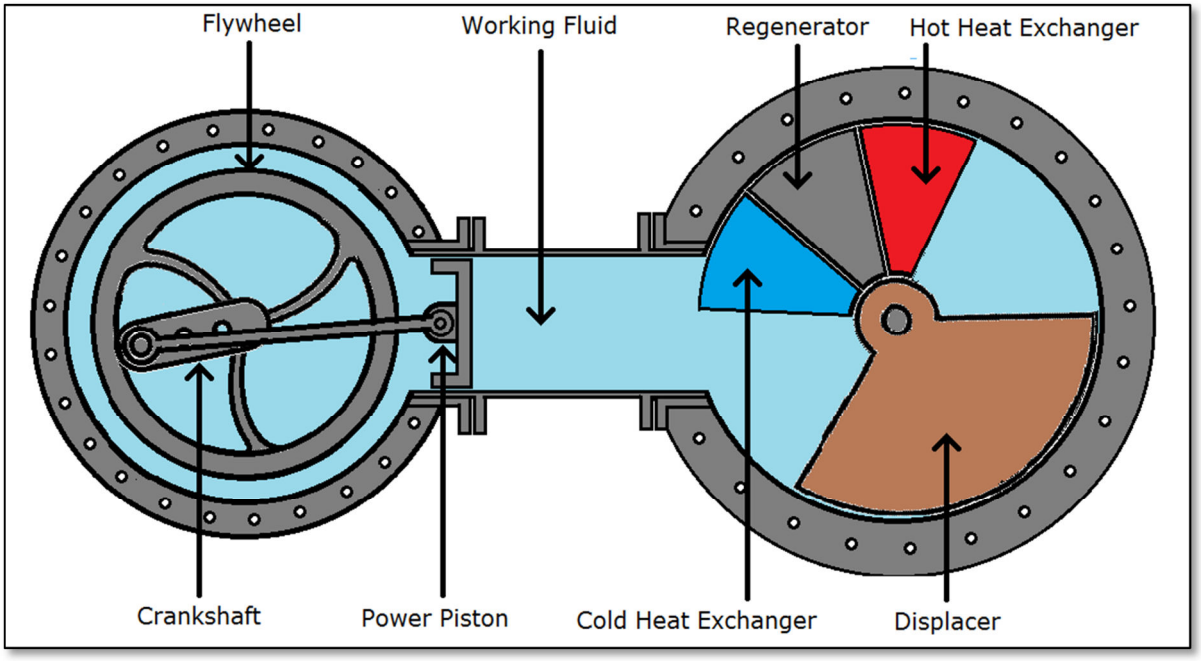

Figure 2.2: Basic engine components for Lloyd's engine design [14]

2.2.1 Displacer

The displacer is a type of piston which shifts the working fluid back and forth between the hot and cold spaces within the engine at the appropriate time [17]. This is achieved by displacing the fluid from the volume it occupies to any unoccupied space within the engine. The displacer does not need to be tightly sealed against the cylinder wall as it is only required to overcome the pressure associated with forcing the working fluid through the heat exchangers and regenerator. Its position is generally controlled by a physical

connection to the same flywheel shaft as the power piston, with around ninety degrees phase advance. It should be made of a thermally insulating material in order to prevent thermal conduction between the hot and cold regions of the engine. It must also be lightweight so that energy is not wasted by overcoming its inertia when changing direction at the end of each stroke. Some engine configurations require the displacer to be tolerant of high temperatures. Conventional displacers work like conventional pistons, displacing the working fluid by vertical movement within a cylinder. The displacer shown in Figure 2.2 instead works with a back and forth (reciprocating) rotation within a cylinder.

2.2.2 REGENERATOR

The regenerator is one of the most important parts of the engine for maximising efficiency [18]. Its role is to store the thermal energy from the working fluid as it flows from the hot side to the cold side and return it to the working fluid as it flows back from the cold to hot side. The more efficiently this can be done, the less heat energy is required from the heat source per cycle, and consequently the more efficient the engine will be [18]. The regenerator is typically constructed of tightly packed metal screens. The high heat capacity and fast heat transfer properties of metal enable efficient heat transfer characteristics. The screen arrangement also helps to prevent thermal conduction through the regenerator.

2.2.3 POWER PISTON

The power piston captures the energy exerted by the expanding working fluid and converts it into usable mechanical work. It must be tightly sealed against the cylinder wall so that no fluid leaks past, but at the same time it must not create too much friction which would reduce efficiency. A lubricant can be used to reduce the dynamic friction between the piston seal and chamber wall, however it has proved difficult to prevent the lubricant getting past the piston seal and into the working fluid chamber [18]. If this occurs problems are caused by the lubricant coating the regenerator material and heat exchanger surfaces, reducing their heat transfer effectiveness and increasing fluid friction losses. The most common piston seal is a material called Rulon, a glass fibre reinforced polytetrafluorethylene (PTFE) substance [18]. Rulon has an extremely low dynamic friction

and is very hard wearing, meaning it can be run without, or with very little lubrication. This extends the service interval of both the piston rings and the regenerator whilst maintaining efficient operation.

2.2.4 Working Fluid

The most common working fluids (all in gas form) are air, nitrogen, helium and hydrogen [19] [13]. The important characteristics of a working fluid are specific heat capacity, thermal conductivity, density and viscosity. Ideally the fluid will have a high thermal conductivity and specific heat to provide fast heat transfer, and low density and viscosity to reduce the fluid friction within the regenerator and heat exchangers. Hydrogen is the best choice given these criteria, however there are a few practical issues with using hydrogen as a working fluid. The main issue is containing the hydrogen, especially in a pressurised engine. The hydrogen will diffuse into and through the metal casing. This can cause the casing to become brittle and requires the hydrogen to be replenished periodically. It is also a flammable gas which can be a safety concern. Helium, being an inert gas, is a safer option and provides performance characteristics not far behind hydrogen, while causing less containment issues. It is however a relatively expensive gas and must be supplied in bottled form. Air or nitrogen are the most cost effective gasses and provide much less containment and supply issues; however they provide a much lower power density than either hydrogen or helium [17]. Pressurised air has been shown to pose an explosion risk owing to its oxygen content. An engine being developed by the Phillips Company in 1949 exploded, where the cause was determined to be lubricating oil vapour mixed with oxygen and ignited by the hot piston head [18]. Bottled nitrogen is very safe.

2.2.5 Flywheel

The flywheel is used to transform the intermittent torque from the engine into a continuous smooth rotational output. It achieves this by storing the mechanical work produced by the expansion stroke and using this to complete the remaining three strokes, none of which produce any useful power (the compression stroke actually requires work rather than produces work). The excess power not used to maintain the engine's rotation can then be extracted from the flywheel.

2.3 ENGINE TYPES

Over the years many engine configurations have been invented and tested with varying degrees of success. Those utilising the Stirling cycle can be split into three main categories depending on the configuration of cylinders and pistons. These categories are designated as alpha, beta and gamma.

2.3.1 ALPHA

The alpha type configuration consists of two power pistons connected to a flywheel with a phase difference of close to ninety degrees [20]. The simplest method to achieve this is to connect both pistons to the crankshaft and flywheel at the same point and have them operating with a separation of ninety degrees. This converts the linear motion of the pistons to a rotational output. One of the pistons is called the compression piston. It is located inside the compression cylinder, or cold side, as represented by the right hand cylinder in Figure 2.3 [21]. The second piston is called the expansion piston and is located in the expansion cylinder, or hot side, as represented by the left hand cylinder in Figure 2.3. The two cylinders are connected with a tube to allow the working gas to flow from one to the other during operation. In the centre of this tube is the regenerator. Figure 2.3 represents one complete cycle of an alpha type Stirling engine.

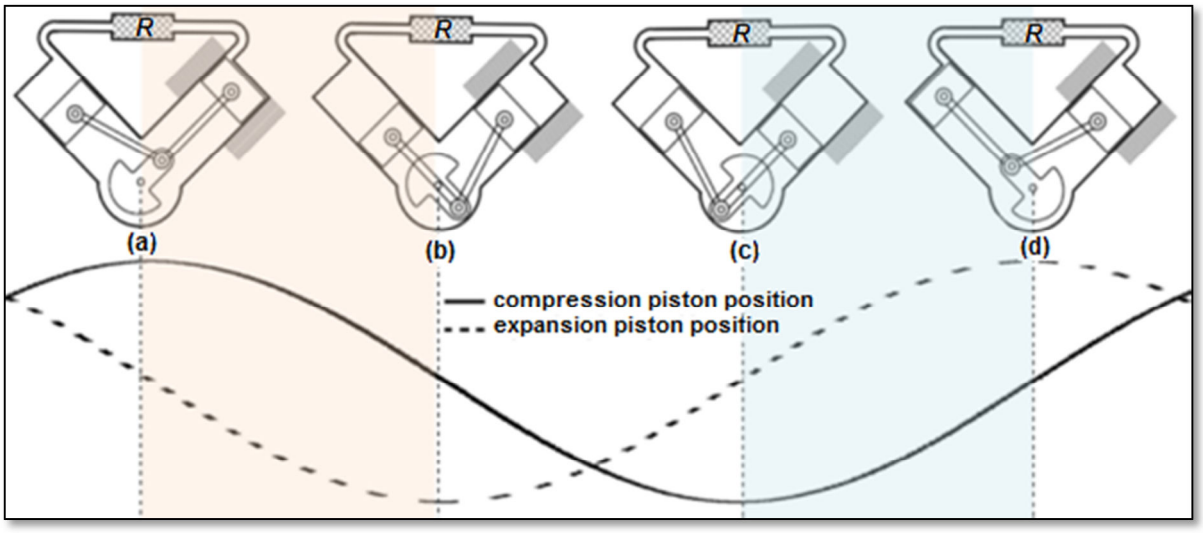

Figure 2.3: Complete cycle of an alpha type Stirling engine including compression and expansion piston displacement graphs (where R is the regenerator) [21]

In Figure 2.3(a) the compression piston is at the top dead centre (TDC) of its travel and the expansion piston is approximately at the half way point moving downwards towards the bottom dead centre (BDC) of its travel. At this stage the working fluid volume is at its minimum value and most of the working fluid is in the expansion cylinder. The flywheel is rotating clockwise and when it has travelled ninety degrees the position in Figure 2.3(b) is reached. This is called the power stroke as all the other strokes utilise the power of this stroke, with whatever is left being the net output power. It corresponds to the transition 1→2 in Figure 2.1, isothermal expansion. However, the engine operation forces the thermodynamic cycle to be far from ideal. One considerably non-ideal operation during this stroke is that the working fluid also begins to expand through the regenerator to the compression cylinder owing to the movement of the compression piston. This increases the temperature of the regenerator and decreases the temperature of the fluid.

In Figure 2.3(b) the expansion piston has reached the BDC of its travel and the compression cylinder is at about the halfway point moving towards the BDC of its travel. At this point the working fluid volume has reached its maximum volume. As the engine moves from Figure 2.3(b) to Figure 2.3(c) the working fluid volume remains fairly constant as the expansion piston moves upwards, reducing the internal volume of the power cylinder, and the compression cylinder moves downwards, increasing the internal volume of the compression cylinder. This corresponds to isochoric removal, transition 2→3

in Figure 2.1. The fluid continues to flow from left to right through the regenerator reducing the fluid's temperature and increasing the regenerator's temperature.

In Figure 2.3(c) the expansion cylinder is at the halfway point moving towards its TDC and the compression piston is at its BDC. The fluid volume is still at its maximum value but most of the fluid is now in the compression cylinder. Transitioning from Figure 2.3(c) to Figure 2.3(d) the compression stroke is completed. This corresponds to the isothermal compression transition 3→4 in Figure 2.1. A significant non-ideal operation during this stroke is that the working fluid also begins to compress from the expansion cylinder through the regenerator, increasing the working fluid temperature and decreasing the regenerator temperature.

In Figure 2.3(d) the expansion piston is at its TDC and the compression piston is at the halfway point traveling towards its TDC. The working fluid volume is at its minimum value and remains so in the transition from Figure 2.3(d) to Figure 2.3(a) as the compression cylinder volume decreases and the expansion cylinder volume increases. This process relates to the transition 4→1 in Figure 2.1, isochoric addition. As the working fluid flows from compression to expansion cylinder, heat is absorbed from the regenerator.

For a given volume, alpha type engines produce the highest specific power of the three basic engine types because they achieve a greater compression ratio [17]. Specific power is defined as the engine's power output divided by its weight. The compression ratio is defined as the maximum working fluid volume divided by the minimum working fluid volume. The main issue with the alpha design is the sealing of the hot side piston. Problems are caused by expansion of materials, especially when high temperature sources are used. The connecting tube used to transfer the working fluid between cylinders also creates unwanted dead volume. Dead volume is defined as any working fluid volume not swept by the pistons; this includes the working fluid volume contained within the heater, cooler, regenerator and all clearance and connection spaces. Any dead volume contained within the engine decreases its power output.

2.3.1.1 Multi cylinder designs

Alpha type engines also lend themselves to double acting, multi cylinder configurations. In general four cylinder designs are used, as illustrated in Figure 2.4 [17]. This setup is essentially four alpha type Stirling engines in series, with the top of each cylinder being the expansion end of the engines and the bottom of the following cylinder being the compression end. The cylinders are connected by tubes which allow the working fluid to flow from one to the next. The loops exiting the top of the cylinders in Figure 2.4 are the hot end heat exchangers. Half way along the connecting tube is the regenerator and below this is the cold side heat exchanger, after which the working fluid enters the compression end of the next cylinder. The cylinders are generally arranged in a circular formation, so that the far right cylinder in Figure 2.4 loops back round to the bottom of the far left cylinder. Compared to other Stirling engine configurations, this design can create a high specific power because the design is so compact.

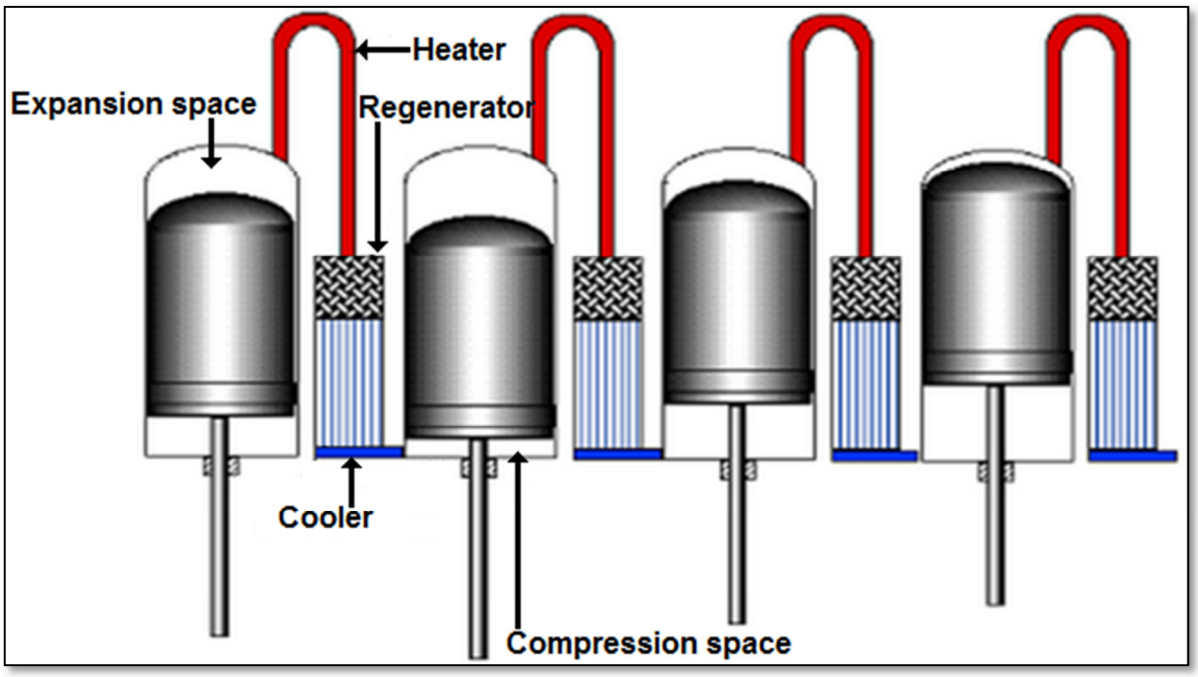

Figure 2.4: Multi cylinder double acting alpha type Stirling engine [17]

In Figure 2.4 each piston leads the preceding piston by ninety degrees. With four piston rods ninety degrees out of phase and arranged in a square, the mechanism for transferring this to a single output is always a complex system. Several ingenious designs have been developed including the swash plate, rocking yoke, wobble yoke, and

mechanical gears [17]. All of these mechanisms have the problem of producing excessive side thrust, thus increasing wear and reducing reliability [17].

2.3.3 BETA

The beta configuration utilises a displacer piston to move the working fluid around the engine [20]. A single power piston is located within the same cylinder to provide the power output. In the beta configuration one end of the cylinder is heated, in the case shown in Figure 2.5 [22] the bottom is the hot end, and the opposite end is cooled, as illustrated by the convection cooling fins in Figure 2.5. Because both piston and displacer are working in the same cylinder, the ninety degrees phase difference is achieved by connecting them at different points on the flywheel.

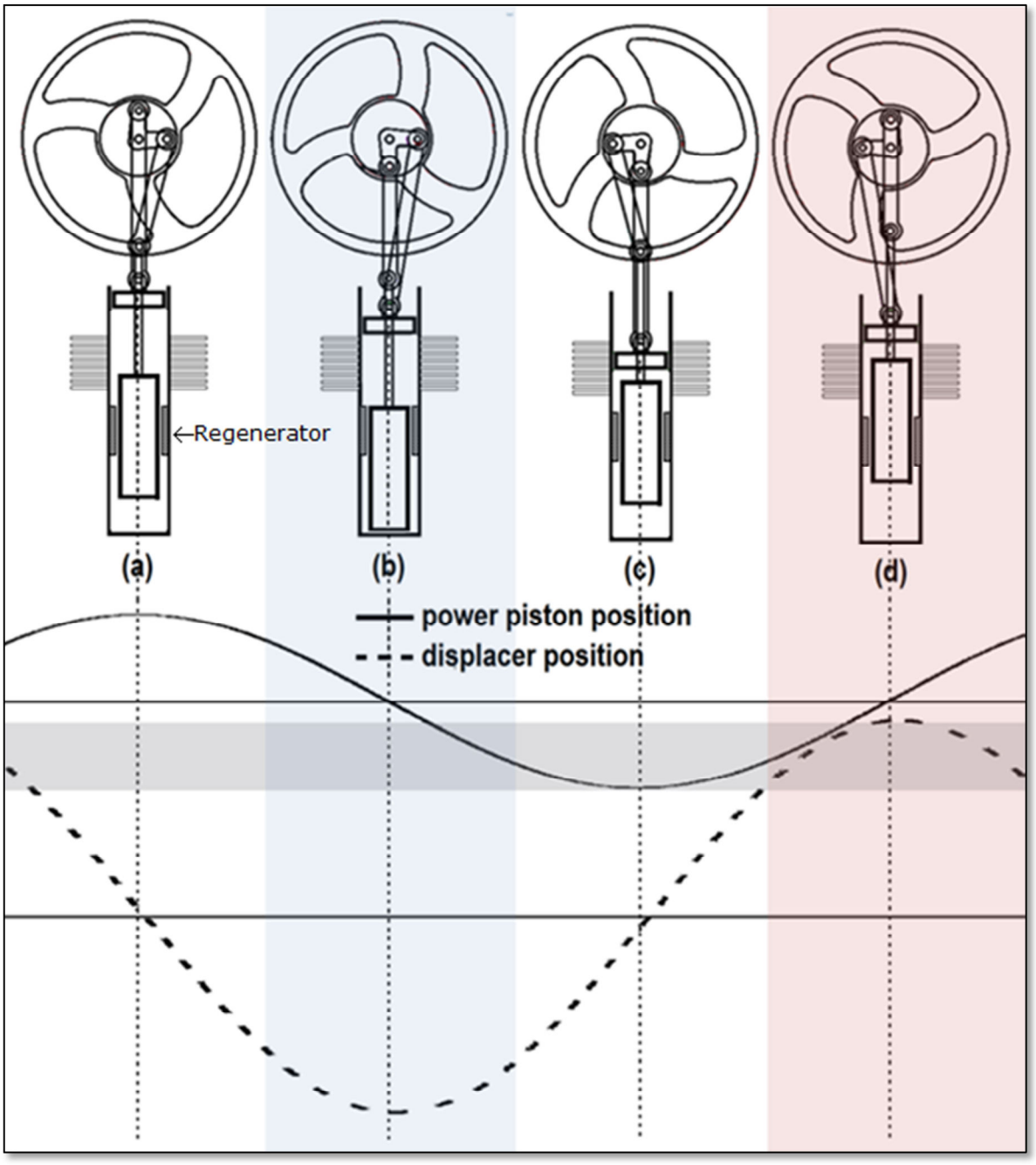

Figure 2.5: Full cycle of beta configuration Stirling engine including power piston and displacer position graphs [22]

Because only the power piston position effects the working fluid volume in the beta configuration, the extremes of its travel in Figure 2.5 do not represent the end of each stroke but rather the halfway point. In Figure 2.5(a) the power piston is at TDC and the displacer is at the centre position moving towards BDC. The working fluid volume is at its maximum value and the majority of it is in the compression end of the cylinder. This is the halfway point in the Transition 2→3 in Figure 2.1, isochoric removal. At the halfway

point of the transition from Figure 2.5(a) to Figure 2.5(b) the compression stroke begins.

In Figure 2.5(b) the power piston is at the halfway point on the way to its BDC, and the displacer is at its BDC. All of the working fluid is in the compression space and this is the halfway point of the compression stroke, transition 3→4 in Figure 2.1. In the transition from Figure 2.5(b) to Figure 2.5(c) the compression stoke finishes and the isochoric addition stroke starts, transition 4→1 in Figure 2.1. The displacer moves upwards shifting the working fluid to the hot end of the cylinder and the power piston does not have much vertical movement so this can be approximated as a constant volume heat addition.

In Figure 2.5(c) the power piston is at its BDC and the displacer is at the halfway point moving upwards towards its TDC. The engine is halfway through its isochoric addition phase, transition 4→1 in Figure 2.1. In the transition from Figure 2.5(c) to Figure 2.5(d) the isochoric addition finishes and the power stroke or isothermal expansion begins.

In Figure 2.5(d) the displacer has reached its TDC and the majority of the working fluid is now in the hot end of the cylinder. The engine is halfway through its expansion stroke and the power piston is at the halfway position on its way to the TDC. In the transition from Figure 2.5(d) to Figure 2.5(a) the expansion stroke finishes and the isochoric removal begins.

The beta configuration can produce a relatively high specific power for a displacement type engine because of the utilisation of the working volume. Figure 2.5 illustrates that there is an overlap in the displacement of the power piston and displacer at different stages of a single cycle. One cause of non-ideal operation is the sinusoidal motion of the displacer. As shown in Figure 2.5, in the initial phase of the compression stroke there is still some working fluid in contact with the hot side heat exchanger as the displacer moves towards its BDC. Conversely at the conclusion of the compression stroke the displacer is already moving towards its TDC allowing working fluid back into the hot side. The beta

configuration avoids hot side sealing issues by placing the power piston at the cold side. It does however have issues with heat conducting along the main cylinder, reducing its efficiency especially after long periods of operation. The regenerator placement requires a double-wall arrangement that can increase this conduction loss effect. Also the rod connecting the displacer to the flywheel must pass through the power piston, which creates a high friction area that reduces efficiency and requires a well-engineered seal. A system called the rhombic drive can be used to reduce engine vibrations and side thrust on the power piston by balancing the drive system [18].

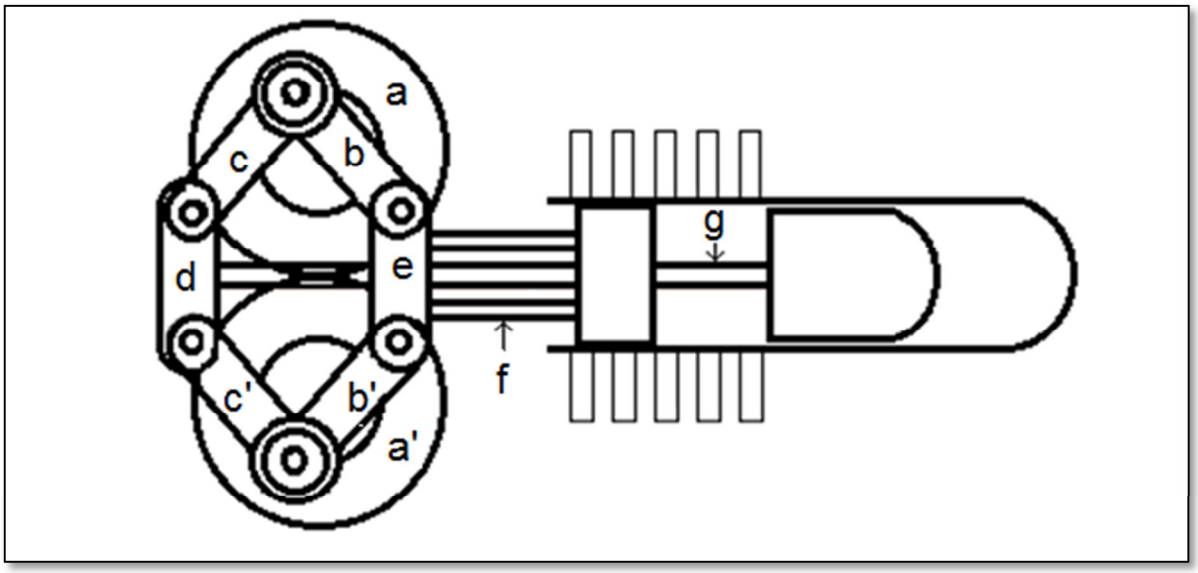

Figure 2.6: Rhombic drive (regenerator not shown) [7]

The rhombic drive was designed by R. J. Meijer in 1953 [18]. Its invention solved the problem of balancing smaller single cylinder engines. It creates axial movement of the piston rods and thus eliminates lateral forces on seals. Figure 2.6 shows the basics of the rhombic drive system. Two counter-rotating gear wheels, a, and, a', are positioned symmetrically either side of the central axis of the engine. The power piston is connected by piston rods, f, to a yoke, e, which in turn is connected to the two gear wheels via connecting rods, b, and, b´. The displacer is also connected to the gear wheels via connecting rods, c, and, c´, the yoke, d, and the displacer piston rod, g, which runs through the power piston. The rhombic drive was given its name because of the rhombus

shape formed between the two sets of connecting rods. The rhombic drive also allows for a non-pressurised crank case which saves weight especially in large engines. This is achieved by adding an extra pressure seal around the power piston rod to form a buffer space. When this buffer space is partially pressurised it compensates for the gas forces acting on the expansion side of the power piston. This is only achievable because the piston rod seals have no lateral thrust acting on them. The lateral forces transmitted from the connecting rods are exactly balanced at the yoke.

2.3.4 GAMMA

The gamma type engine also has a displacer and power piston, but they have separate cylinders [17]. This eliminates the need to have the displacer rod passing through the power piston, but also adds a certain amount of dead volume which decreases their specific power. Because the power piston is isolated from the heat source, problems with cylinder expansion and piston sealing are not present.

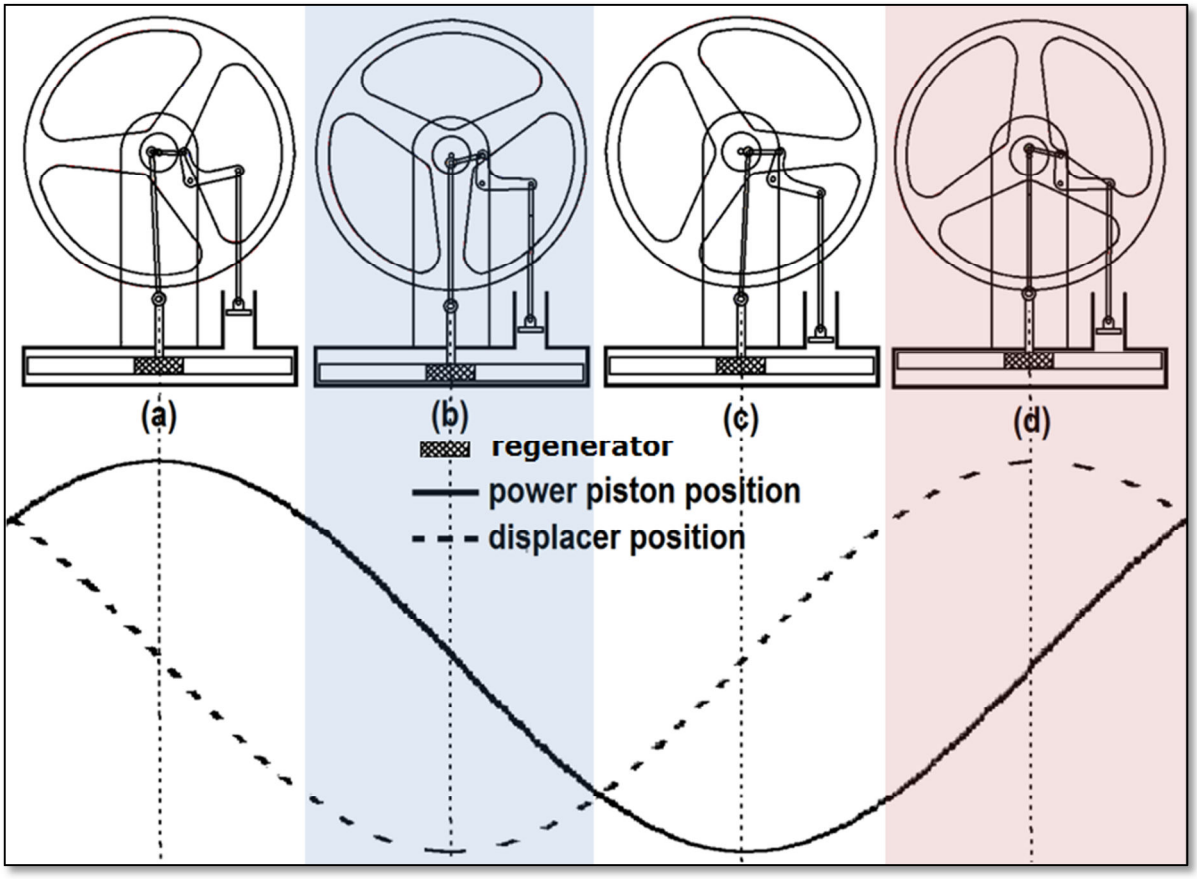

Figure 2.7: Full cycle of gamma configuration Stirling engine including power piston and displacer position graphs [23]

The operation of the gamma engine is very similar to the beta, with the main difference being the separation of power and displacer cylinders and the relative diameter of the piston and displacer. In Figure 2.7(a) the displacer is at its centre position moving towards its BDC and the power piston is at its TDC. The working fluid is transitioning from the hot side of the displacer cylinder to the cold side and the engine is halfway through the isochoric removal stage. At the halfway point between Figure 2.7(a) and Figure 2.7(b) the compression stroke begins. The sinusoidal motion of the displacer means there is still some working fluid in contact with the hot side, contributing to the non-ideal operation illustrated in Figure 2.8. Similarly at the end of the compression stroke some working fluid is in contact with the hot side as the displacer begins its travel towards its TDC.

At Figure 2.7(b) the displacer is at its BDC and the power piston is at its halfway point moving toward its BDC. All of the working fluid is now at the cold side, at this point the engine is halfway through the isothermal compression stroke. At the halfway point between Figure 2.7(b) and Figure 2.7(c) the isothermal compression stroke finishes and the isochoric addition stroke begins.

Figure 2.7(c) illustrates the midpoint of the isochoric addition stroke. The displacer is now moving back toward its TDC and the power piston has reached its BDC. The working fluid is transitioning from the cold side to the hot side. Halfway between Figure 2.7(c) and Figure 2.7(d) the isochoric addition stroke finishes and the expansion stroke begins. Again inefficiencies arise from the fact that some of the working fluid is still in contact with the cold side at the beginning and end of the expansion stroke. Also as the working fluid expands it must travel past the cold side, reducing its temperature and therefore expansion.

In Figure 2.7(d) the displacer has reached its TDC and the power piston is at its halfway point moving towards its TDC. The working fluid is now mostly at the hot side and the engine is halfway through the expansion stroke. Halfway between Figure 2.7(d) and Figure 2.7(a) the expansion stroke finishes and the isochoric removal stroke begins, thus returning to the beginning of the closed loop process.

The gamma type engine is generally used where separation of the power piston cylinder is advantageous. This separation means that there are no sealing issues associated with heating of the power piston cylinder, making it the simplest to design and manufacture. Because of the increased volume associated with the separation of the power and displacement cylinders, the gamma type engine produces the lowest compression ratio of the three designs. If a regenerator is utilised, it is generally placed around the circumference of the displacer chamber so that the working fluid must pass through it as the displacer moves. An alternative is to integrate the regenerator into the displacer, as seen in Figure 2.7.

2.4 Power Production

2.4.1 Idealised Power Output

The work produced by the ideal Stirling cycle can be calculated as the integral of the working fluid pressure with respect to volume, as seen in equation 1 [24].

$$W = \oint P dV \tag{1}$$

This can be visualised as the area enclosed by the four transitions in the PV diagram in Figure 2.1, and can be expressed as the integral of the transition 1→2 minus the integral of the transition 3→4, seen in equation 2.

$$W = \int_{V_1}^{V_2} P dV - \int_{V_3}^{V_4} P dV \tag{2}$$

By substituting the ideal gas law, shown in equation 3,

$$PV = nRT \tag{3}$$

and using the transformations in equation 4.

$$\int_{V_A}^{V_B} P dV = \int_{V_A}^{V_B} \frac{nRT}{V} dV = nRT \ln\left(\frac{V_B}{V_A}\right) \tag{4}$$

The work produced in a single closed loop cycle can be expressed by equation 5.

$$W = nRT_H \ln\left(\frac{V_2}{V_1}\right) - nRT_C \ln\left(\frac{V_4}{V_3}\right) \tag{5}$$

This can then be simplified to give the expression in equation 6.

$$W = nR \ln\left(\frac{V_2}{V_1}\right)(T_H - T_C) \tag{6}$$

Of course it is impossible for these transitions to take place instantaneously (in fact, most engines use a sinusoidal transition motion which is far from instantaneous), at any point in the cycle there will be variations in pressure and temperature throughout the working fluid and heat exchangers. This results in a real world cycle diagram more like that seen

in Figure 2.8 [25]. The power output can still be calculated by integrating the fluid pressure with respect to volume, which amounts to calculating the area enclosed within the PV diagram.

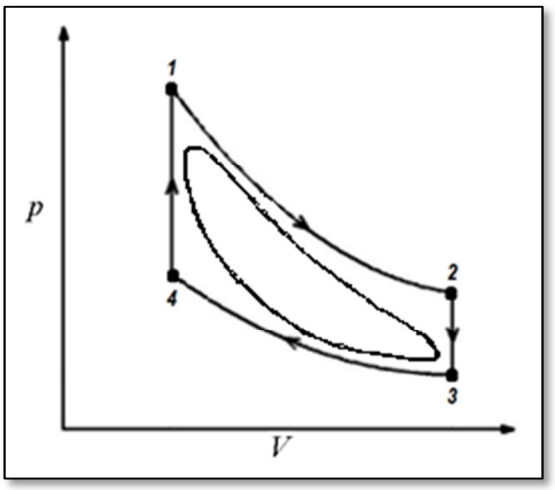

Figure 2.8: Real world PV diagram, where the internal smooth cycle curve shows the actual engine operation, and the outside curve shows an ideal operation cycle [25].

2.4.2 CARNOT LIMIT

There is a theoretical efficiency limit to the power that any heat engine can produce given a heat source to sink temperature difference of $T_H - T_C$; this is called the Carnot limit [26]. Equation 7 describes the Carnot efficiency [26], this is a measure of the ratio of output work that the engine produces, to heat absorbed from the heat source. The theoretical maximum Stirling cycle efficiency is equal to the Carnot efficiency.

$$\eta_{max} = \eta_{carnot} = 1 - \frac{T_C}{T_H} \quad (7)$$

2.4.3 REAL WORLD POWER ESTIMATION

There are many methods for estimating the power produced by a Stirling engine design depending on the level of accuracy that is desired. The simplest and most widely used is the Beale formula shown in equation 8 [27],

$$P_o = B_n P f V_e \quad (8)$$

where P_o is the power output in W, B_n is the Beale number, P is the average working fluid pressure in Pa, f is the operating frequency in Hz and V_e is the expansion space

volume in m^3. The Beale number can be calculated in several ways for a prototype design. For well-designed, high temperature differential engines, a constant between 0.11 and 0.15 is generally used [28]. It has been suggested by Kongtragool and Wongwises [29] that the best method for estimating power output, especially for LTD Stirling engines, is the mean pressure power formula shown in equation 9,

$$P_o = PfV_eF\left[\frac{T_H - T_C}{T_H + T_C}\right] \quad (9)$$

where T_H and T_C are the hot and cold space working fluid temperatures respectively in K. F is a dimensionless factor that can be altered for different types of engines. It has been shown that $F = 2$ for the ideal Stirling cycle, but a value between 0.25 and 0.35 should be used for practical calculations [29].

A more accurate and consequently more involved method is the Schmidt analysis, which was developed by Gustav Schmidt in 1861 [19, p. 25]. The analysis calculates the closed form solutions for the case of *sinusoidal* working volume variations with respect to the cycle angle. The Schmidt formula to calculate work per cycle for gamma configuration Stirling engines is shown in equation 10 [29].

$$W_{Schmidt} = PV_P\pi \sin\frac{(1-\tau)}{A + (A^2 - B^2)^{\frac{1}{2}}} \quad (10)$$

$$A = (1+\tau) + \frac{(4k_s\tau)}{(1+\tau)} + k_p \quad (11)$$

$$B = \left[(1-\tau)^2 - 2(1-\tau)k_p cos\alpha + {k_p}^2\right]^{\frac{1}{2}} \quad (12)$$

$$p_m = p_{max}\left[\frac{(A-B)}{(A+B)}\right]^{\frac{1}{2}} \quad (13)$$

$W_{Schmidt}$ is the work produced per cycle in Nm, P is mean cycle pressure in Pa, p_{max} is maximum pressure attained during each cycle in Pa, $k_p = V_p/V_d$ is swept volume ratio, $k_s = V_s/V_d$ is dead space volume ratio, V_s is dead space volume in m^3, α is phase

angle lead of the displacer over the power piston in degrees and τ is the working fluid temperature ratio T_C/T_H. Inefficiencies are then taken into account; power losses such as heat transfer, heat conduction loss, mechanical friction and fluid flow friction are calculated and subtracted from the initial power estimation. Note that the analysis is only valid for sinusoidal piston velocity profiles (for both the power and displacer piston).

More recently computer simulations have been the favoured method for engine design and power estimation as more variables can be added to achieve greater accuracy. The engine is modelled by writing conservation of mass, volume and momentum equations for several control volumes of the gas circuit in the form of partial differential equations. Realistic initial conditions are input and the conservation calculations are performed continuously until reaching a steady state condition, at which point the engine performance characteristics can be obtained [30].

2.5 LTD STIRLING ENGINES

The LTD Stirling engine is generally characterised as any Stirling engine which runs on a temperature difference of less than around two hundred degrees Celsius [31] [32] [14] [13]. They are usually large for the power they produce, meaning they have a low specific power. They also have a low compression ratio because of the large volume of working fluid needed to produce a reasonable power output. Because piston and displacer inertia generally increases with size, lower operating speeds are required to limit mechanical stresses. As described by the Carnot limit, the efficiency of a Stirling engine is proportional to the temperature difference; this means that LTD Stirling engines inherently have a low efficiency. Despite these limitations LTD Stirling engines are still capable of producing a useful power output. Equation 9 illustrates that the power output of a Stirling engine in the simplest terms is proportional to the working fluid pressure, operational frequency, expansion volume and applied temperature differential. To extract a useful amount of work out of a LTD source, the other parameters must be adjusted to increase the power output. This is generally achieved in one of three ways.

The first method of increasing power is to increase the working fluid volume, by simply increasing the size of the engine. With more working fluid a greater number of molecules

of working fluid are present, which increases the expansion volume for a given temperature rise and therefore increases the power output. By increasing the working fluid volume the physical size of the engine must also increase, and in doing so the inertia of moving components is also generally increased. This increase in inertia means that it requires more force to accelerate and decelerate components within the engine, increasing mechanical stresses. To reduce mechanical stresses engine speed is generally reduced, which limits the operating frequency of the engine and has a detrimental effect on the power output. More efficient heat exchangers are also required to compensate for the increased working fluid volume, which increases the cost of the engine.

The second, most widely utilised method for increasing power is to increase the pressure of the working fluid. Again more molecules of working fluid are introduced, increasing thermal conduction and expansion volume for a given temperature rise, and therefore increasing power output. This technique increases the complexity of the case design and shaft seals. The effectiveness of the heat exchangers is increased owing to the increased thermal conductivity of the working gas. The fluid friction losses, however, increase due to the increased viscosity of the working fluid.

The third method of increasing power is to use a Multi cylinder design. By using multiple cylinders essentially you can scale the power output of a single smaller engine by the number of cylinders introduced. This method increases the design complexity, especially with regard to the crankshaft design.

It is possible for all the general forms of Stirling engine (alpha, beta and gamma) to be configured to operate under LTD conditions. Over the years many forms of Stirling engine have been tried. During a period of twelve years Professor Ivo Kolin designed, built and tested 16 engines with the aim of reducing the temperature difference on which a Stirling engine could run [33]. These 16 engines included such innovations as diaphragm pistons, discontinuous displacer motion, rotary displacers, and flat plate heat exchangers. Since the efforts of Professor Ivo Kolin and Professor James Senft in the 1970s and 1980s, one type of LTD design has dominated. It is known as the flat plate gamma configuration, an example of which is shown in Figure 2.9 [34]. The flat plate gamma configuration

combines low compression ratio, large heat transfer areas, minimal dead space and simple construction to achieve unsurpassed LTD operation.

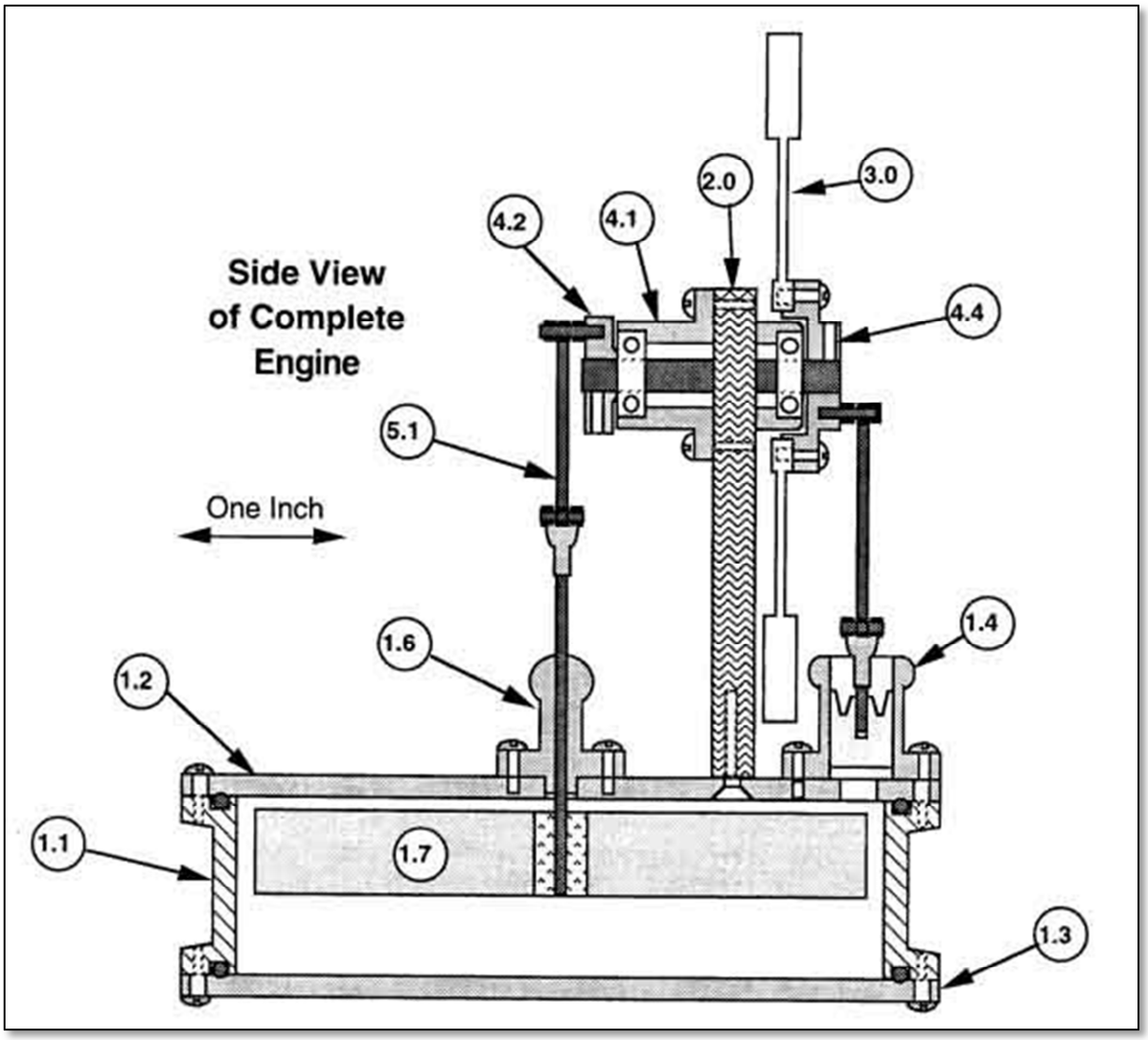

Figure 2.9: Modern LTD Stirling Engine [34]

This design consists of a large diameter, relatively flat displacer cylinder with thermally conductive top and bottom (Figure 2.9, 1.2 & 1.3) to act as flat plate heat exchangers. The flat design increases the heat exchanger area through which heat can be delivered and expelled. The edge of the displacer cylinder (Figure 2.9, 1.1) is made of a thermally insulating material to prevent thermal shorting between hot and cold heat exchangers. The displacer (Figure 2.9, 1.7) fits loosely inside the displacer cylinder and is made of a light weight thermally insulative material. If a regenerator is included, it is generally placed within the displacer or around the circumference of the displacer. The power piston cylinder

(Figure 2.9, ⑭) is of much smaller diameter than the displacer cylinder and is situated directly on top of the top plate heat exchanger to minimise dead space. The power piston creates an air tight seal within the power piston cylinder whilst creating as little mechanical friction as possible. Both displacer and power piston are connected to a flywheel (Figure 2.9, ⑩) which keeps the engine running during the compression phase and maintains the desired phase angle of around 90°. While this design achieves excellent LTD operation, it does not scale very well for power production for several reasons. When increasing the size geometrically the internal volume will increase at a greater rate than the heat exchanger surface area. This will result in less efficient heat conduction and therefore power output. If the engine was to be pressurised to increase efficiency the large flat shape is not conducive to containing high pressures.

2.5.1 Existing Large Scale LTD Stirling Engines

The idea of using Stirling engines to produce useful energy from LTD sources is being researched and developed around the world. The National Institute for Research and Environment in Japan have constructed and tested a 300 W gamma type Stirling engine [35]. The power piston has a 100 to 200 mm variable stroke length and a 400 mm diameter. The displacer has a diameter of 800 mm and a stroke of 80 mm creating a compression ratio of 1.271. Copper fin and tube heat exchangers were used along with a copper mesh regenerator. The design is capable of being pressurised; however, operating under atmospheric pressure conditions experimental results show a maximum output of 210 W at 100 rpm. The heat source fluid was ethylene glycol at a temperature of 130 °C with a flow volume of 20 l/m. The heat sink fluid was water at a temperature of 15 °C with a flow Volume of 20 l/m [32].

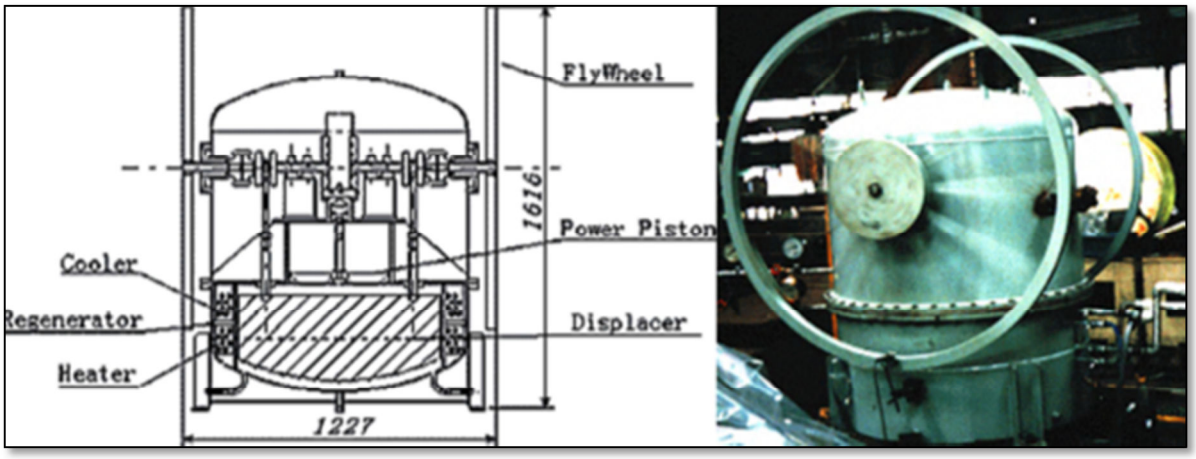

Figure 2.10: 300W gamma type Stirling engine [35] [32]

In Tamera, Portugal, a 1.5 kW beta type LTD Stirling engine has been constructed by Sunvention International, as seen in Figure 2.11 [36]. The working fluid is air and the engine is run with an internal pressure close to atmospheric. The main cylinder has a diameter of 2 m and a height of 0.5 m. The hot side temperature is 150 °C, delivered by solar collectors. The thermal delivery medium is either water at a pressure of 5 bar, or unpressurised vegetable oil. The cooling fluid is unpressurised water. The engine has been tested for over 1000 hours of operation and has an estimated working lifetime of 30 years. One innovative feature is the active phase control, which can adjust the power output by manipulating the phase delay between the power piston and displacer. The rolling fabric seal on the power piston provides a simple and easily replaced seal [36].

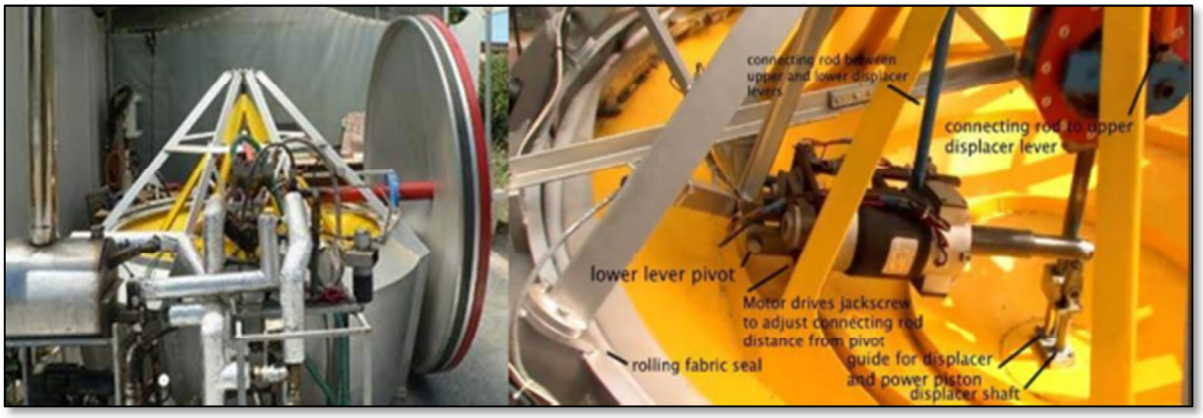

Figure 2.11: Sun Pulse Electric [36] [37]

Suction Gas Engine Mfg. Co. Ltd has produced a 1 kW alpha type LTD Stirling engine as seen in Figure 2.12 [38]. The heater and the cooler utilise compact plate fin and tube

type heat exchangers and conventional laminated brass wire net is used for the regenerator. The drive system is a unique mechanism that they call the "X yoke Mechanism". By adopting this mechanism, the engine is more compact and can accomplish reduced mechanical friction losses and side thrust on the piston rings. The engine's body is similar to a conventional pressure vessel, meaning it can be run at very high pressures. It has currently produced a maximum output of $740\,W$

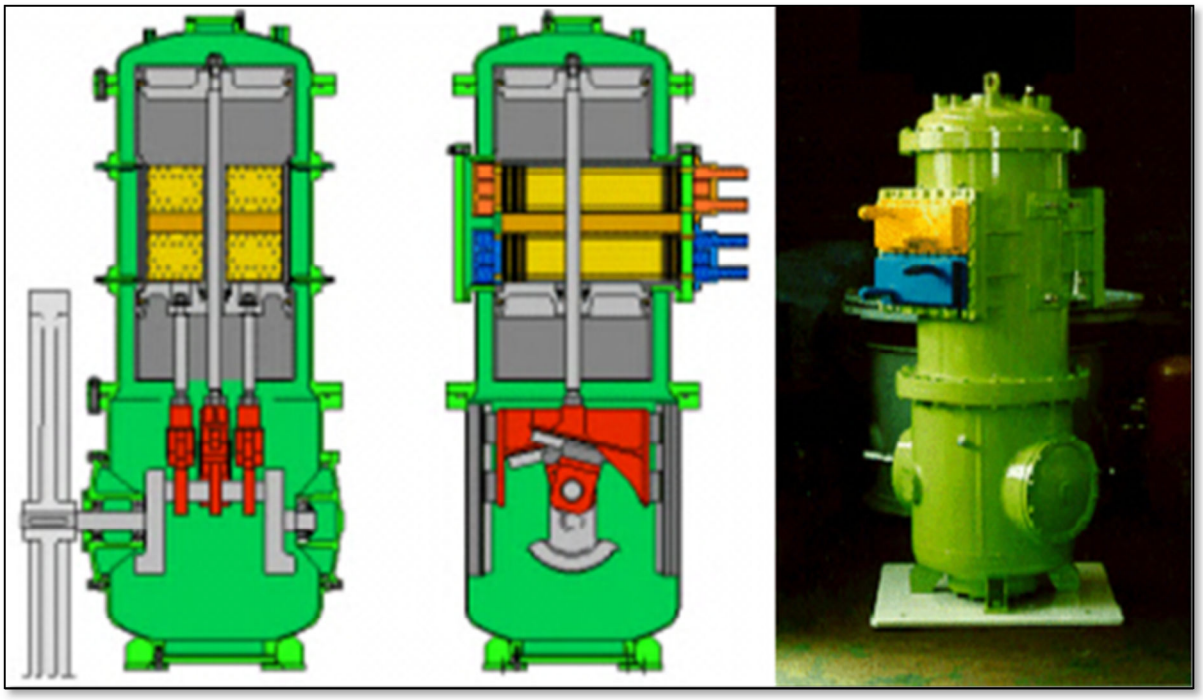

Figure 2.12: Suction Gas Engine Co ltd Alpha Type LTD Engine [38]

Probably the most promising design is the "ThermoHeart Engine" developed by Cool Energy Inc. in Boulder, Colorado, USA [39]. They have developed a $3\,kW$, three cylinder, single acting alpha Stirling engine as seen in Figure 2.13. Nitrogen is used as the working gas. It is optimised for temperatures of $100-300\,°C$, using a mineral-oil based fluid for heat transfer with a flow range of $40-150\,l/m$. The engine has been shown to achieve a thermal to electric conversion efficiency of $25\,\%$ at 600 rpm. They claim it is designed for a 70,000 hour maintenance free life and will be commercially available in late 2014 for around $12,000 USD. They are also developing a $20\,kW$ model with an operating speed of $600\,rpm$ that will weigh $5500\,lbs$, have a lifetime of 100,000 hours with service intervals of 20,000 hours and produce output voltages up to $500\,V_{dc}$ [38].

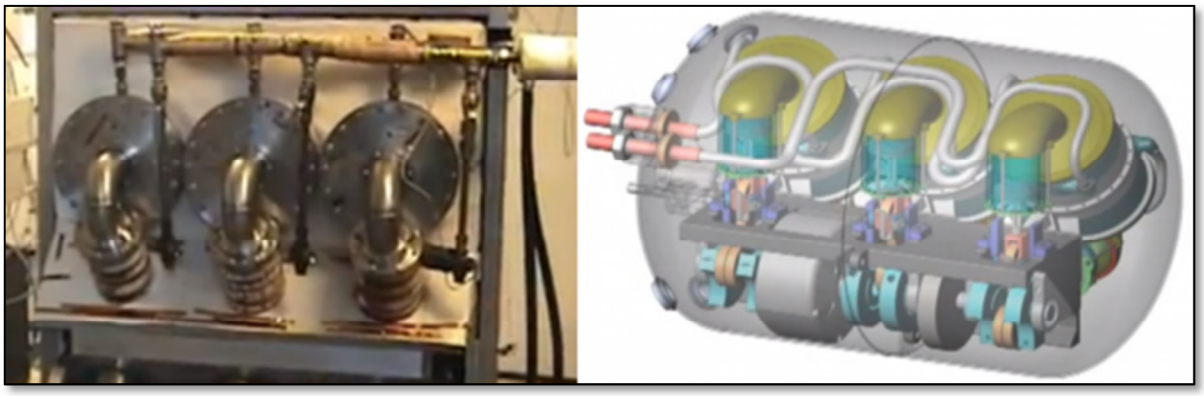

Figure 2.13: Solar Heart Engine 2nd and 3rd prototypes [40]

2.6 LLOYD'S ENGINE DESIGN

This section describes the LTD Stirling engine design that was developed by Caleb Lloyd as a Masters project in 2008 [14]. The major design objectives and decisions are outlined. A description of the main components is given, including the displacer, power piston, heat exchangers, regenerator, crank shaft and generator.

2.6.1 DESIGN OBJECTIVES

The main design goals for the engine were to keep the cost as low as possible while aiming to produce an electrical power output of up to $500\,W$. The thermal input objectives were a hot side temperature range of 50°C to 90°C, with a cold side temperature of 20°C. Initially the design principles of the traditional pancake design were aspired to; however it was concluded with preliminary calculations that a pressurised design would be required to achieve the designated power output. This meant that a large diameter, flat displacer chamber would have unmanageable forces on the end plates when pressurised, leading to the choice of a smaller diameter, longer chamber. Because of this design choice it was infeasible to provide sufficient heat exchange with external heat exchangers as is traditional with LTD Stirling engines. Internal heat exchangers were designed to provide sufficient heating and cooling for the chosen volume of working fluid. The design process culminated in a $10\,bar$ ($1000\,kPa$) pressurised, gamma type LTD Stirling engine with a rotary reciprocating-motion displacer, using hot water as a heat source and air as the working fluid. The displacer chamber was split into three sections of equal volume, one containing the heat exchanger elements, one the displacer, and the remaining third the

working fluid, as seen in Figure 2.14. The third containing the heat exchanger was also split into thirds, with the hot and cold heat exchangers either side of the regenerator. A detailed description of the engine design process can be found in [14].

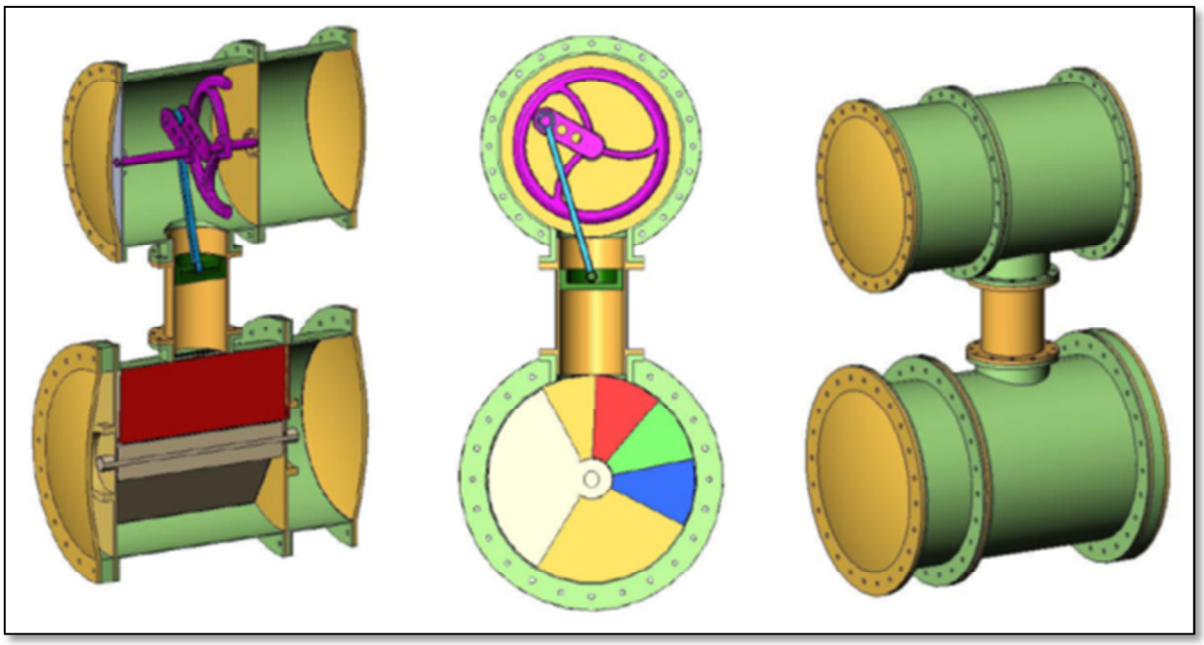

Figure 2.14: Lloyd's CAD model [14]

To keep costs down, industrial steam piping was utilised for the displacer and power piston cylinders. This also provided a good structure to create a pressurised chamber. A pressure of $1000\,kPa$ was concluded to be achievable with such materials. With the desired power output of $500\,W$, the Beale formula was used to calculate a required expansion volume of $0.005m^3$. Using a general relationship between volume ratio and temperature ratio, the required compression space volume was calculated to be $0.083m^3$ [14]. It was decided to increase this value to $0.130m^3$ to allow lower temperature differentials to still produce a reasonable output power. Using the Carnot formula, the maximum theoretical efficiency of the prototype engine was calculated to be 19%. Taking into acount heat losses, stray thermal conduction paths, an imperfect regenerator, dead space, internal friction of bearings and seals and mechanical to electrical transformation losses, this value was reduced to an estimated total efficiency of around 5%. Figure 2.15 shows the constructed pressure vessels.

Figure 2.15: Constructed pressure vessels, displacer chamber (left) and generator chamber (right) [14]

The engine will operate as illustrated by Figure 2.16. In Figure 2.16 (a) the displacer is rotating anti-clockwise, shifting the working fluid from the hot side to the cold side. This is the isochoric removal stroke, where the heat is removed from the working fluid while its volume remains relatively constant. Figure 2.16 (b) represents the central point of the compression stroke. The working fluid is now in contact with the cold side heat exchanger and remains at a fairly constant temperature as the power piston uses stored mechanical energy from the flywheel to compress it. Figure 2.16 (c) depicts the engine at the central point of the isochoric addition stroke. This is where the volume is largely unaltered much while the displacer shifts the working fluid from the cold to hot side. To finish the cycle, Figure 2.16 (d) shows the central position of the power producing expansion stroke. Here the working fluid increases in temperature because it is in contact with the hot side heat exchanger. This causes the working fluid to expand, forcing the power piston upwards.

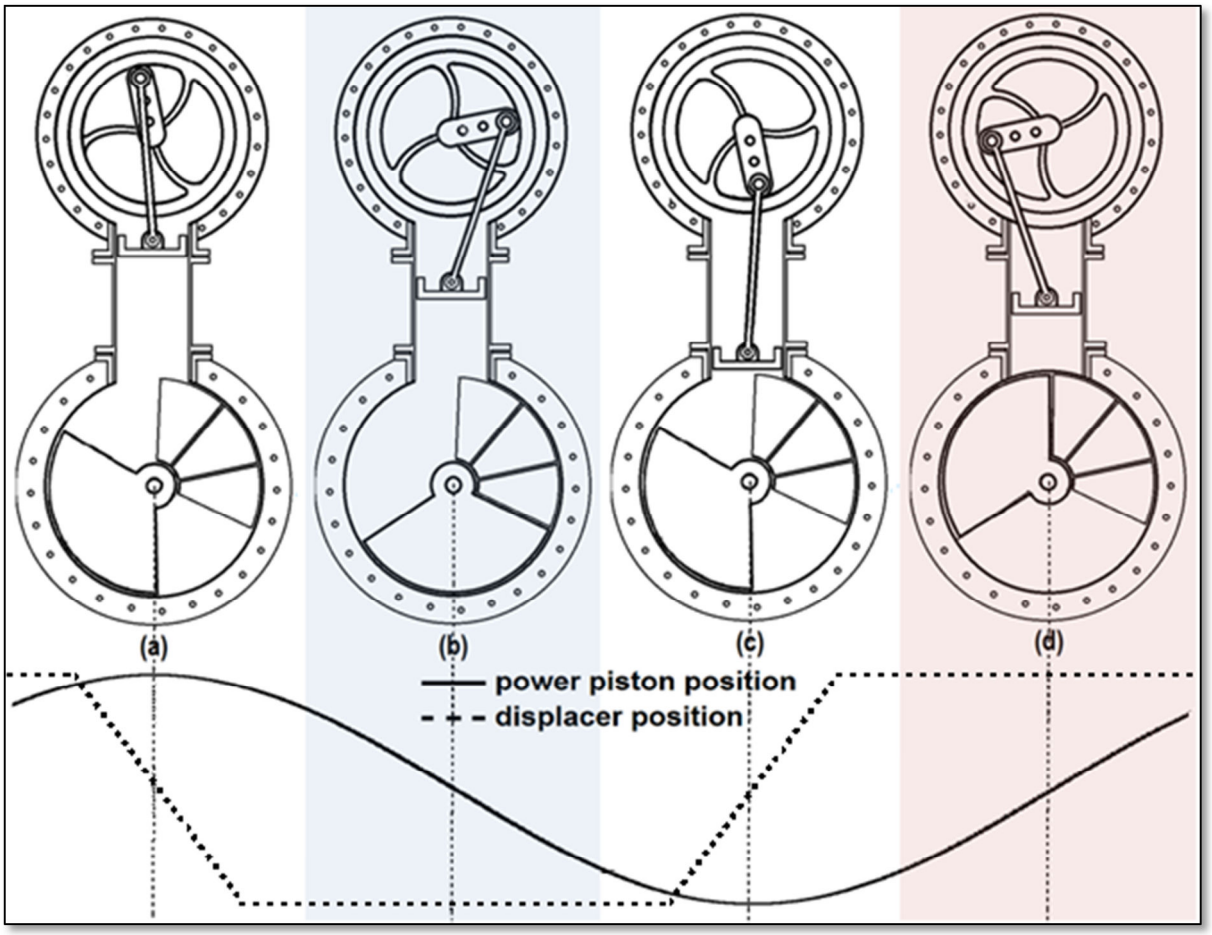

Figure 2.16: Operating cycle of Lloyd's engine design

2.6.2 DISPLACER

The displacer arrangement for this project is fairly novel and untested. Instead of being cylindrically shaped and occupying the whole cross sectional area of the displacer cylinder, it is formed in a wedge shape occupying one third of the displacer cylinder and rotates back and forth about a central shaft. This motion forces the working fluid to pass through the heat exchangers and regenerator, which occupy a further 120° wedge of the displacer chamber.

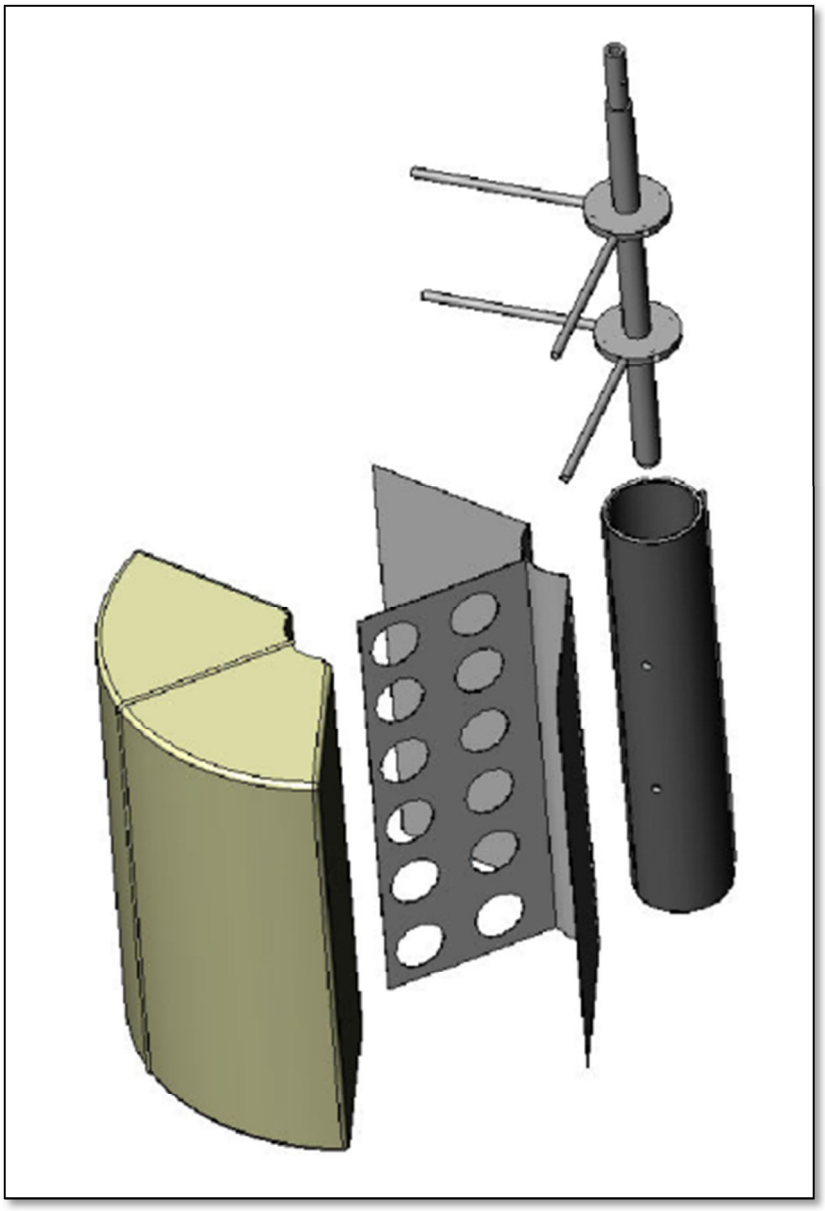

Figure 2.17: Original displacer design [14]

Figure 2.17 shows an exploded view of the displacer design developed in [14]. The central shaft was constructed of aluminium and connected to a PVC pipe with disk shaped aluminium supports. The exterior shell was constructed of aluminium sheet and filled with HP35 expanded polyurethane foam. In order to prevent any unwanted working fluid leaking around the displacer, seals were designed to seal against the inside of the displacer chamber, which will be lined with a piece of polypropylene plastic. These seals run around the central axis of the displacer, but divert around the circumference of the top and bottom of the PVC cylinder to prevent the working fluid passing through the bearings supporting the central shaft. These seals were made of fabric folded in half and pinched

between two aluminium strips. They are designed to protrude $4\,mm$ from the outer edge of the displacer.

In [14] it was decided that the actuation of the displacer would be achieved independently of the crank shaft for two main reasons. The first reason was that independent displacer actuation eliminated the need for a shaft to exit the pressurised generator chamber and enter the displacer chamber, which would have required two expensive shaft seals. The second was that it has been shown that a non-sinusoidal displacer motion can increase the mechanical power output in low speed engines [41]. While this could feasibly be achieved with a mechanical linkage, it would be a lot easier in a prototype to construct and control with electric motors. It was decided to use a stepper motor system in a pressurised, but isolated, section of the displacer chamber to actuate the displacer. In this way various displacer velocity profiles could be achieved with very little effort by simply altering the stepper motor control code. The engine design called for the displacer to be rotated 120° back and forth. The desired displacement patterns included varying this motion from the commonly used sinusoidal displacement to as close to a square wave as possible.

The actuation design in [14] was initially to have a single stepper motor connected to the displacer through an Anaheim Automation 10:1 gear box. The stepper motor chosen in [14] was Lam Technologies Nema 34, M1343061, which at the time was the most powerful in its range. It was a two phase, $1.8°$ step angle, hybrid design stepper motor, with a holding torque of $12.1\,Nm$ and a maximum phase current of 12A. After initial testing in [14] it was found that a single stepper motor would not be powerful or fast enough to actuate the displacer at the engine design frequency and an alternative method was proposed. The proposition was that an extra motor should be added to double the power output and the 10:1 gearbox replaced with a 2:1 gearing system to increase displacer peak velocity. This proposed setup is illustrated in Figure 2.18.

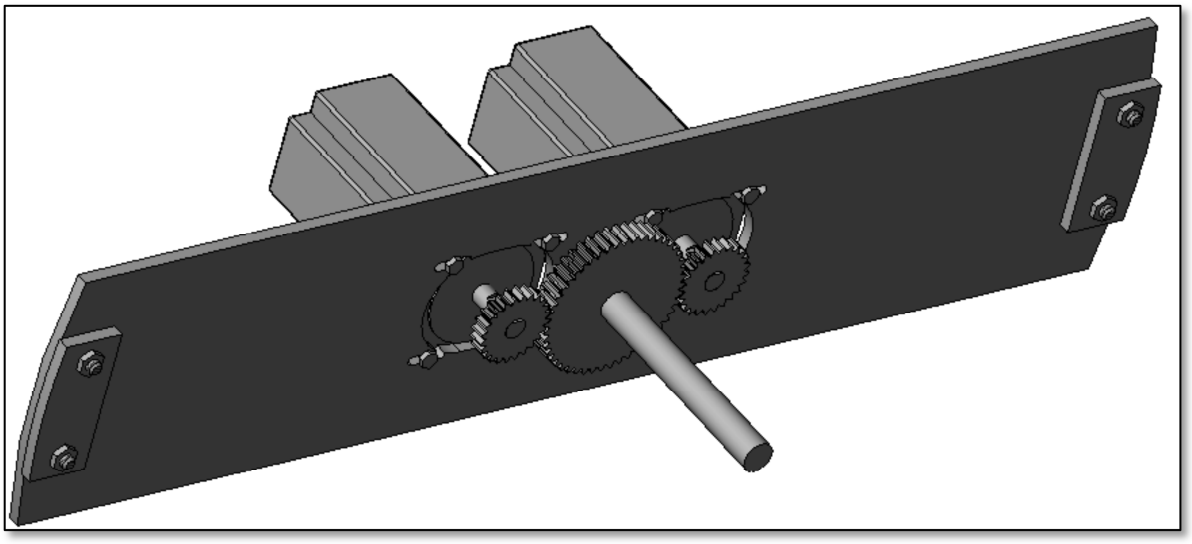

Figure 2.18: Dual stepper motor drive proposed in [14]

Stepper motors require a controller to provide the correct sequencing of their stator coils. The IBC-400E intelligent motion controller from Advanced Micro Systems was chosen in [14] to achieve this function. The IBC-400 can provide step and direction outputs at speeds up to 60,000 steps/second, and also has provision for limit and home inputs as well as encoder feedback. The IBC-400 can be programmed via serial interface utilising either RS-422 or RS 232 protocols. To provide the necessary current for the motors, the controller was connected to a pair of Lam Technologies DS1078 stepper motor drivers. These drivers take the signals from the controller and amplify them, providing the power output required to run the motors. The DS1078 stepper motor drivers require a DC input voltage of 90V and can produce a peak output phase current of 14.1A.

2.6.3 CRANK SHAFT

The power piston connector rod, crank shaft, and flywheel arrangement converts the power piston's linear motion into the rotational motion used to power the attached synchronous electric generator. The main design goals were to produce a rigid, balanced and adjustable crankshaft. The rigidity would prevent any power loss through flexing. It must be balanced to prevent vibration which could potentially lead to component failure. Adjustable power piston stroke length is desired to test the effects of altering the expansion volume of the engine.

Figure 2.19: Power piston, connector rod, and crank shaft design [14]

Figure 2.19 shows a SolidWorks™ model of the final design. The shaft is attached to the crank by two flat plates with four triangular braces. These are all made of aluminium to provide a lightweight rigid structure. The flat plates have slots milled in them to allow adjustment of both the connecting rod (con-rod) and counter balancing weights. By altering the position of the con-rod attachment to the crank shaft, the length of the power piston stroke can be adjusted. The adjustability of the counter balancing weights means that the system can be easily balanced for different stroke length configurations. The con-rod is also adjustable in length to allow the position of the power piston to be adjusted. Each end of the con-rod has a ball joint bearing; these are connected to the central section via a threaded rod as shown in Figure 2.20. One will have a left hand thread and the other a right hand thread. Consequently when the central section is rotated one direction its overall length will be increased, and when rotated the other direction its length will be reduced.

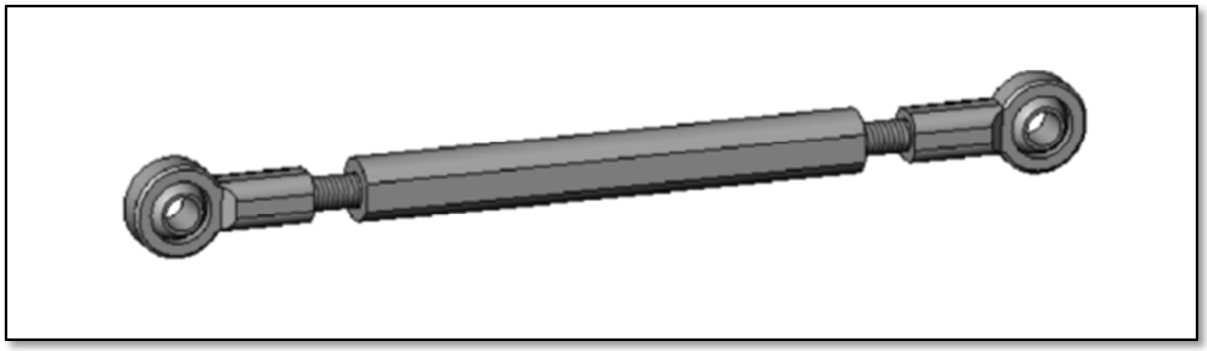

Figure 2.20: Con-rod design [14]

2.6.4 Power Piston

The power piston captures the energy of the expanding working fluid and transfers it to the crank shaft to be utilised as a rotational mechanical output. The design objectives for the power piston were to make it as light weight as possible and to reduce the losses associated with its constant acceleration and deceleration. The seals should prevent any working fluid from getting past the piston, whilst creating as little mechanical friction as possible. As with all other components the final design must provide a relatively low cost solution.

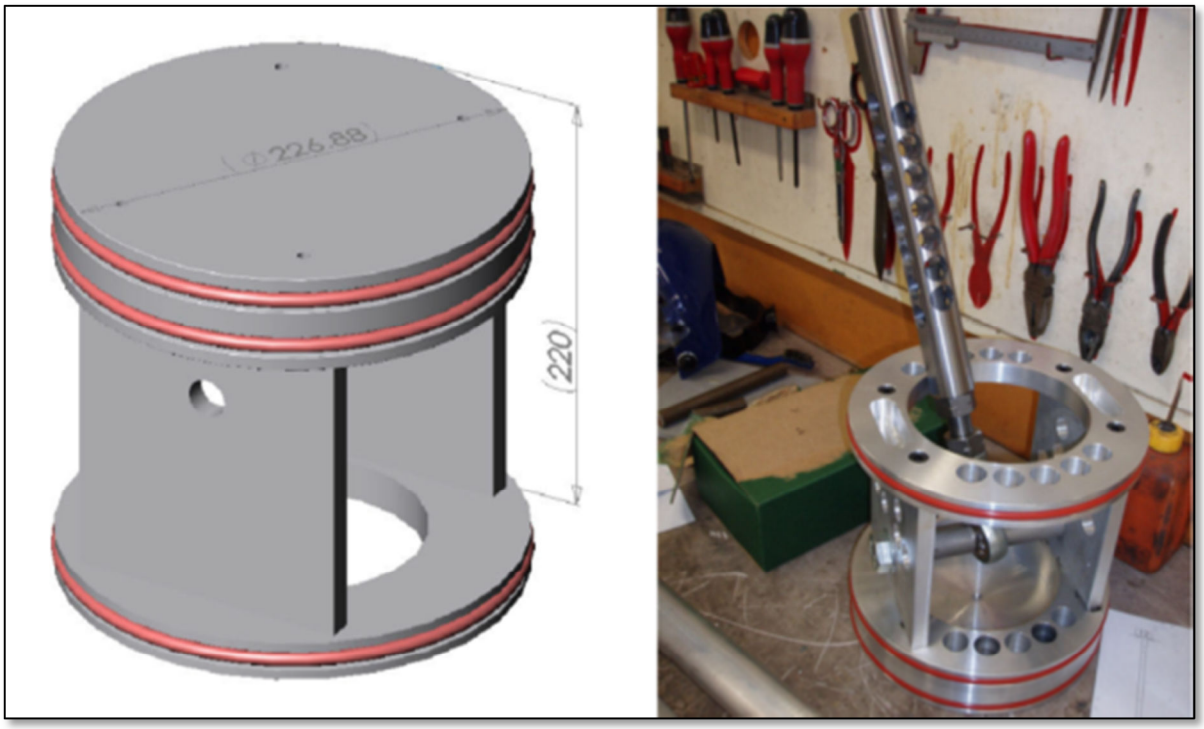

Figure 2.21: Power piston SolidWorks model (left), Constructed power piston with con-rod (right) [14]

Figure 2.21 illustrates the design solution. The piston structure is machined from aluminium to provide a rigid lightweight structure. Because of the low temperatures used in the engine, expansion or deformation should not be an issue. Two silicone rubber O-rings are placed at the end facing the working fluid to provide a good seal. A third O-ring is placed at the far end to stabilise the piston within the chamber. Silicone grease will be used to provide lubrication and facilitate a low friction movement. To save costs, instead of machining from a solid aluminium block, the top and bottom discs are machined from solid aluminium and are connected together with 10 mm aluminium plate.

2.6.5 GENERATOR

The generator converts the mechanical power of the Stirling engine into an electrical output. By measuring the electrical output power and knowing the mechanical to electrical efficiency of the generator, both the mechanical output power of the engine and the total thermal to electrical efficiency could be calculated. For this project the generator will also provide motive power to start the Stirling engine, as it will not be self-starting. The generator chosen in [14] to fit these criteria is depicted in Figure 2.22. It is a 3 phase, permanent magnet synchronous generator, with a rated speed of $480\,rpm$, rated power of $1000\,W$, and a rated voltage of $48\,V$.

Figure 2.22: Generator [14]

2.6.6 HEAT EXCHANGERS

The purpose of the heat exchangers is to transfer thermal energy from the source or sink to or from the working fluid. This is most effectively achieved with a large heat transfer area and materials with good heat transfer properties. In the case of this project the thermal source was chosen to be hot water and the thermal sink, cold water. Water was chosen because it is cheap, accessible, easy to pump, suitable for the design temperatures and has a good heat transfer coefficient. The chosen design was the fin and tube heat exchanger shown in Figure 2.23. Copper tubing was chosen because of its availability and heat transfer properties. Aluminium was the chosen material for the fins because of its cost, weight, and heat transfer properties. The aluminium fins were stacked up on copper tubes with aluminium spacer washers in between. The stack of fins and washers was then clamped down using threaded brass tube. Thermal grease compound was used on all the washers and fins to improve the thermal contact between the copper tubes and aluminium fins.

Figure 2.23: Constructed heat exchanger installed within displacer chamber [14]

With the designed output power of $500\,W$ and a predicted efficiency of around 5% [14], the heat exchangers would need to provide greater than $10\,kW$ of thermal energy to the working fluid. The shape of the heat exchangers was chosen to be a $40°$ wedge of the displacer cylinder. This meant that both exchangers and the regenerator combined would fill one third of the displacer cylinder. With the water flow rate specified to be $100\,ml/s$, it was calculated that an area of $8.1\,m^2$ would be required per heat exchanger to provide sufficient heat transfer. This was calculated to translate to 150 aluminium fins per heat exchanger, each with a surface area of $0.054\,m^2$.

3. DISPLACER

This chapter gives a brief description of the original displacer design and the level to which it had been completed before work began on this project. An account of the new work completed on the displacer and displacer actuation system is then detailed. This includes full schematics of the electronics and the software used to control the displacer. Testing of multiple actuation configurations was undertaken resulting in an updated displacer design. The design decisions and chosen construction techniques used to create this new design are also detailed.

3.1 ORIGINAL DESIGN

The displacer design developed in [14] consisted of an aluminium shell filled with HP35 expanded polyurethane foam. This was connected to a central PVC cylinder which provided both support and a smooth flat surface to support sliding seals. The PVC cylinder was then connected to the aluminium drive shaft via two aluminium disks as seen in Figure 2.17. The actuation system was initially designed to be a single stepper motor driving the aluminium shaft via a 10:1 gearbox. After initial testing of this setup it was decided that more power would be required to actuate the displacer at the design frequency of 2Hz. A new drive system was proposed utilising two stepper motors and driving the displacer through a 2:1 gearing ratio. A more detailed description of the original design is given in section 2.6.2 Displacer.

3.2 EXTENDED DESIGN AND TESTING

Because it had been four years since the completion of the previous project [14], it was decided that the single motor setup would be re-tested. This would provide an opportunity to gain familiarity with the components and software while also verifying the previously obtained results.

3.2.1 SINGLE MOTOR TEST BENCH

Figure 3.1 depicts the single motor test bench setup. The stepper motor, on the left, is a 2 phase, 1.8° step angle, hybrid M1343061 Lam Technologies stepper motor. When used in a bipolar configuration it has a holding torque $12.1\,Nm$ with a maximum phase current

of $10\,A_{rms}$. It is driving the flywheel, on the right in Figure 3.1, through the Anaheim Automation 10:1 gearbox in the centre. The $500\,step/revolution$ incremental encoder, far right in Figure 3.1, provided positional feedback to the motor controller. The stepper motors were controlled using an Advanced Micro Systems (AMS) IBC-400E stepper motor controller. This provided step and direction outputs for speeds up to $60{,}000\,steps/second$. It also provided limit, home, go, and soft stop inputs, with an input range of 5 to $28\,V$, along with 3 programmable user input/output (IO) ports. It also had provision for encoder feedback to provide closed-loop operation. The controller contains 512 bytes of non-volatile (NV), electrically erasable programmable read only memory (EEPROM) for long term data storage, and 512 bytes of "shadow" RAM (random access memory) for fast program operation. The controller was connected to a Lam Technologies DS1078 stepper motor driver to provide the necessary power to run the motor. The DS1078 used a direct current (dc) supply voltage of $90\,V$ to supply an effective phase current of $10\,A_{rms}$ and peak current of $14.1\,A_{peak}$.

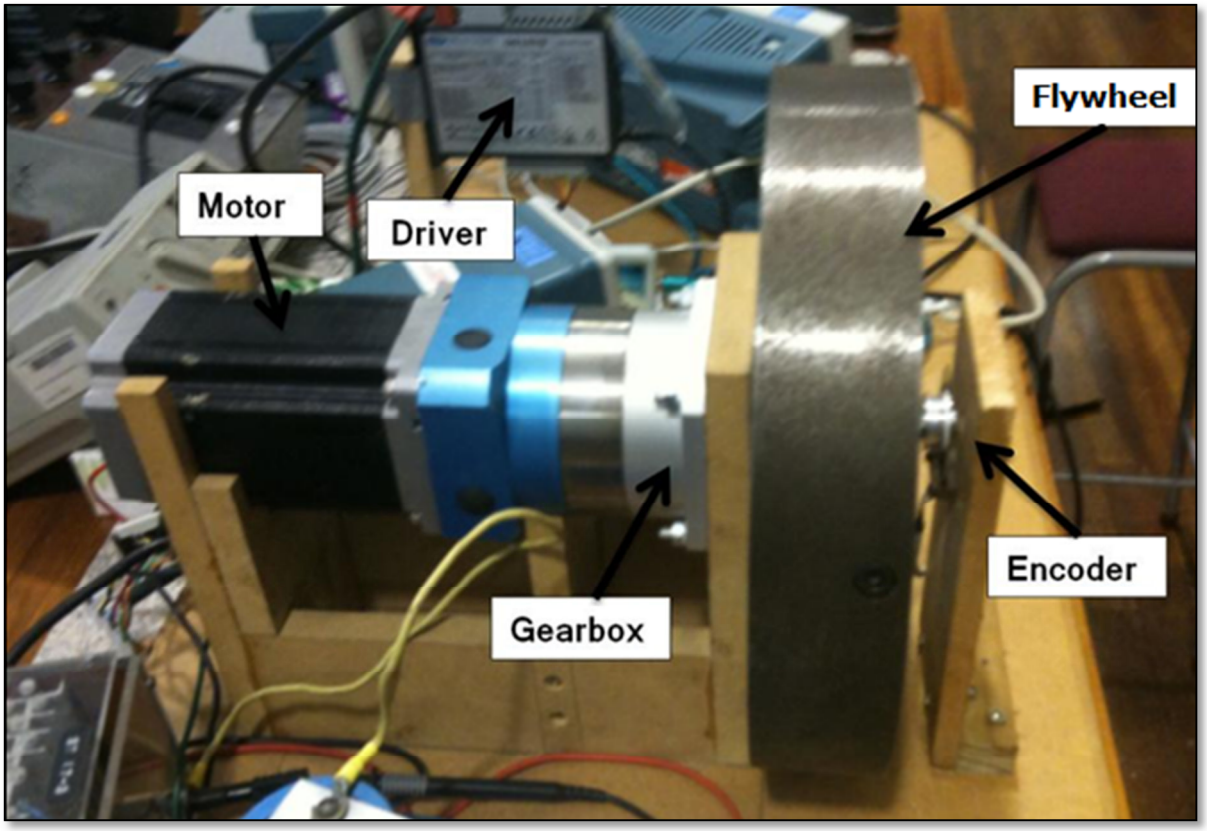

Figure 3.1: Stepper motor test setup

The controller used an ASKII based programming lanquage where letters represented functions and the following numbers represent the operands. For example, “V” was the function to set the maximum slew speed after acceleration from the initial velocity. The slew speed was the number of steps the motor would rotate per second. The number following the V would set the slew speed in steps per second. The controller was designed to be programmed with a serial terminal called AMS cockpit; however, because of the aging software this could not be achieved on a Windows 7, 64 bit operating system, as seen in Figure 3.2.

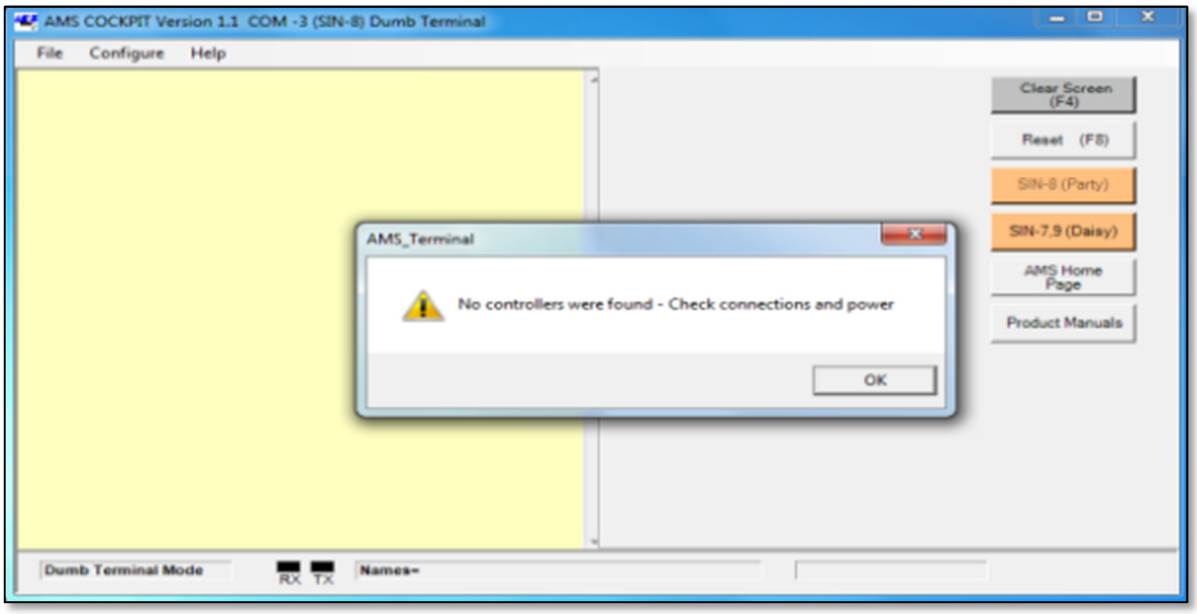

Figure 3.2: AMS Cockpit would not communicate with the IBC-400E stepper motor controller on a Windows 7 OS

To overcome this problem a hyper terminal was used to communicate with the controller. To achieve this, a script had to be developed to convert the control code into the text based language used by the controller. This was achieved through the use of Cygwin (Figure 3.3), a Unix-like command line interface for windows, and Sed, a text stream editor.

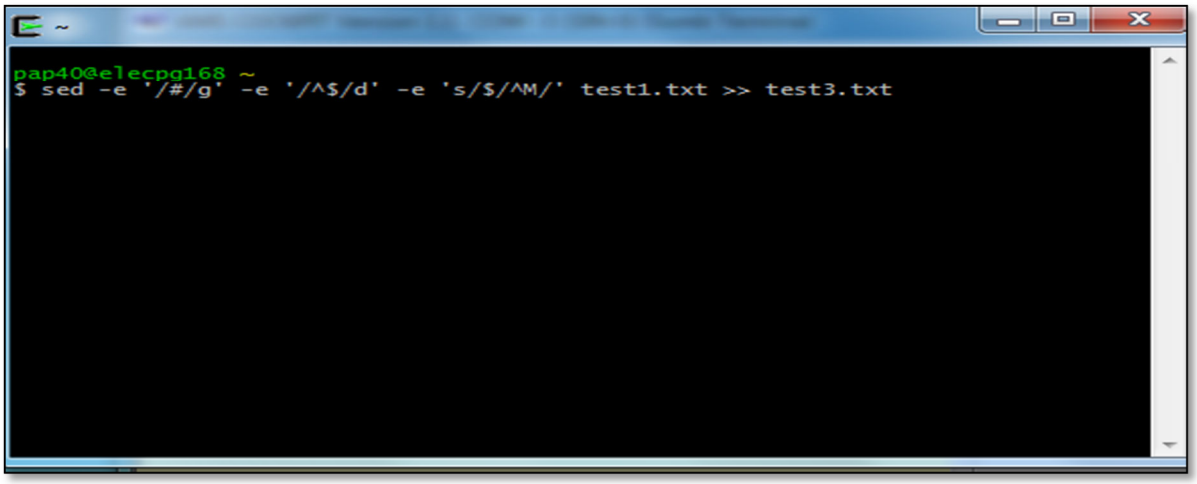

Figure 3.3: Cygwin Terminal used to compile stepper motor code wit sed text stream editor

The control code was written in Notepad, a simple text editor. "#" symbols were placed in front of all comments as seen in Figure 3.4(left). Then after being run through the text editor the code was ready to be programmed onto the controller, Figure 3.4(right).

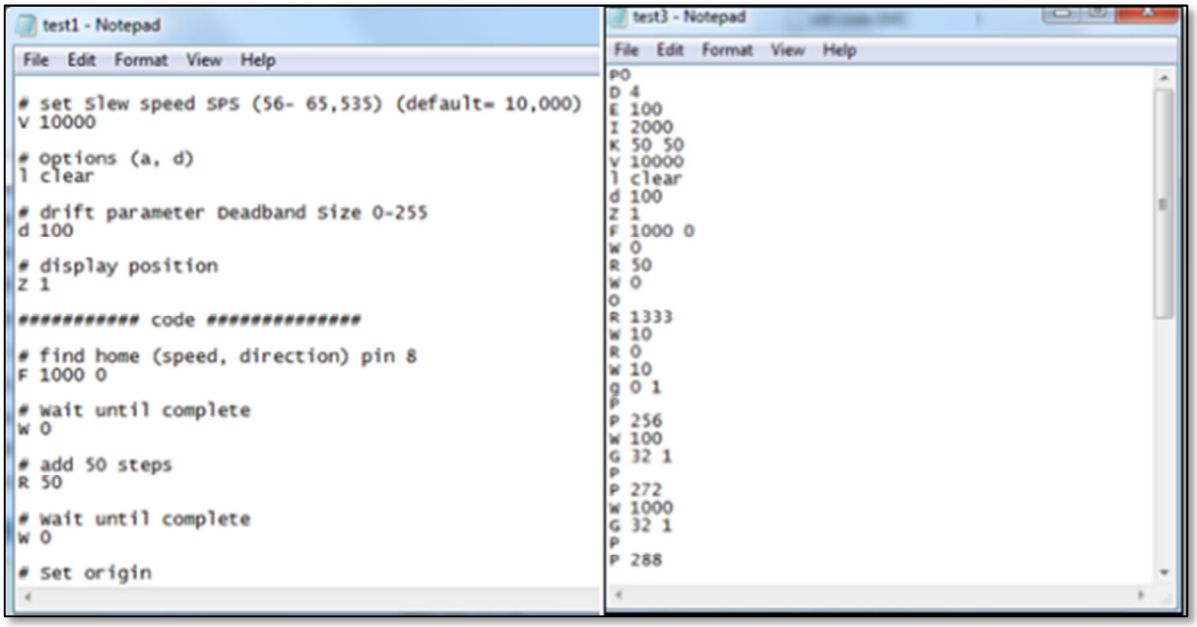

Figure 3.4: Stepper motor commented Code (left) stepper motor compiled code (right)

Then to program the code onto the controller a terminal called RealTerm was utilised as seen in Figure 3.5. This terminal could connect with the controller via a serial port and transmit the compiled code using RS-232 protocol with a baud rate of 9600 bits per second.

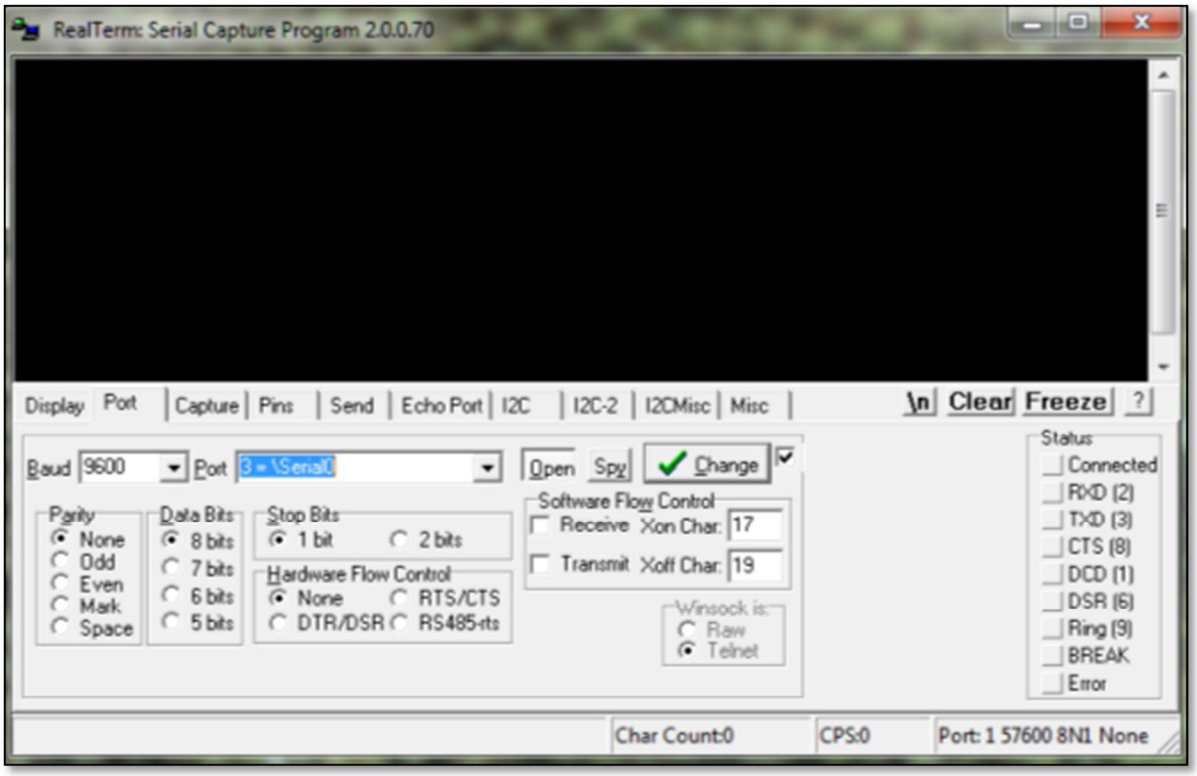

Figure 3.5: Realterm serial communication terminal used to program stepper motor controller

The stepper motor drivers were configured with a LAM Technologies software package called UDP commander 1.70, shown in Figure 3.6. This software was capable of setting the motor resolution, motor current, current reduction time and percent. It also had the capability to manipulate the drive signals applied by the controller and set alarms based on events such as over voltage or phase shorts.

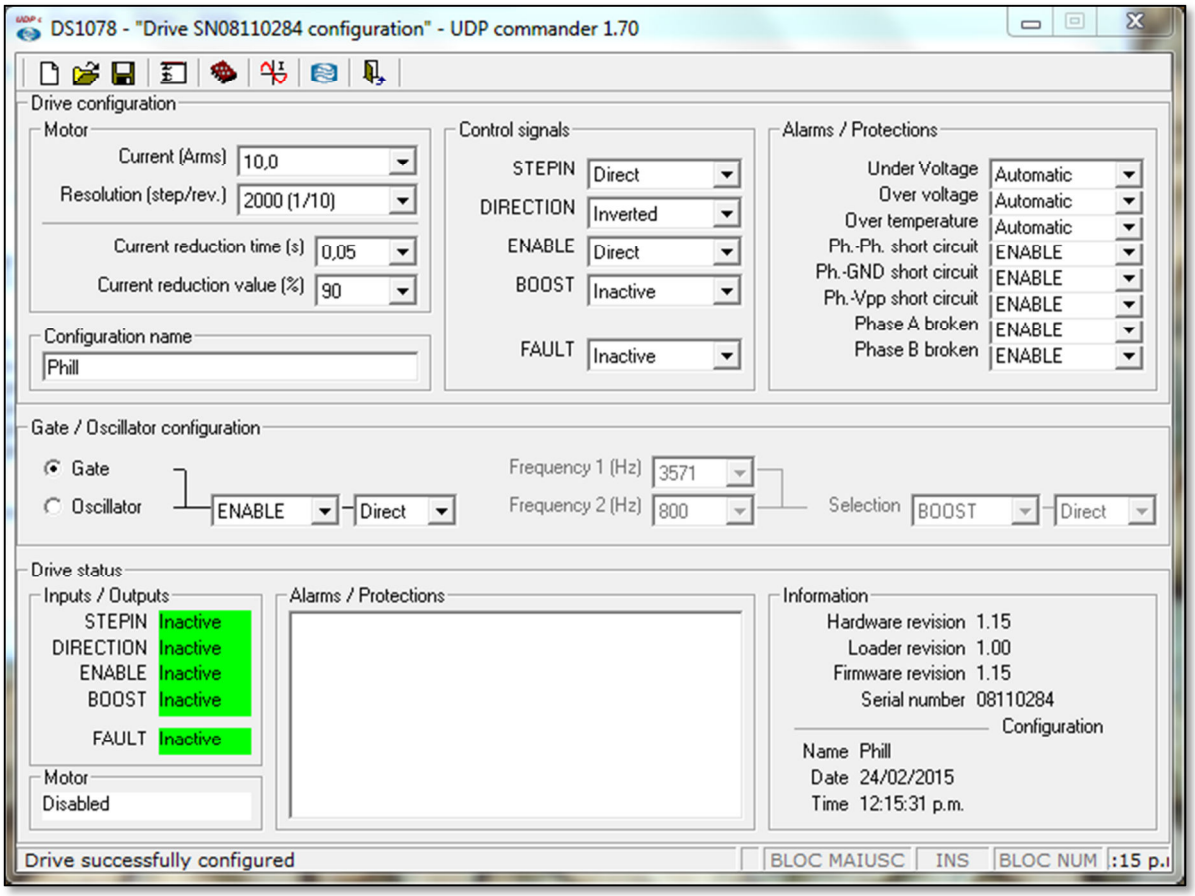

Figure 3.6: UCP commander 1.70 user interface used to change motor driver settings

To check that the maximum power was being applied to the motors by the driver, measurements were taken of the motor phase current as shown in Figure 3.7. The phase current was measured to be an average of $10\,A_{rms}$, which was the motor driver's maximum output. Likewise the phase voltage peaked at $90\,V_{dc}$ which was the motor driver supply voltage. This indicated that the driver/motor combination was operating at its peak power output.

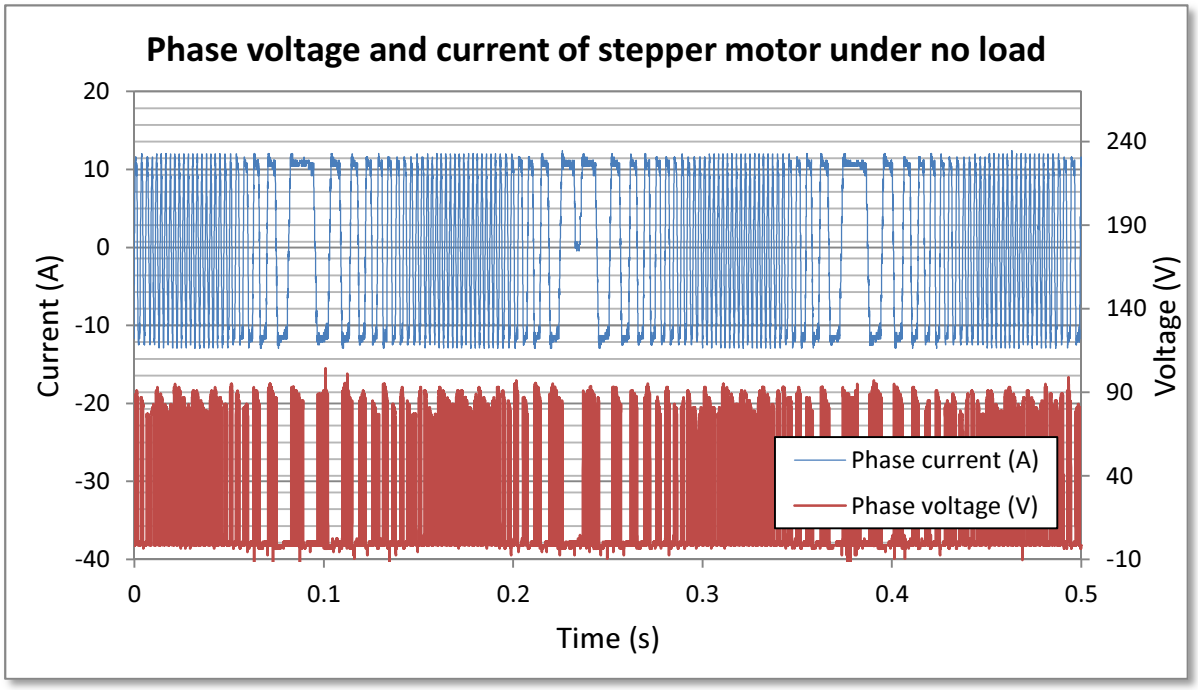

Figure 3.7: Phase voltage and current of stepper motor showing that the driver is supplying the full 10Arms to the stepper motor.

Once familiarity was achieved with the stepper motor control systems a flywheel with a rotational inertia of $0.1598\,kg.m^2$, which was estimated to be similar to the displcer, was attached to the rotor. The motor was then attempted to be run at the engine design frequency of $2\,Hz$. This meant that the displacer needed to rotate 120° and then back to its original position in $0.5s$. The parameters that had the biggest effect on the performance of the system were the acceleration, deceleration, initial speed and maximum speed settings. The initial speed variable was "I" and the operand specified the initial velocity in steps per second. The maximum slew speed, in steps per second, was specified with the variable "V". The acceleration and deceleration were varied with a parameter denoted by "K", which was followed by two operands. The first operand controlled the speed at which the motor accelerated and the second the speed at which it decelerated. These variables had no physical units but altered the time taken to ramp from the specified initial speed to the specified maximum slew speed and vice versa. Larger values represented slower acceleration and deceleration and smaller values represented faster acceleration and deceleration. These variables were all tuned to try and achieve the best performance characteristics possible. The initial speed variable was gradually increased until the motor stalled when a move command was issued. This indicated that the controller was trying to

start the motor at a speed of which it was not capable. After setting the maximum achievable initial speed, the maximum slew speed was set. This was set to the maximum value allowed in the software of 60,000 steps per second. The variable that had the most effect on the achievable displacer actuation time was the acceleration and deceleration. Again the acceleration and deceleration variables were decreased until the motor stalled when atempting the specified motion.

Figure 3.8 shows the stepper motor phase current under load (purple trace). This indicates that the motor driver was supplying the maximum specified $10A_{rms}$ and the motor was producing its maximum power output for this motor/driver combination.

Figure 3.8: Stepper motor phase current under load (purple trace)

This testing verified the conclusion in [14] that a single stepper motor would not be sufficient to actuate the displacer at the desired speed. It was discovered that a sinusoidal displacement motion (velocity profile) provided the fastest response. The maximum frequency that could be achieved with this setup was $1.2\,Hz$ using a sinusoudal displacement motion, as illistrated in Figure 3.9 (red line). A frequency of only $0.83\,Hz$ was achieved utilising non-sinusoidal motion, as shown by the blue line in Figure 3.9.

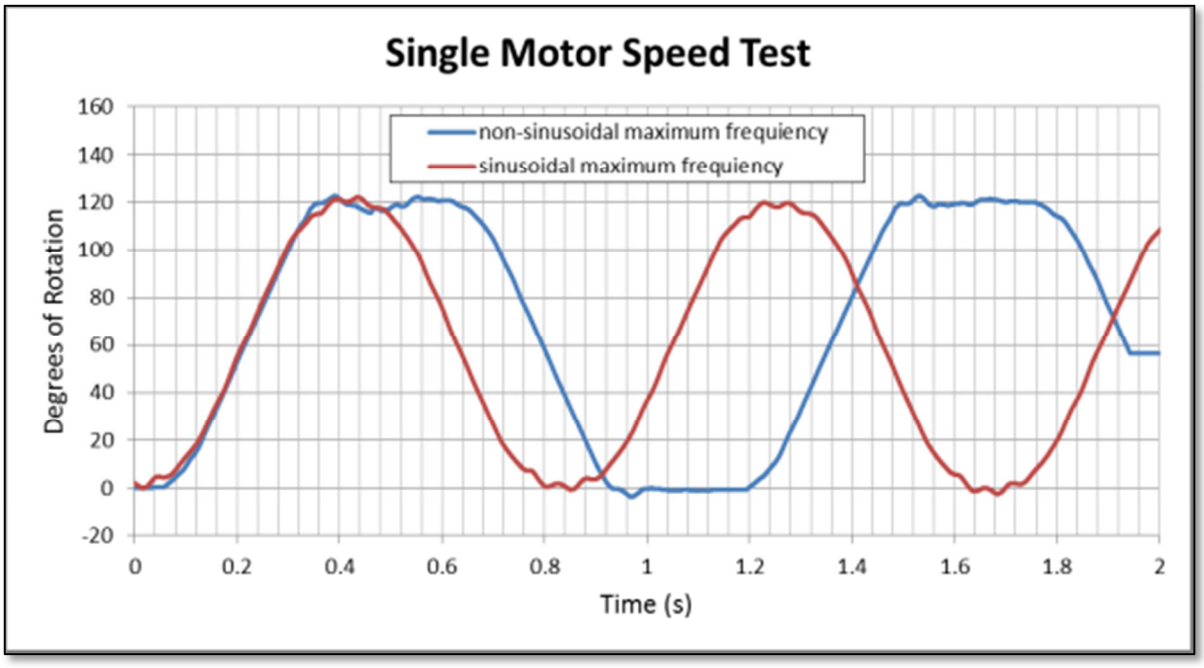

Figure 3.9: Maximum frequency reached with a single stepper motor, sinusoidal 1.2Hz, non-sinusoidal 0.85Hz.

If higher speeds of acceleration and or deceleration were attempted the motion became unreliable. As Figure 3.10 illustrates, the angle of rotation is either falling short or overshooting the required 120°. The spikes represent a jerky motion resulting from the controller trying to correct the motor position based on the information provided by the optical encoder.

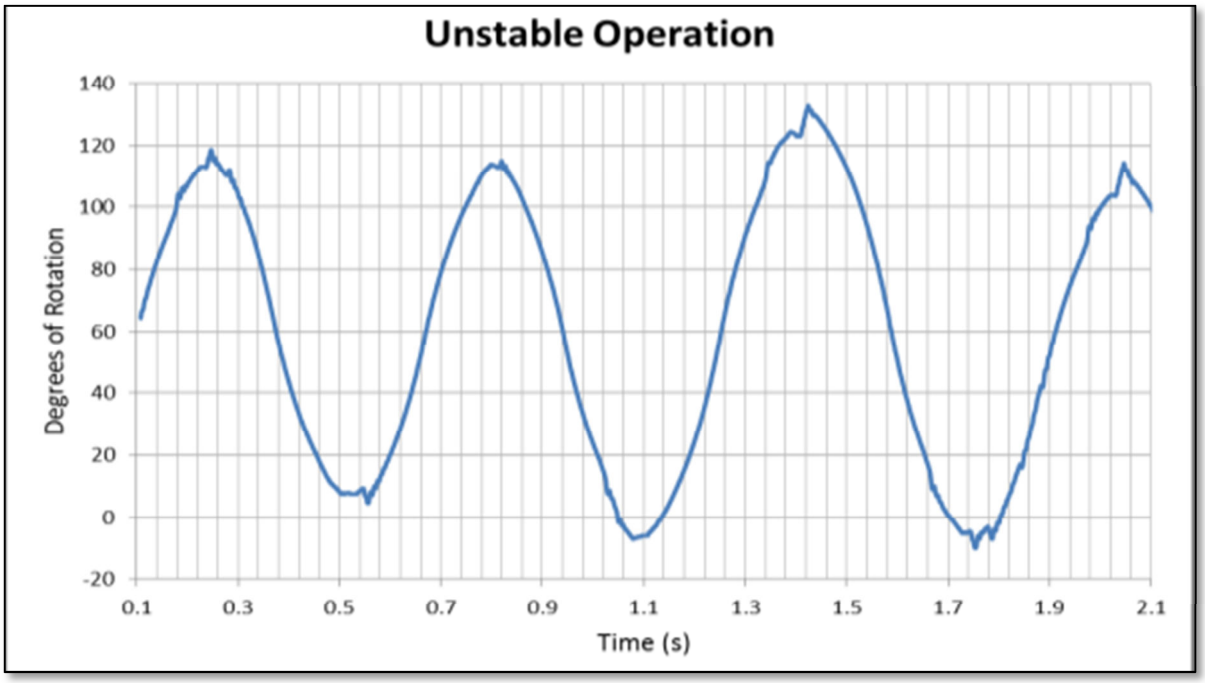

Figure 3.10: Unreliable motion resulting from attempting higher frequency operation

3.2.2 Dual Motor Test Bench

A second test rig, shown in Figure 3.11, was fabricated to assess whether the dual motor setup proposed (but not tested) in [14] would be capable of achieving the desired speed of $2Hz$. The two motors were connected to two gears which were secured either side of a third larger gear, creating a gearing ratio of 2:1. The output shaft was connected to a flywheel which simulated the rotational inertia of the displacer.

Figure 3.11: Dual motor test bench setup

The schematic of the stepper motor control setup for this duel motor test rig is shown in Figure 3.12. The controller provides step, direction and a moving signal to the motor drivers. The drivers then convert these signals into drive signals for the stepper motors. The stepper motors were connected to the drivers in bipolar parallel configuration. An incremental encoder was connected to the shaft of one of the motors which then provided positional feedback to the controller. There were also two limit switches, two IR transmitter/receivers and three push buttons connected to the controller. The limit switches stopped the motors from proceeding in the current direction of travel if activated. The IR transmitter/receivers were used to interface the timing of the displacer's actuation with the rest of the engine (especially the power piston phase). The push buttons provide local go, soft stop, and home controls without the need for a terminal connection.

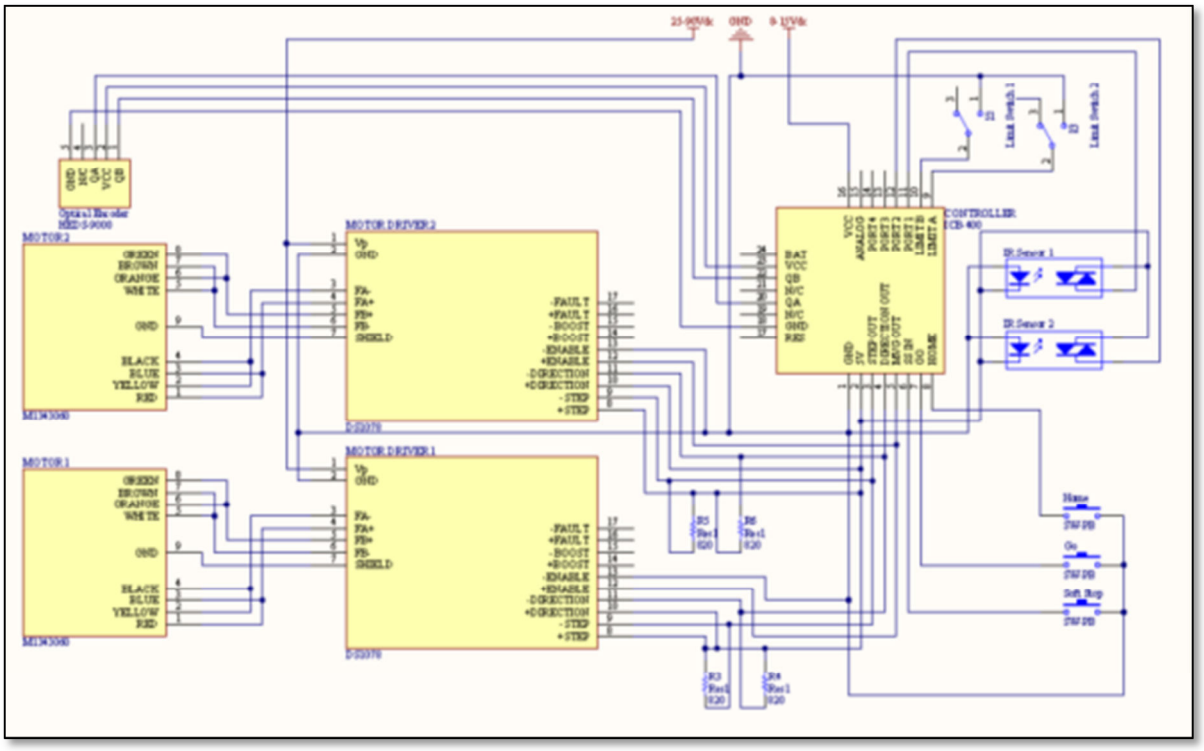

Figure 3.12: Displacer actuation control schematic

Testing with the dual motor setup again showed that the target frequency of $2\,Hz$ was unachievable with the flywheel's rotational inertia. The maximum achieved frequency was increased to $1.53\,Hz$, as shown by Figure 3.13. This was achieved with an acceleration variable of 5, a deceleration variable of 5, an initial speed variable of $5000\,steps/s$ and a maximum speed variable of $60{,}000\,steps/s$.

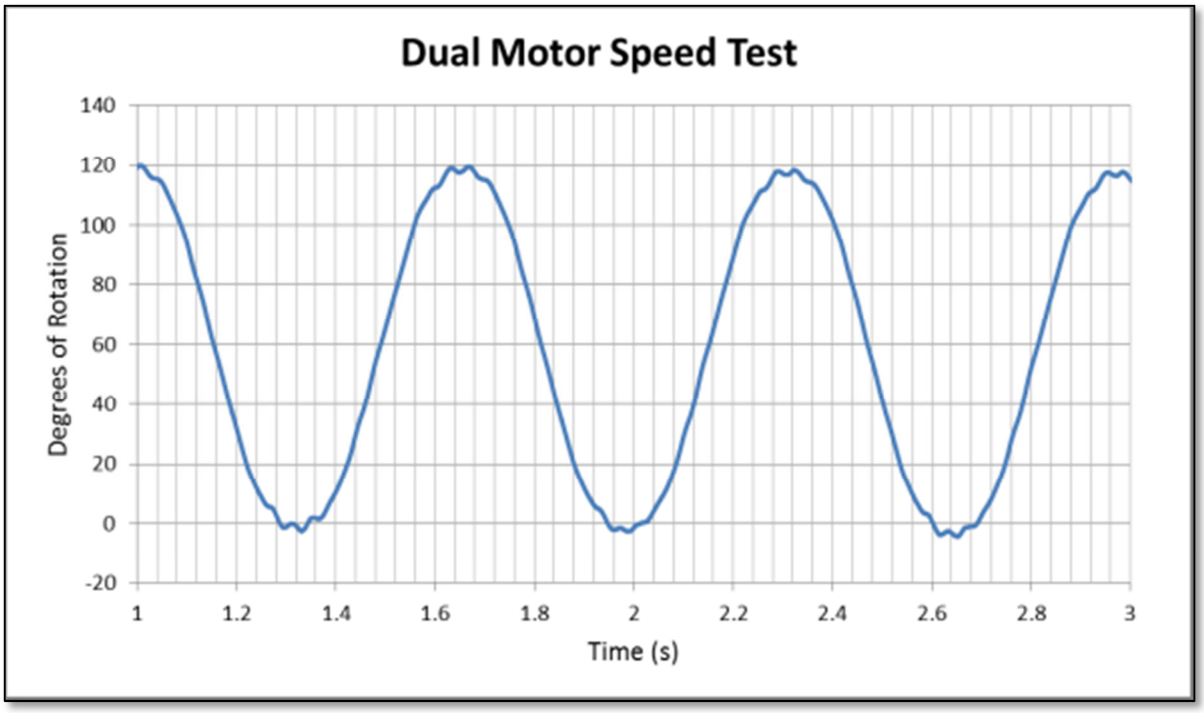

Figure 3.13: Dual motor maximum achieved frequency of 1.53Hz

As the stepper motors could not actuate the dummy load at the required speed, there were two options to increase the speed of the displacer. Either the displacer's rotational inertia had to be reduced, or more powerful motors would be required. As the motors were a rather expensive component, the reduction in weight and moment of inertia of the displacer was the most cost effective solution. To assess the extent to which the displacer would need to be modified, several more tests were carried out with flywheels of varying moments of inertia.

3.2.3 Motor Characterisation

To assess the maximum moment of inertia that the dual motor setup could actuate at the desired $2\,Hz$, four flywheels of varying moments of inertia were connected to the output shaft. The acceleration, deceleration, maximum speed and initial speed variables were then varied to ascertain the maximum frequency for each flywheel, whilst maintaining a stable displacement actuation. In order to calculate the moment of inertia for each load a SolidWorks model was developed. SolidWorks can calculate model's physical properties, including the moment of inertia, as long as the material's density is specified. The

SolidWorks models, moment of inertia, mass and maximum achieved frequency are shown in Table 3.1.

Table 3.1: Calculated flywheel moment of inertia

Flywheel model	Moment of inertia $(kg \cdot m^2)$	Mass (kg)	Maximum frequency (Hz)
	0.1598	11.2	1.53
	0.0643	9.51	2.63
	0.0127	3.9	3.45
	0.0045	2.51	3.57

The moment of inertia was then was plotted against the maximum achieved frequency to produce Figure 3.14. The horizontal error bars represent a 5% error in the estimated moment of inertia and the vertical error bars represent a 2% error in maximum displacement frequency. The test points were fitted with a best fit trend line of $y = 3.6958e^{-5.487x}$ and the maximum allowable moment of inertia of the displacer was calculated by finding the intersection of this trend line with the desired engine frequency of $2\,Hz$. As expected the displacer design in [14] had a higher moment of inertia than the calculated limit of $0.112\,kg \cdot m^2$.

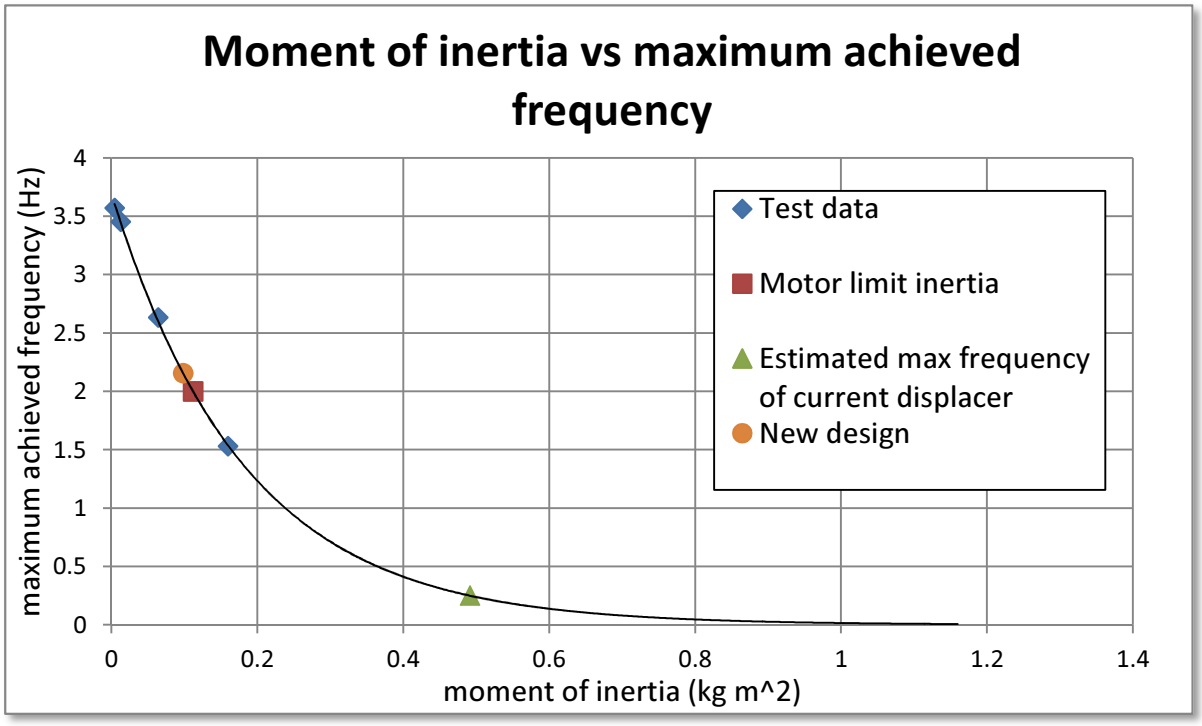

Figure 3.14: Estimate of stepper motor capabilities based on multiple flywheel tests with differing moments of inertia

3.3 Displacer Redesign

Because the displacer design exceeded the rotational inertia that the dual motor setup could actuate at the desired frequency, three options were considered to rectify this. Firstly, new more powerful motors could be purchased to ensure the desired frequency could be achieved; secondly the displacer could be redesigned and built to allow the current motors to achieve the desired frequency. The third option would be to devise an entirely new displacement actuation system, possibly using linear actuators, springs or inflatable bladders. The decision was made to redesign the displacer, mainly because this was the most cost effective solution.

When deciding on the possible options for redesigning the displacer, several methods were considered. The main decisions that needed to be made were whether or not to reduce the size of the displacer and how much of the original displacer to keep. It would be possible to make the displacer much thinner as long as it provided sufficient insulation between the hot and cold regions. This would reduce the weight and moment of inertia considerably; however it would also increase the length of travel required. In addition, the working volumes of the expansion and compression space would be altered significantly.

While this may not necessarily be a bad thing, it was decided to keep the displacer the same size to maintain the initial design volumes, at least until initial testing has been carried out.

Table 3.2: Original displacer materials

Part	Material	Density (kg/m^3)	Moment of Inertia $(kg \cdot m^2)$
Internal Foam	Polyurethane Foam	35	0.2625
Drive Shaft	Aluminium	2705	0.0007
Shaft Supports	Aluminium	2705	0.0034
Pipe	PVC	1300	0.0336
Top & Bottom Skin	Aluminium	2705	0.0646
Sides Skin	Aluminium	2705	0.0411
Central Spine	Aluminium	2705	0.0216
Reinforcing Rods	Steel	7850	0.0213
		Total	**0.4488**

The strategy for redesigning the displacer was to remove enough rotational inertia so as to allow the dual stepper motors to actuate it at the design frequency. This involved removing as much weight as possible, with increasing importance the further from the centre of rotation (as this has more effect on increasing the inertia). Table 3.2 shows the parts that made up the original displacer, along with their densities and moments of inertia taken from the centre of the aluminium drive shaft, as shown in Figure 2.17. Although the foam had a very low density, it took up a large volume and thus was the major contributor to the overall moment of inertia. It was decided to remove the foam, reinforcing rods, aluminium casing, top, bottom and central spine. The remaining aluminium shaft, shaft supports and PVC pipe had a combined moment of inertia of $0.0377\ kg \cdot m^2$. This meant that any new additions must have a combined moment of inertia less than $0.0743\ kg \cdot m^2$. The design chosen to achieve this is shown with a 3D SolidWorks model in Figure 3.15.

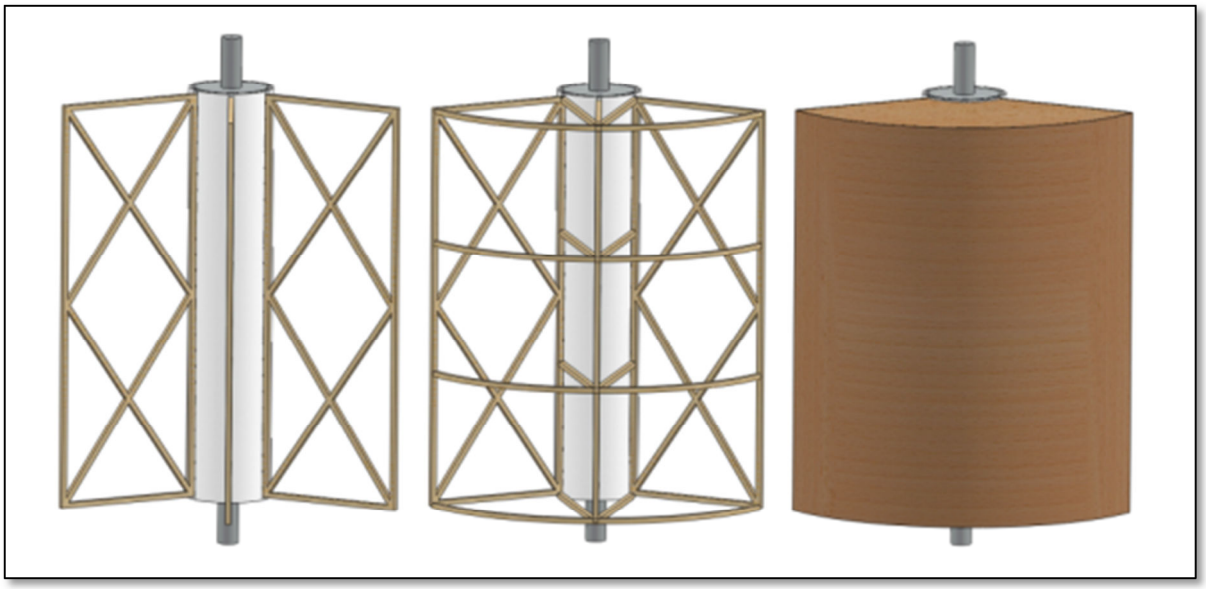

Figure 3.15: SolidWorks Model of Displacer Design

Firstly three lightweight braced pine (or equivalent density stiff material) frames will be constructed and screwed to the PVC cylinder. The central frame will be braced back to the base of the exterior frames, as it will be supporting the sliding seal and will experience horizontal forces. Axial ribs will then be cut and secured to the outside edge of the frames. Finally to provide a light weight case, Depron® foam will be cut to shape and glued to the supporting frames. Depron® is an extruded polystyrene foam product, It is extremely lightweight, rigid and moisture resistant [42]. The parts and their respective densities and moments of inertia from the centre of the drive shaft are shown in Table 3.3, with the total moment of inertia estimated to be $0.0984\ kg \cdot m^2$.

Table 3.3: Material Properties New Design

Part	Material	Density (kg/m^3)	Moment of Inertia $(kg \cdot m^2)$
shaft	Aluminium	2705	0.0007
shaft supports	Aluminium	2705	0.0034
pipe	PVC	1300	0.0336
Top & bottom	Depron Foam	33	0.0019
circumference	Depron Foam	33	0.0083
Circumference ribs	Pine	340	0.0109
Sides	Depron Foam	33	0.0138
Reinforcing struts	Pine	340	0.0006
Frames	Pine	340	0.0251
		Total	**0.0984**

The aim of the displacer seals is to prevent the working fluid escaping past the displacer and short-circuiting the heat exchangers and regenerator. The sliding seals were originally constructed with a fabric material bent over and clamped between two aluminium strips. This construction technique is not compatible with the new hollow displacer design so a new solution is required. The choice of seal will be made based on which can provide the best seal with the least friction and at the lowest cost. The ideal solution would be custom made Rulon seals, however these would be very expensive. There are two other types of seal that are commonly available and may be useful in this application. The first being a nylon brush type seal and the second being the rubber type seal. The brush type seals are likely to provide very little frictional losses when sliding on the polypropylene plastic liner, but may not provide a sufficient seal. The rubber type seals should provide a good seal, but may also create quite large frictional forces when sliding on the polypropylene liner. Further investigation and testing is required before this choice can be made.

3.5 DISCUSSION

In retrospect, it would have been beneficial to do more calculations on the capabilities of the stepper motors before starting testing. This possibly would have identified the inertia/power problem much sooner, saving both time and effort. The decision was made to keep the central components of the original displacer because they should have little effect on the total moment of inertia. Also by keeping most of the original structure, the

cost and time to manufacture were kept low. The current displacer design's moment of inertia is calculated to be just short of the calculated motor limit; this is not best design practice and is likely to cause issues during testing. There are also a lot of sliding seals on the current design; these will add frictional losses when rotating at the design frequency of $2\,Hz$, which have not been included thus far in the calculations. Because of these issues it may be necessary to completely redesign the displacement mechanism if the displacer form is kept the same

The new displacer design has no internal insulation, it will rely on the external Depron® foam shell and the air trapped within for insulation. This should provide sufficient insulation because of the LTD and also the thickness of the current displacer design. Because the current design is hollow it would be crushed when the displacer chamber was pressurised if it was completely sealed. To prevent this, a pin hole could be utilised to allow pressure equalisation during engine pressurisation. It must however be small enough not to allow working fluid transfer during operation, as this would have a detrimental effect on the engine performance by introducing dead space.

During testing the method of connecting the flywheels to the stepper motor shafts were grub screws. These would wear through relatively quickly due to the large acceleration and deceleration forces exerted by the desired displacement motion. This was also the proposed connection method for the displacer to the stepper motors in [14]. The current design calls for four grub screws, it may however be necessary to add a keyway to stop the shaft or screws wearing out. If this is the case it would be wise to include some type of mechanical fail safe, such as a split pin, for safety purposes. This would prevent extensive damage to the heat exchangers or motors if something was to go wrong with the stepper motor control.

4. REGENERATOR

The basic structure of the regenerator, including the shape and fill material, had been specified in the previous thesis [14]. The shape specified was a 40° wedge the same size and shape as the heat exchangers. Wire wool was identified as the preferred fill material based on cost and performance characteristics. In this project, investigations were carried out as to how an even flow could be achieved within the varying length regenerator shape. Suitable construction materials were also specified and the regenerator was designed and constructed.

4.1 DESIGN

Regenerator design is a balancing act between several properties to achieve the maximum effectiveness with as few losses as possible. Heat capacity and heat transfer want to be maximised, while flow losses and dead space must be minimised. For maximum heat capacity, a large volume regenerator containing thick wire screens is required. For maximum heat transfer a large heat transfer surface area is required. This is best achieved with a large volume matrix containing fine wire screens. To minimise flow losses a highly porous small matrix is required. Porosity, designated by Ø, is defined as the void volumes within the regenerator over the total regenerator volume. To minimise dead space a small volume, a low porosity matrix is required. An optimal compromise must therefore be found as illustrated in Figure 4.1.

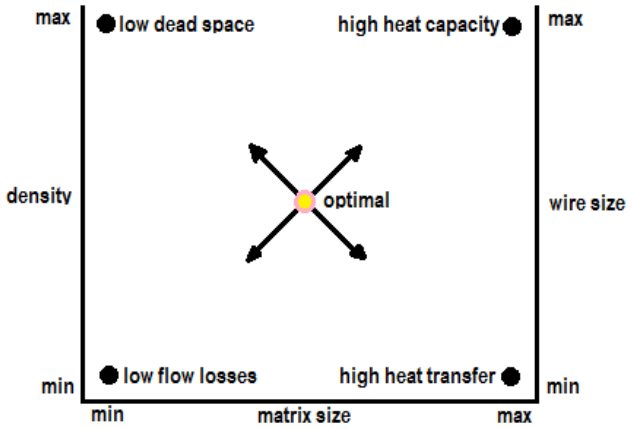

Figure 4.1: Representation of conflicts in regenerator optimisation

For this project's engine, the regenerator has been designed to fit into the space between the hot and cold heat exchangers, constraining its physical dimensions. Because of the engine's configuration, this space does not have a constant length. This complicates the design of the regenerator as the regenerator length has an impact on many of the design parameters such as porosity and wire diameter. Figure 4.2 shows the regenerator shape with increasing axial length from inside, L_i, to outside, L_o. If the fill material was packed to an even density, ρ_{fill}, then the fluid friction would be lower along the inside edge where the length through the regenerator is smallest. This would result in a higher fluid flow rate on the inside edge. Conversely the length through the regenerator would be greatest at the outside edge, increasing fluid friction and decreasing fluid flow rate, as shown in Figure 4.2(a).

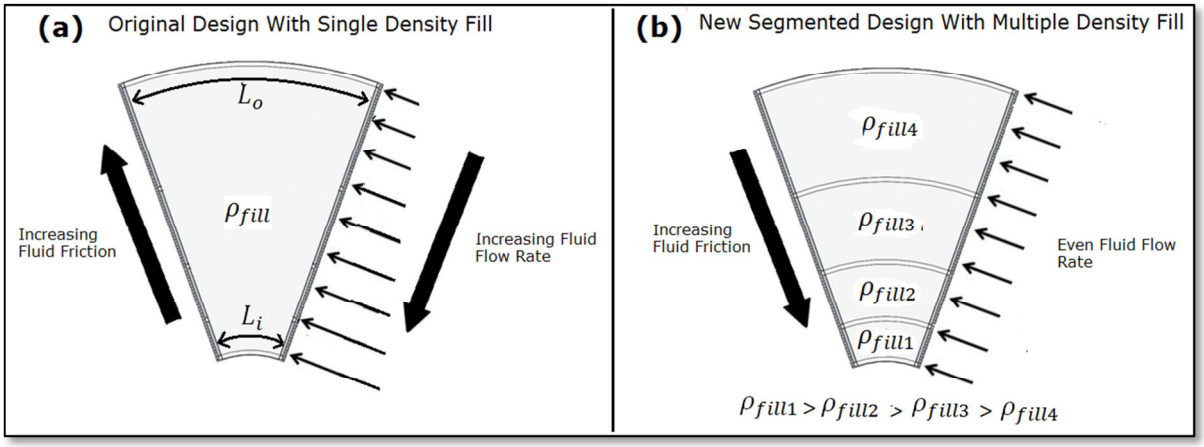

Figure 4.2: (a) Variable fluid flow through regenerator with uniform fill material density, (b) Fluid flow controlled within regenerator through the use of internal curved panels and multiple fill density

It was decided to construct the regenerator in such a way as to provide an even fluid flow. In this way the fluid should flow axially and not be forced to move radially when passing through the regenerator. To achieve this, curved panels would be placed inside the regenerator to create distinct sections, as shown in Figure 4.2(b). This meant that the parameters in each section could be altered independently to achieve the desired flow rate. This also meant that each section was effectively an independent regenerator with different operating conditions, with the combined properties of the individual sections constituting the desired overall regenerator properties. The design parameters that had to be decided were; firstly, the number of segments that the regenerator was split into, to most effectively

create an even flow whilst still being physically reasonable to build, and secondly, the amount of wire in each section to provide the desired flow rate with maximum effectiveness. It was decided to use only a single wire width throughout the regenerator. This meant that the wire could be bought in bulk, reducing the cost and also reducing the complexity of the design process.

4.1.1 SIMULATION

To try and optimise the number of sections used in the regenerator a Matlab™ file was created to evaluate the effects on the working fluid flow when passing through the regenerator. Firstly the variables that were assumed to be fixed were assigned; these are shown in Table 4.1. The independent variables were then defined and limits specified as shown in

Table 4.2.

Table 4.1: Simulation model fixed variables

Variable	Designator	Value	Units
Engine frequency	f	2	Hz
Specific heat capacity of steel	C_m	437	$J/kg \cdot °C$
Dynamic viscosity of working fluid	μ	0.0000185	$kg/m \cdot s$
Specific heat capacity of air	C_p	1000	$J/kg \cdot K$
Density of working fluid	ρ	12	kg/m^3
Wire material density	ρ_{wire}	7800	kg/m^3
Regenerator width	W_r	0.3	m
Regenerator height	H_r	0.806	m
Outside regenerator radius	r_o	0.392	m
Inside radius	r_i	0.093	m
Prandtl number	N_{pr}	0.7	dimensionless
Expansion volume	V_e	0.005	m^3
Compression volume	Vc	0.083	m^3
Wire radius	a	0.05	mm

Table 4.2: Simulation model independent variables

Variable	Designator	Minimum value	Maximum value	Units
Number of segments	N_{seg}	1	10	$integer$
Segment wire mass	M_{wire}	0	10	kg

The best indicator of the resistance to fluid flow was the pressure drop created by the wire wool in a given segment. Initially the pressure drop was calculated using equation 14 [14],

$$P_{drop} = \frac{\mathrm{M}_o{}^2 f_k L}{2\mathrm{R}_h \rho} \quad (14)$$

where M_o is the mass flow rate of the working fluid per unit area, f_k is the matrix friction factor (found using equation 18), L is the average axial length of the regenerator segment, R_h is the hydraulic radius which is equal the $\mathrm{d}_h/4$ (d_h found from equation 20), and ρ is the density of the working fluid. The mass flow rate per unit area of working fluid was found by first calculating the mass of the working fluid that would flow through each regenerator segment every half cycle. This was done by using equation 15.

$$\mathrm{M}_{wf} = \frac{(\pi r_1{}^2 - \pi r_2{}^2)\mathrm{H}_r \rho}{3} \quad (15)$$

Where r_1 and r_2 were the inside and outside radii of a given segment. H_r is the height of the regenerator and ρ is the density of the working fluid. From this the mass flow rate in $kg/m^2 s$ could be evaluated by multiplying the mass flow rate per unit area by twice the operational frequency, f, and dividing by the free flow area as shown in equation 16,

$$\mathrm{M}_o = \frac{2f\mathrm{M}_{wf}}{\mathrm{A}_{ff}} \quad (16)$$

A_{ff} is the free flow area in m^2 and was calculated by multiplying the porosity by the total cross sectional area of the given segment as shown in equation 17 [14].

$$\mathrm{A}_{ff} = \emptyset \mathrm{W}_{rs} \mathrm{H}_r \quad (17)$$

The friction factor was calculated using equation 18, where based on test data for random fibre networks, $\alpha = 192$, $\delta = 4.53$ and $\gamma = -0.067$ [43].

$$f_k = \frac{\alpha}{N_{re}} + \delta N_{re}{}^{\gamma} \quad (18)$$

The Reynolds number, N_{re}, was calculated using equation 19 [14], where μ is the dynamic viscosity of the working fluid in $kg/m \cdot s$, and d_h is the hydraulic diameter of the regenerator material.

$$N_{re} = \frac{M_o d_h}{\mu} \quad (19)$$

The hydraulic diameter is a measure of channel flow efficiency and was calculated using equation 20 [14]. V_{reg} represents the volume of the regenerator segment in m^3 and was calculated using equation 21. S_{reg} represents the regenerator segment heat transfer surface area in m^2 and was calculated using equation 22 [14].

$$d_h = \frac{4V_{reg}}{S_{reg}} \quad (20)$$

$$V_{reg} = \frac{(\pi {r_1}^2 - \pi {r_2}^2)H_r}{9} \quad (21)$$

$$S_{reg} = 4\left[\frac{1-\emptyset}{\emptyset}\right]\frac{V_{reg}}{2a} \quad (22)$$

The regenerator porosity, $\emptyset$, is the ratio of void space within the regenerator segment to total regenerator segment volume. It was calculated using equation 23 [14].

$$\emptyset = 1 - \left[\frac{M_{wire}}{\rho_{wire} V_{reg}}\right] \quad (23)$$

Where M_{wire} is the mass of wire in a given segment in kg and ρ_{wire} is the density of the wire material used in kg/m^3. The convective heat transfer coefficient was then calculated using equation 24 [14], where Y_3 is an intermediate value based on porosity which can be looked up in Table 4.3 [14].

$$h = Y_3 C_p {N_{pr}}^{-\frac{2}{3}} \quad (24)$$

Table 4.3: Table of selected Y_3 values for known values of porosity and Reynolds number [44]

$\emptyset$	$N_{re} < 10^5$
0.95	$Y_3 = 2.75 {N_{re}}^{-0.48}$
0.60	$Y_3 = 0.5 {N_{re}}^{-0.396}$

4.1.2 TESTING

To validate this theoretical model for pressure drop in the regenerator, a test rig was constructed. The objective was to ensure that the pressure drops across different length

sections of the regenerator were accurately represented by the model. Four $32\,mm$ diameter polyvinyl chloride （PVC） tubes of different lengths, $S_1 = 79\,mm$, $S_2 = 113.5\,mm$, $S_3 = 163.2\,mm$ and $S_4 = 233\,mm$ were constructed, each representing a different flow path through the regenerator. These tubes were then packed with wire wool to the density specified in the model. Gauge $\#0$ wire wool was used for these tests, as it most closely represented the $0.05\,mm$ wire radius specified in the model. A regulator was attached to the outlet of an air compressor to supply the air flow. A Turnigy mini anemometer was used to measure the air speed with range of $0 - 30\,m/s$ and an accuracy of $\pm\,0.1\,m/s$. To verify the calculated performance the pressure drop across the wire wool was then measured with a MPXM2010GS silicon piezoresistive pressure transduser. This sensor has a range of 0 to $10\,kP_a$ and an accuracy of $\pm\,10\,P_a$. The setup is depicted in Figure 4.3.

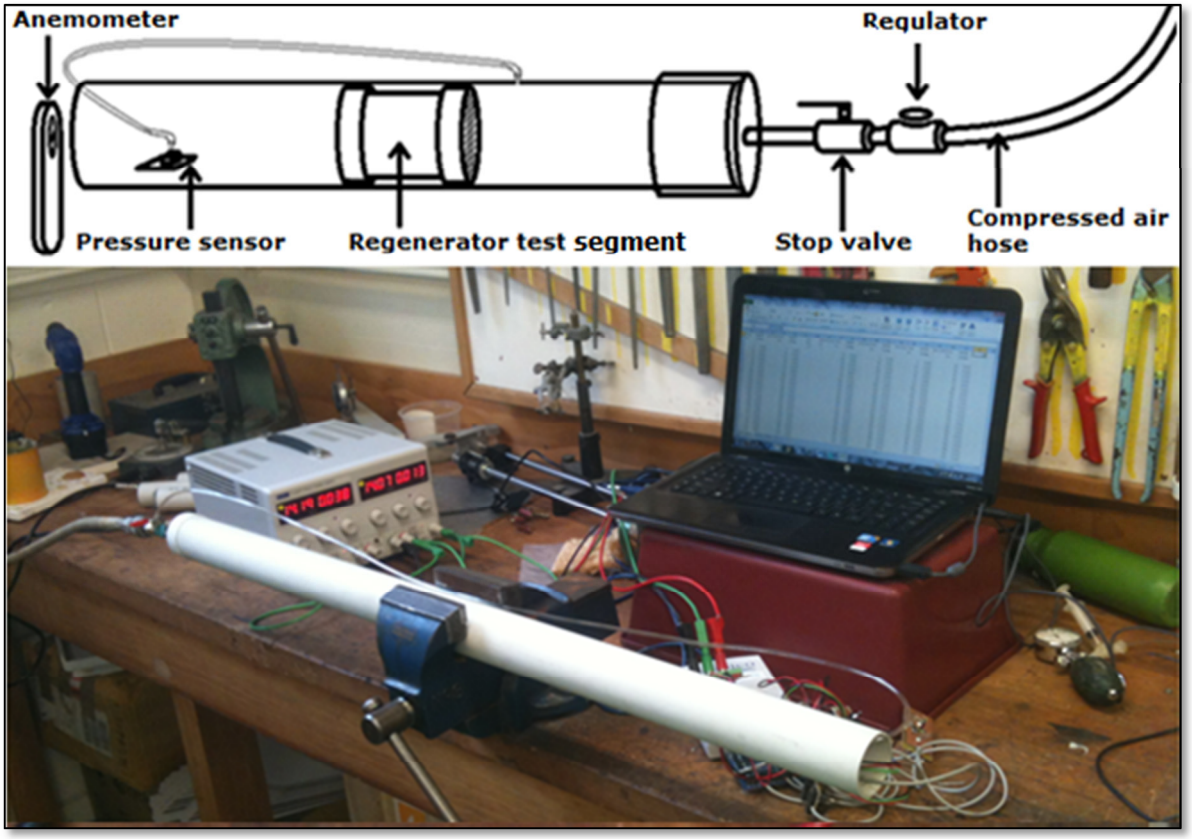

Figure 4.3: Regenerator test setup

Initially tests were conducted with no material inside the tubes. This was done to ascertain the base pressure drop through each containment tube. Subsequent measurements were then adjusted by subtracting these base values. There was also a constant offset in the

sensor measurements of $-0.255\,mmHg$; therefore this was added to all subsequent measurements. Five air speeds were tested for each section ranging from 0 to $3\,m/s$ by adjusting the regulator in the air hose. The first set of measurements showed that the simulation overestimated the pressure gradient at higher airspeeds and underestimated at lower air speeds, as shown in Figure 4.4. To improve the model and better match the experimental results a more detailed simulation was developed.

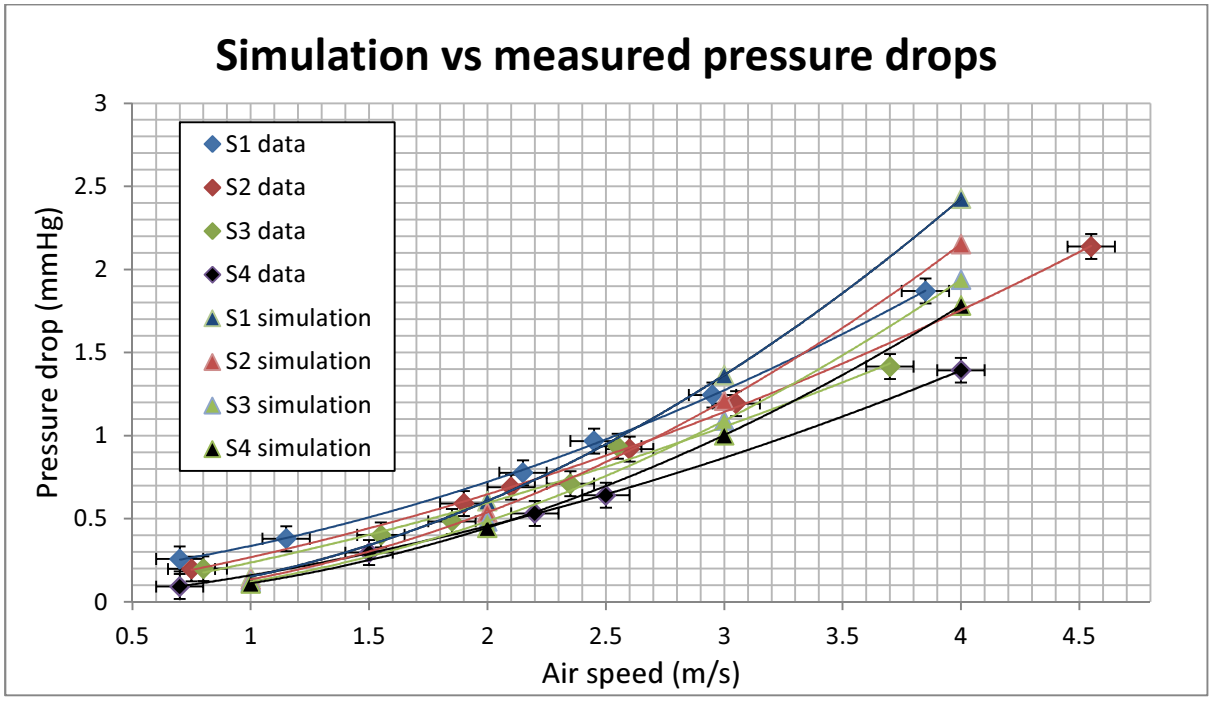

Figure 4.4: Initial simulation overestimating the pressure drop through test segments

The adjusted model used the Darcy-Forchheimer equation, shown in equation 25 [45]. Darcy's law was developed to describe fluid flow in porous media; however it assumes that the pressure gradient is linearly proportional to the fluid velocity [46]. For higher velocities inertial effects can become significant. An inertial term is then added, known as Forchheimer term (second term in equation 25). This term is able to account for the non-linear behaviour of the pressure difference with respect to the fluid velocity [47]. The inertial coefficient (C) accounts for nonlinear effects within the porous media at higher flow rates.

$$\frac{dp}{dx} = \frac{\mu v}{K} + C\frac{\rho v^2}{\sqrt{K}} \qquad (25)$$

dp/dx is the pressure drop across distance dx through the porous media, μ is the working fluid viscosity, K is the porous media permeability, v is the working fluid velocity, C is the inertial coefficient and ρ is the working fluid density. A modified version of the Gebart relationship, given in equation 26 [48], was used to calculate the permeability of the fill material based on several physical characteristics.

$$\frac{K}{a^2} = C_1\left(\sqrt{\frac{1-\emptyset_c}{1-\emptyset}}-1\right)^{C_2} \quad (26)$$

Where a is the wire radius, $\emptyset$ is the wire wool porosity, $\emptyset_c$ is the critical value of porosity below which there is no permeating flow (the percolation threshold), and C_1 and C_2 were geometric parameters used to model different porous materials [48]. The best fit parameters obtained for a random fibre network in [48] are shown in Table 4.4.

Table 4.4: Random fibre model best fit parameters [48]

Parameter Best fit value	Parameter Best fit value
$\emptyset_c$	0.0743
C_1	0.491
C_2	2.31

Using these parameters the permeability was calculated for each section. The inertial coefficient C was calculated using equation 27, where C_f is the matrix friction factor which was calculated with equation 18, using measured values of dp/dx. N_{reK} is the permeability based Reynolds number, which was calculated using equation 29. [49]

$$C = C_f - \frac{1}{N_{reK}} \quad (27)$$

$$C_f = \frac{dp}{dx}\frac{\sqrt{K}}{\rho v^2} \quad (28)$$

$$N_{reK} = \frac{\rho v\sqrt{K}}{\mu} \quad (29)$$

The updated model provided a much more accurate representation of the test data, as illustrated by Figure 4.5. This model could then be used to estimate the pressure drop and power loss associated with the full scale regenerator.

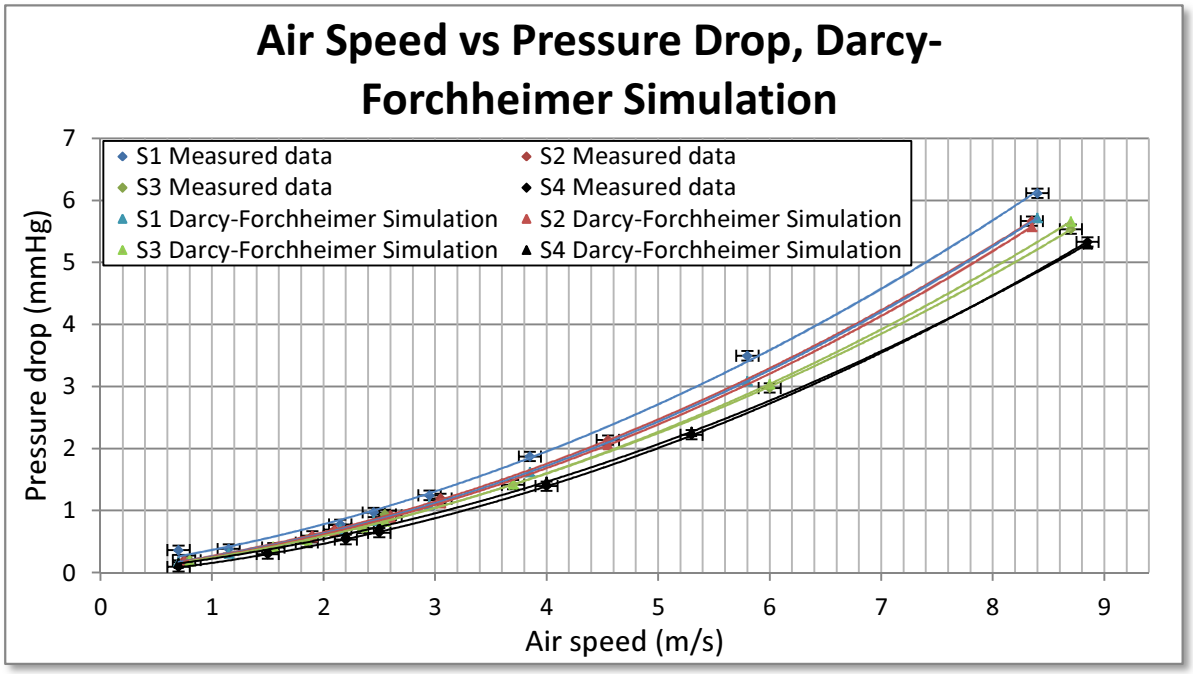

Figure 4.5: Measured data overlaid with Darcy-Forchheimer simulation data

4.1.1 Results

The validated theoretical pressure-drop model could now be utilised as a design tool to study variations in the regenerator design. If all sections were of the same width and packed with the same density of wire wool, the pressure drops and flow losses were calculated to be much higher through the outside segments. Figure 4.6 shows the calculated pressure drops through the regenerator split into four even sections, each packed with wire wool to the same density. The discontinuities represent the position of the partitions.

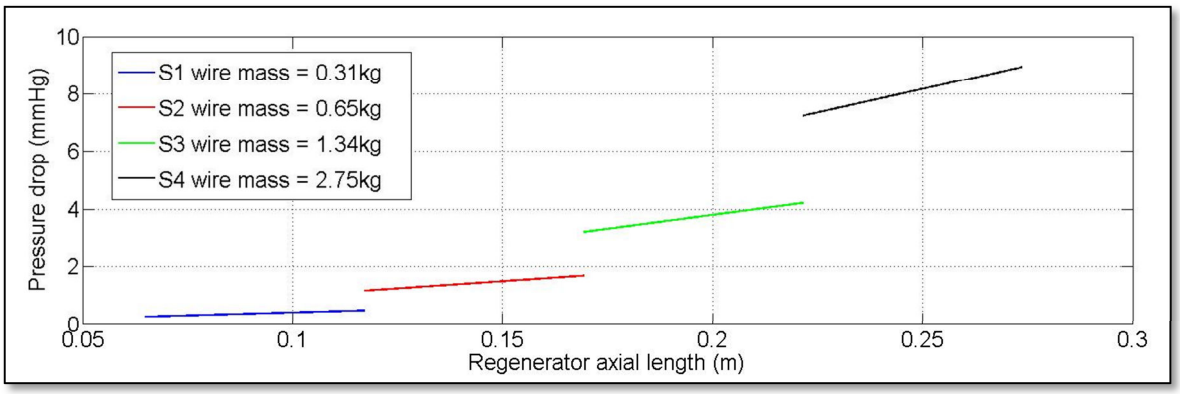

Figure 4.6: Regenerator flow losses with even spacing and porosity

The greater length of the outer sections increased flow friction and therefore pressure drop and power loss. This simulation assumed that the mass of air flowing through each section was even, however because of the lower flow friction there would be a higher flow rate through the inside. To achieve an even average pressure drop throughout each section of the regenerator, a Matlab function was written that allowed alteration of the wire mass of each section individually. The result is shown in Figure 4.7. While this equalised the average pressure drop, the **span** of the pressure drop on the inside section was much greater than that of the outside section. This pressure span was due to the fact that there were greater axial length spans from edge to edge within the inside sections.

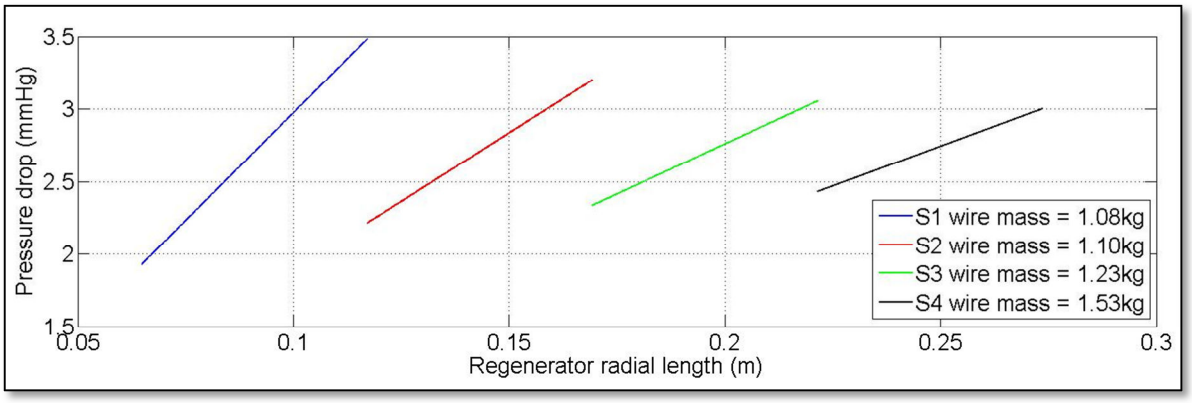

Figure 4.7: Equalised average pressure drop by manipulating wire mass

To equalise the pressure span across all sections another Matlab function was written to alter the segment widths. This resulted in an even pressure drop span throughout, as shown in Figure 4.8.

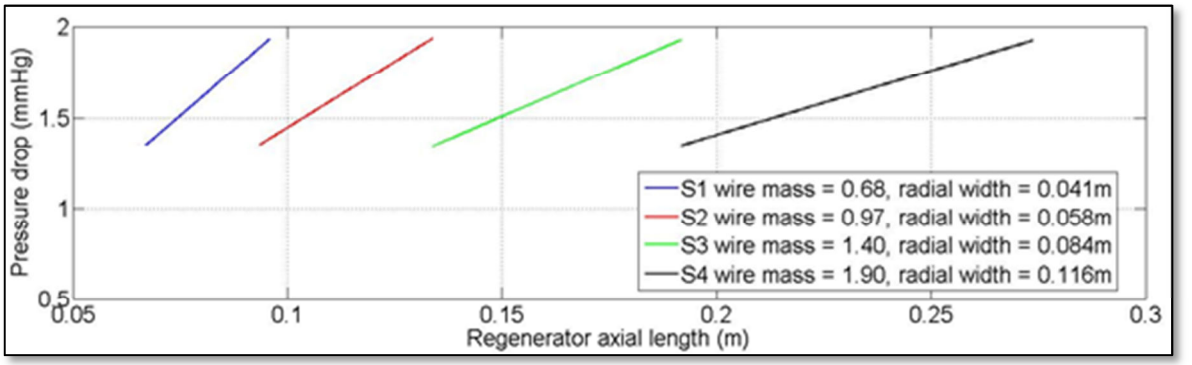

Figure 4.8: Equalised pressure drop span across segments all segments

With a total regenerator width defined by the internal dimension of the displacer chamber, the function illustrated in Figure 4.9 calculates the section widths, for any number of sections, required to give an even pressure drop throughout the regenerator. Using this data a decision had to be made as to how many sections were required to achieve an effective equalisation of the pressure drop, and therefore flow rate. The more sections that were added, the more even the flow rate would become, however adding curved panels also had the potential to negatively affect the regenerator performance in two ways. The junction between the wire wool and the curved panels had the potential to create an irregular fill structure causing unpredictable fluid flow. Also the volume occupied by the curved panels would not be doing any useful work.

Because it is very difficult to model the effects of these losses on the regenerator efficiency, it was decided to use the minimum number of curved panels to achieve an acceptably even fluid flow rate. To try and evaluate what the minimum number of sections would be, a function was written to cycle through from 1 to 9 sections calculating the maximum pressure drop **span** for each. The total wire mass for each case was kept constant, with only the distribution altered to level the average pressure drops. Figure 4.9 shows the results of this simulation, with maximum pressure drop span in mmHg plotted against the number of segments that the regenerator was split into.

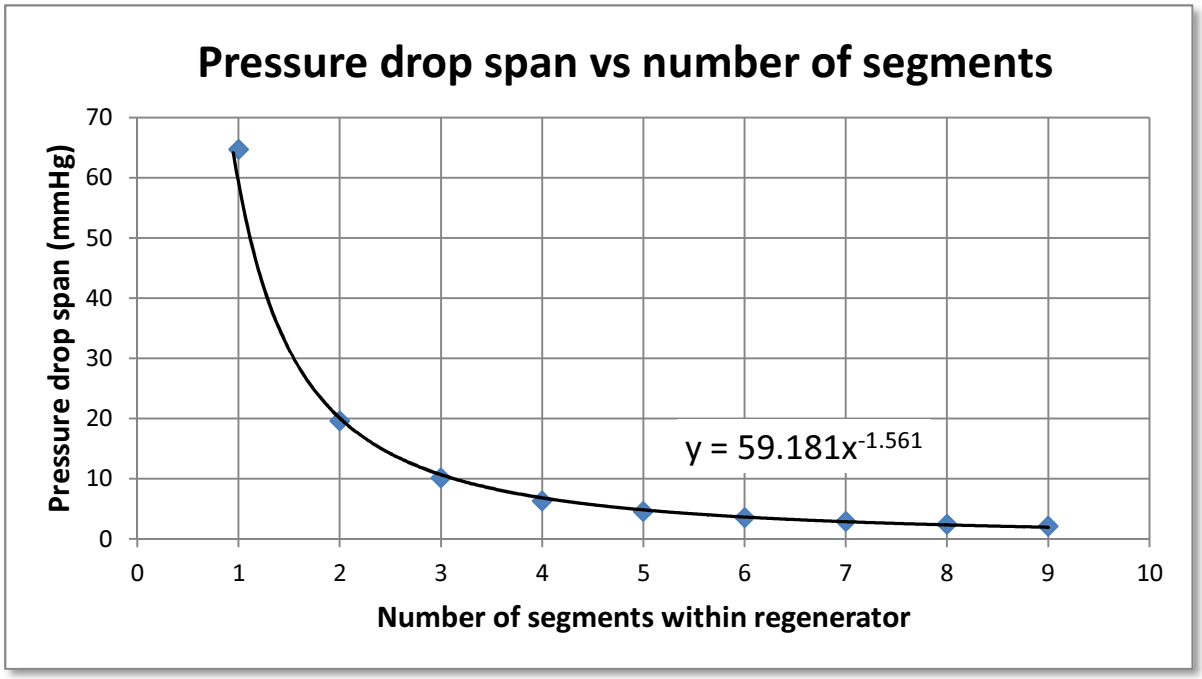

Figure 4.9: Rate of diminishing return with increased segments within regenerator case

The simulation indicated an initial steep drop off in pressure drop span, with diminishing returns for added segments. A trend line was added to the data showing a power relationship as illustrated by the equation in Figure 4.9. Based on the results of this simulation it was decided to use three internal curved panels creating four sections. This seemed like the best compromise between improved pressure drop span without adding too many sections. Figure 4.10 is a SolidWorks model of the final regenerator design, the curved panels are axial and placed at radii of 93, 134, 192, 276, 392mm.

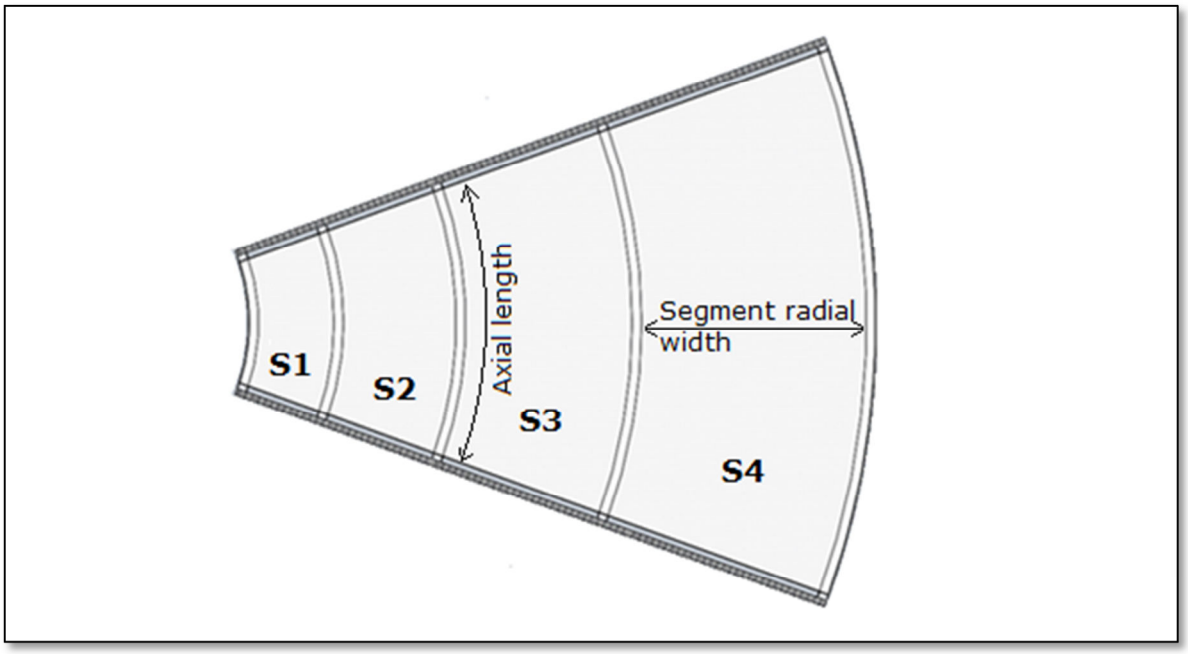

Figure 4.10: Segmented regenerator plan with four segments S1 (inside) to S4 (outside)

To evaluate the optimum mass of wire wool to be used, a Matlab function was written to evaluate the total power loss and effectiveness of the regenerator while varying the total wire mass used. The total power loss was simply the combined power loss of the four individual sections. Using the pressure drop calculated earlier the power required to push the working fluid through the regenerator segments could be calculated using equation 30 [14].

$$P_{loss} = 2fP_{drop}V_e \tag{30}$$

The regenerator effectiveness is defined as, the enthalpy change of the working fluid for a single blow, devided by the maximum theretical entalpy change for ideal regeneration [50]. To evaluate the effectiveness of each section, equation 31 was used [14]. The Number transfer units (NTU) was calculated using equation 32 [14].

$$\eta_{reg} = 100\left[\frac{\mathrm{NTU}}{\mathrm{NTU}+2}\right] \tag{31}$$

$$\mathrm{NTU} = \frac{\mathrm{h}S_{reg}}{\mathrm{M}C_p} \tag{32}$$

The optimal configuration would maximise the engine efficiency. As such calculations were made to estimate the overall effect of the fluid flow losses and regenerator effectiveness on total engine efficiency. The ideal engine efficiency is the net output work (W_{net}) divided by the total heat input (q_{in}) [14]. To acount for the imperfect regenerator and power loss due to flow losses the q_{loss} term was added to the denomenator in equation 33 [14]. This represents the extra heat energy that would need to be supplied to offset a regenerator effectiveness of less than $100\,\%$ and any regenerator power losses.

$$\eta = \frac{W_{net}}{q_{in} + q_{loss}} = \frac{nR(T_H - T_C)\ln\left(\frac{V_{max}}{V_{min}}\right)}{nRT_H \ln\left(\frac{V_{max}}{V_{min}}\right) + \left[\left((1 - \eta_{reg})mC_v(T_H - T_c)\right) + (P_{loss} * f)\right]} \quad (33)$$

Using the optimal operating temperatures of $T_H = 90\,°C$, $T_C = 25\,°C$ and asuming an operating frequency of $2\,Hz$ the engine efficiency was calculated for varying total regenerator wire mass.

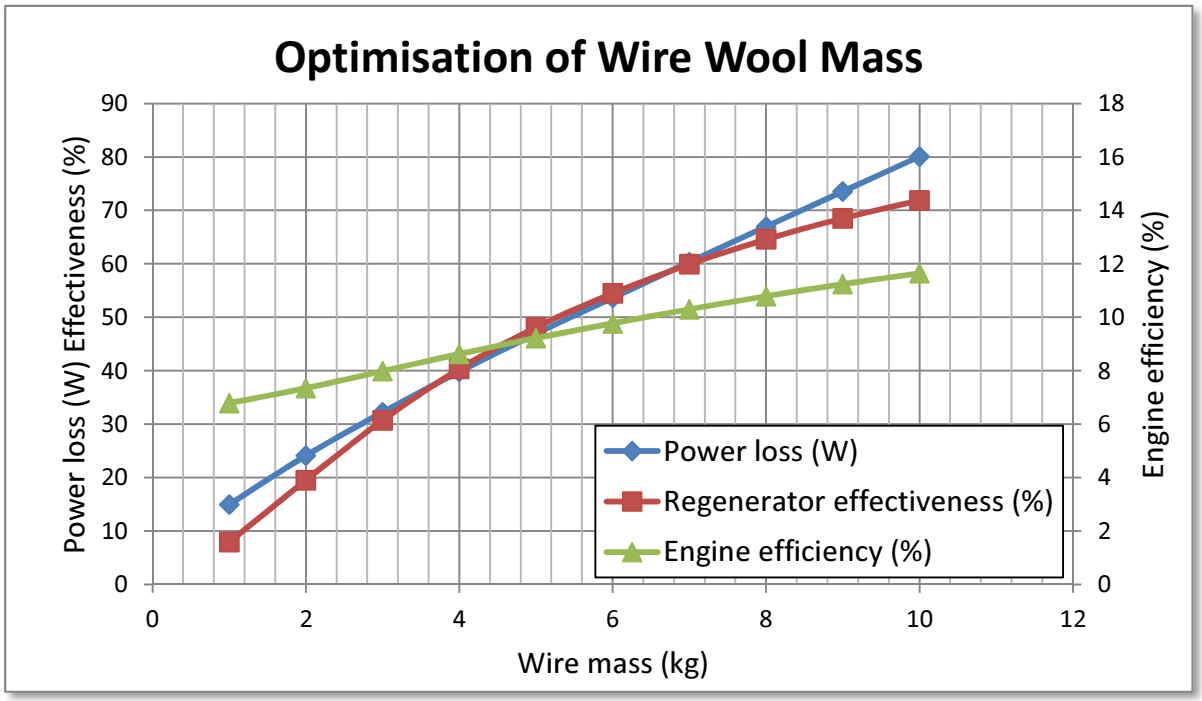

Figure 4.11: Wire mass optimisation

Figure 4.11 shows the simulated average effectiveness of the four combined regenerator segments (red) along with the combined power loss (blue). The net effect of these on the engine efficiency is shown in green; this is the parameter to be optimised. While this simulation in Figure 4.11 suggests that the optimum wire mass would be above 10kg it

also had to be considered that there would be a maximum weight of wire wool that could be packed into the regenerator volume. Tests were carried out to estimate the maximum density that could be achieved with samples of the wire wool to be used in the regenerator. The maximum achievable density when packing by hand was $256\ kg/m^3$ (determined by physical testing). With an internal volume of $0.00266\ m^3$, this limited the innermost section to a wire mass of $0.68\ kg$. After running a simulation to equalise the fluid flow this resulted in the full scale regenerator masses displayed in Table 4.5.

Table 4.5: Regenerator wire masses

Section	Volume (m^3)	Mass (kg)	Density (kg/m^3)
S1	0.00266	0.68	255.7
S2	0.00535	0.97	181.2
S3	0.01124	1.40	124.8
S4	0.02154	1.90	88.3
Total	0.04080	4.96	N/A

4.2 Regenerator Build

To stop direct heat conduction through the regenerator the curved panels were made of acrylic. Acrylic was chosen because it was stiff enough to hold its shape under the pressure of the compacted wire wool, and would not deform under the highest temperatures expected in the engine. The faces were constructed from a wire mesh; this confined the wire wool to the interior of the regenerator whilst still allowing the working fluid to pass through.

To create the curved acrylic sections, wooden forms were constructed using a thin piece of plywood bent over wooden ribs cut to the desired radius of the acrylic. The acrylic was heated in an oven to $150°C$ which is above its glass transition temperature of $120°C$. It was then removed and pressed onto the form until it had cooled. When the acrylic had cooled and solidified it was assembled into the final configuration. The joins were all glued with Weldon 16 fast set solvent cement and screwed with 15mm self-tapping zinc plated screws. Wire screens were then cut to size and screwed to each face. The final shell construction is shown in Figure 4.12.

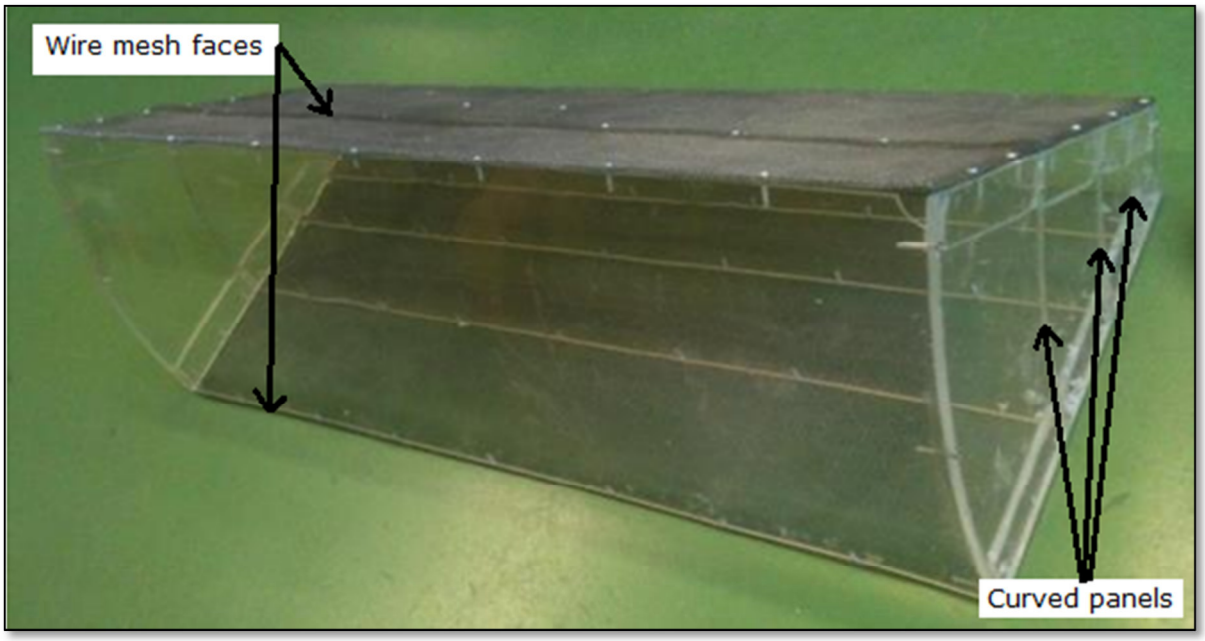

Figure 4.12: Final regenerator construction before packing

The wire wool was purchased in $5\,lb$ rolls. Each roll was cut into $800\,mm$ lengths, these lengths were then weighed and placed into the regenerator until the total weight for that section, seen in Table 4.5, had been reached. The top wire screen was then forced down and screwed to the acrylic frame. The regenerator was then placed inside the displacer chamber as seen in Figure 4.13.

Figure 4.13: Regenerator installed within displacer chamber next to one of the installed heat exchangers

4.3 DISCUSSION

The unusual shape of the regenerator in this engine means that its design was very experimental. A lot of time was spent designing and testing to try and overcome the shape peculiarities. To fully test the regenerator's performance a full scale test rig could be built; alternatively sensors could be placed inside the engine to assess its performance under real world operating conditions. One additional factor that was not tested and may particularly affect a regenerator of this design is fringe flow. This is where the wire wool is compressed against the acrylic and may create unwanted, lower resistance channels for the working fluid to pass through. With more working fluid passing through these channels and not through the wire, the efficiency of the regenerator would be affected. With the extra sections within this design there is a larger surface area of the wire wool acrylic boundary. If this does become an issue a rough surface could be glued to the acrylic reducing the chance of these channels being created.

Although it would also be possible to vary the wire diameter in different sections, it was decided for ease of construction and cost to keep the same diameter wire throughout. Introducing variable wire diameters would allow greater manipulation of the individual section's characteristics. A smaller diameter wire would increase the heat transfer area with decreased porosity, while a larger wire diameter would allow a greater thermal capacity with increased porosity. This option could be considered if the current design does not perform to the desired specifications.

The model developed to simulate the regenerator was only for steady flow and not oscillating flow. This was done for simplicity and also under the assumption that for a low speed engine, the pressure drop in the regenerator may be predicted adequately from the correlations developed for steady, unidirectional flow [51]. For higher accuracy an oscillating flow model could be developed. This may be necessary if the current design does not perform as expected.

5. MOTOR/GENERATOR SETUP

In order to generate electrical power from the mechanical action of the engine, a generator was required. A 1kW, 3 phase, permanent magnet generator had already been selected for this purpose [14]. As well as generating power when the engine is running, the generator must also initially run as a motor to get the engine started. This is because single piston, gamma type Stirling engines cannot self-start. This section covers the design and construction of a system capable of achieving this functionality.

5.1 DESIGN

Figure 5.1 is a block diagram of the final test setup. The motor/generator is controlled with the use of a computer via a field oriented control (FOC) inverter. The inverter allows control of bi-directional flow of three phase power to and from the motor generator. The inverter is powered with an isolated DC supply via a load switch circuit. This load switch circuit provides the capability of supplying a load to the motor/generator when it is in generating mode. The Stirling motor simulator was a three phase induction motor controlled with a variable speed drive (VSD) directly from the mains supply.

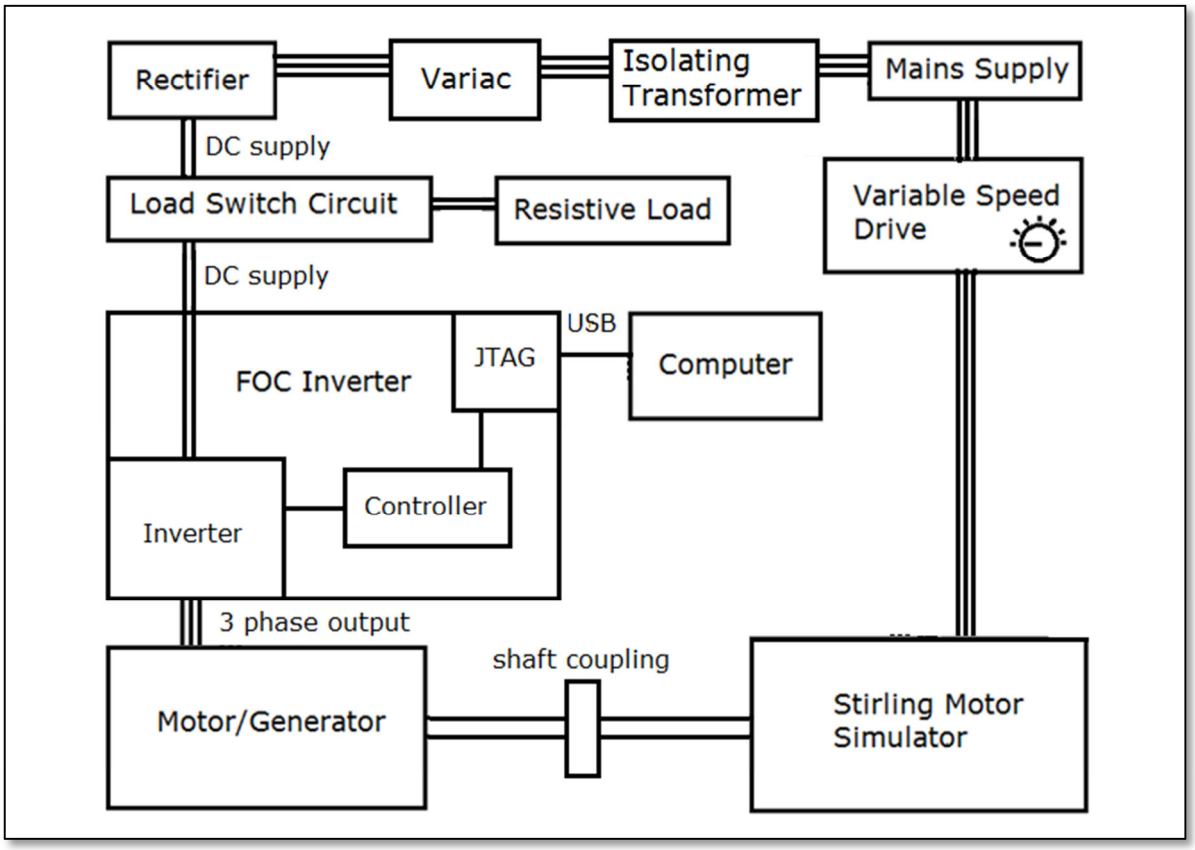

Figure 5.1: Block diagram of motor/generator setup

5.1.1 FOC INVERTER

Because the generator does not have any positional sensors, the best way to control it as a motor is a method called FOC. To achieve bi-directional flow of power, a pulse width modulation (PWM) controlled inverter was required. The TMDSHVMTRPCKIT permanent magnet synchronous motor (PMSM), FOC inverter from Texas Instruments (TI) was chosen to perform this task. This kit is designed to run high voltage permanent magnet motors without position sensors. It utilises a C2000 controller which can be programmed using TI's software editor and debugger, Code Composer Studio (CCS). A lot of the code needed to run a motor is provided with the kit and only requires customisation to a particular motor.

FOC estimates the motor's speed by measuring the phase currents of the motor while in operation. Figure 5.2 shows a block diagram of a typical FOC setup. Two of the three phase motor currents, designated by i_a and i_b, are measured and passed to the Clarke transform module. The $\alpha\beta\gamma$, or Clarke transform, can be thought of as projecting the

measured three phase motor currents onto a stationary two axis reference frame [52]. Only two measurements are required to complete the transformation because the three phase currents are assumed to be balanced, the third is always zero. The dqo, or Park transform, is then used to convert these measurements onto a rotating two axis reference frame called the direct and quadrature axis. These transformations effectively translate the three phase AC values into two DC values which are much easier to use in control calculations [53]. These direct and quadrature current measurements are then used as inputs for proportional-intergral (PI) controllers, adjusting the set points (i_{Sqref} and i_{Sdref}) to maintain the required speed (n_{ref}). The Park, or dqo, transform is then reversed to produce the PWM signals that control the inverter.

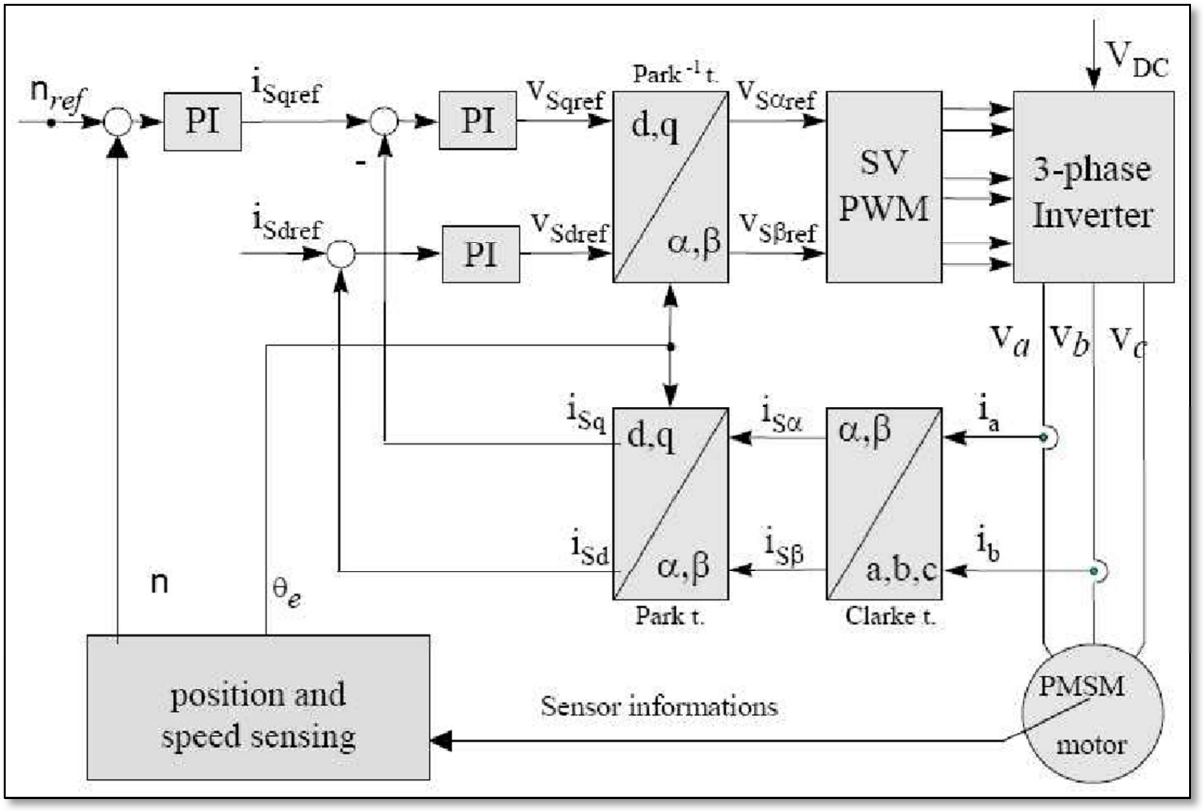

Figure 5.2: FOC for PMSM [54]

The motor/generator test setup is shown in Figure 5.3. The generator is on the left and the motor on the right is used to simulate the Stirling engine. The generator can be activated and speed or torque controlled using FOC with the use of TI's CCS. The motor on the right can then be activated using a VSD (in variable torque mode) to simulate the Stirling engine increasing its torque output. If at some point the Stirling engine torque

increases such that it is greater than the generator's, then the Stirling engine is running under its own power. At this point the current supplying the inverter would drop below zero and a resistive load must be switched in to dissipate the generated power.

Figure 5.3: Motor/generator test setup

5.1.2 Load Switch Circuit Design

The resistive load, shown in the middle of Figure 5.3, supplies an artificial load to the generator which dissipates the power being produced and also provides a measurement of the output power. To achieve the switching of the resistive load an additional circuit was required to be designed and built. The schematic of this circuit designed for this purpose is shown in Figure 5.4, and the printed circuit board (PCB) design is shown in Figure 5.5.

The purpose of this circuit is to sense when the Stirling engine begins to generate power and switch the motor/generator from its motor configuration, used to start the Stirling engine, to its generator configuration, used to produce power from the running Stirling

engine. A $4\,m\Omega$ current sense resistor (R7) was placed in the power supply ground line. The voltage drop across this resistor was monitored by an INA282 current sense amplifier with $200\,V/V$ amplification. A passive RC filter (R11 and C8) with a cut-off frequency of $31\,Hz$ was used on the output of this setup and then fed into a comparator. The other input of the comparator was connected to a variable voltage so that the trip point could be tuned if necessary. The comparator output then controlled a transistor (Q2) which switched a metal oxide semiconductor field effect transistor (MOSFET, Q1) capable of handling the power supplied by the generator. When the sensed current dropped below the reference voltage, the comparator switched on the MOSFET and thus the resistive load. The light emitting diode (LED, D2) provided a visual indication when this switching took place. A diode in the positive line prevented any large voltages being transmitted back through the power supply to the grid.

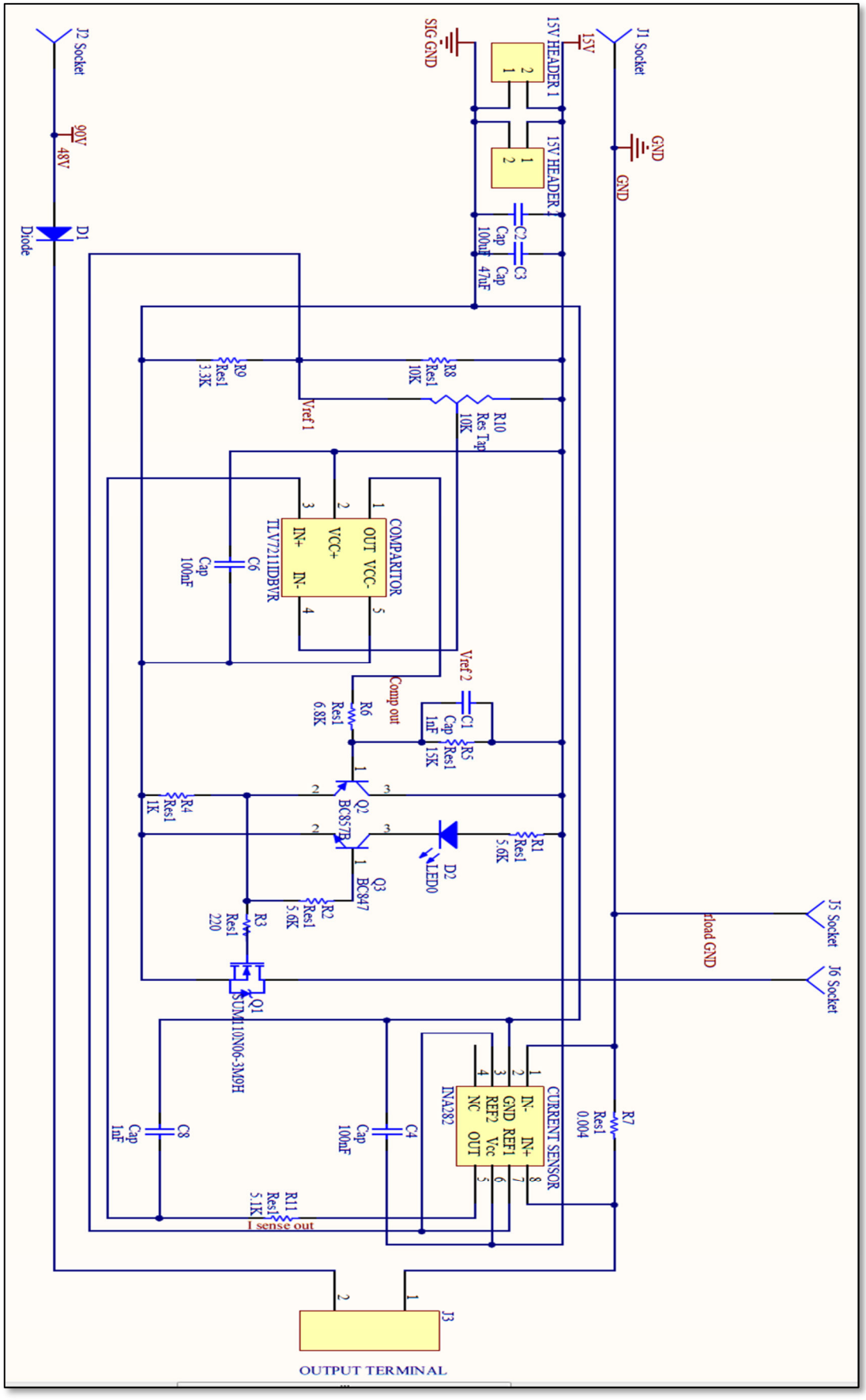

Figure 5.4: Switching circuit schematic diagram

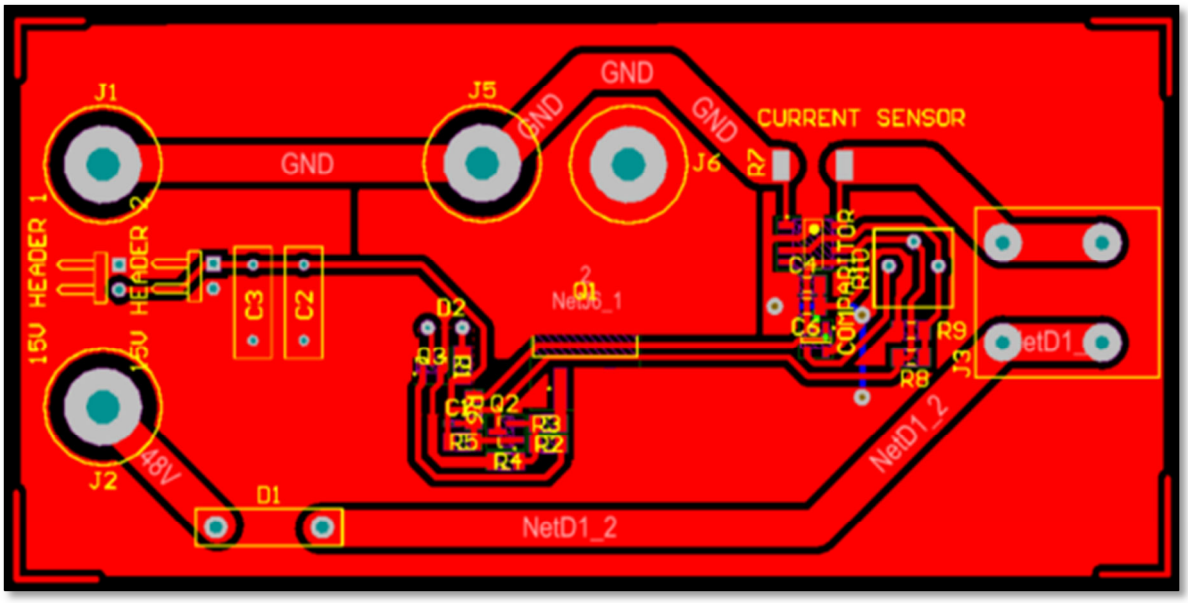

Figure 5.5: PCB design of load switching circuit

5.2 Setup and Testing

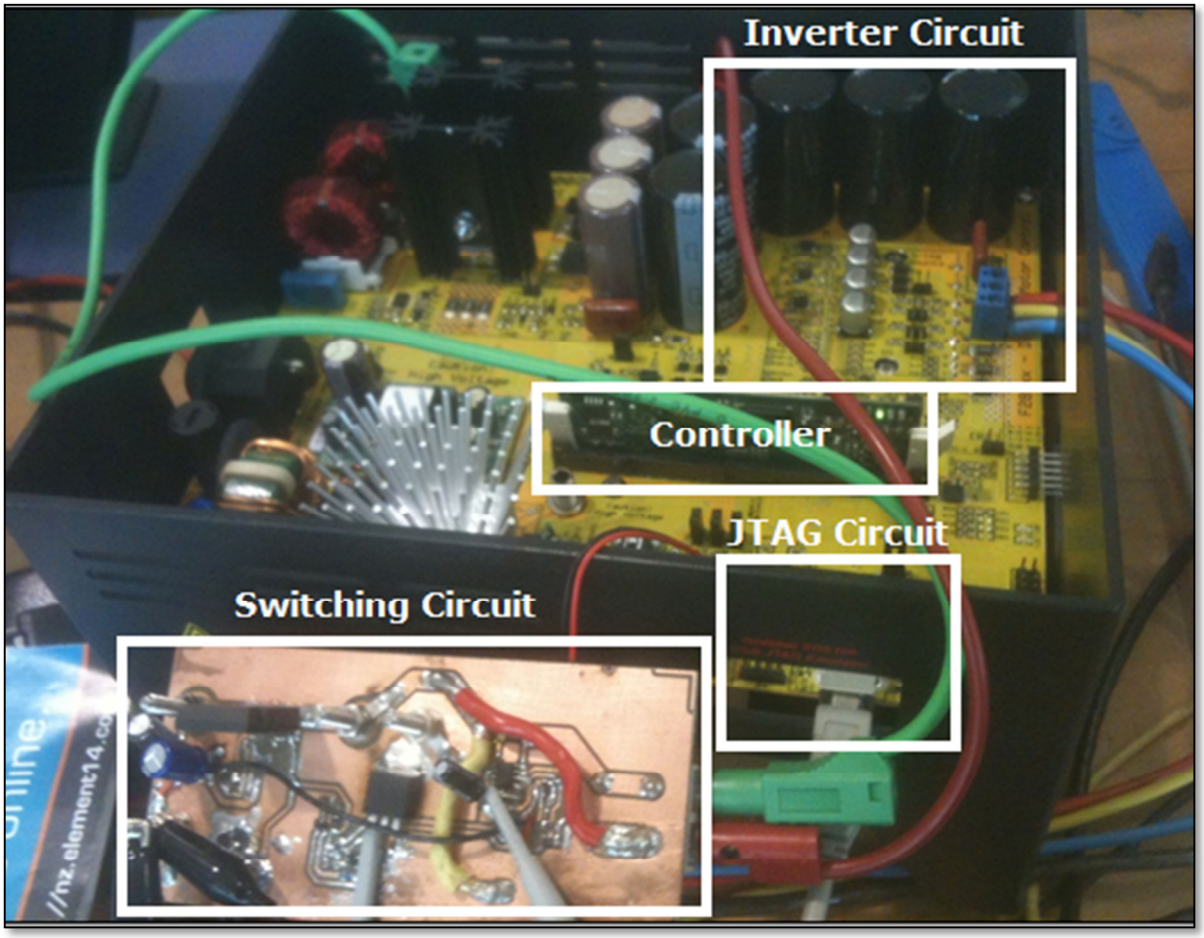

Figure 5.6: TI's TMDSHVMTRPCKIT PMSM FOC inverter connected to load switching circuit

Figure 5.6 shows the switching circuit connected between the power supply and the inverter. The three leads heading out of the inverter on the left hand side of Figure 5.3 go to the motor/generator. The inverter was connected to a laptop running TI's CCS. By controlling the inverter, the motor/generator was brought up to $480\,rpm$. The Stirling engine simulating motor torque was then slowly increased using the VSD. As the torque of the Stirling engine simulating motor increased, the current flowing from the power supply through the load switch circuit to the inverter decreased. This is illustrated by a measurement was taken from the output of the INA282 current sense amplifier represented by the purple trace in Figure 5.7. The red trace in Figure 5.7 is the control level voltage on the gate of the power MOSFET. As illustrated, when the inverter current drops below the reference current, shown in green, the control voltage switches from low to high as desired. The supply current response time is slower than load current measurement because of the low pass filter placed on the output of the INA282 current sense amplifier.

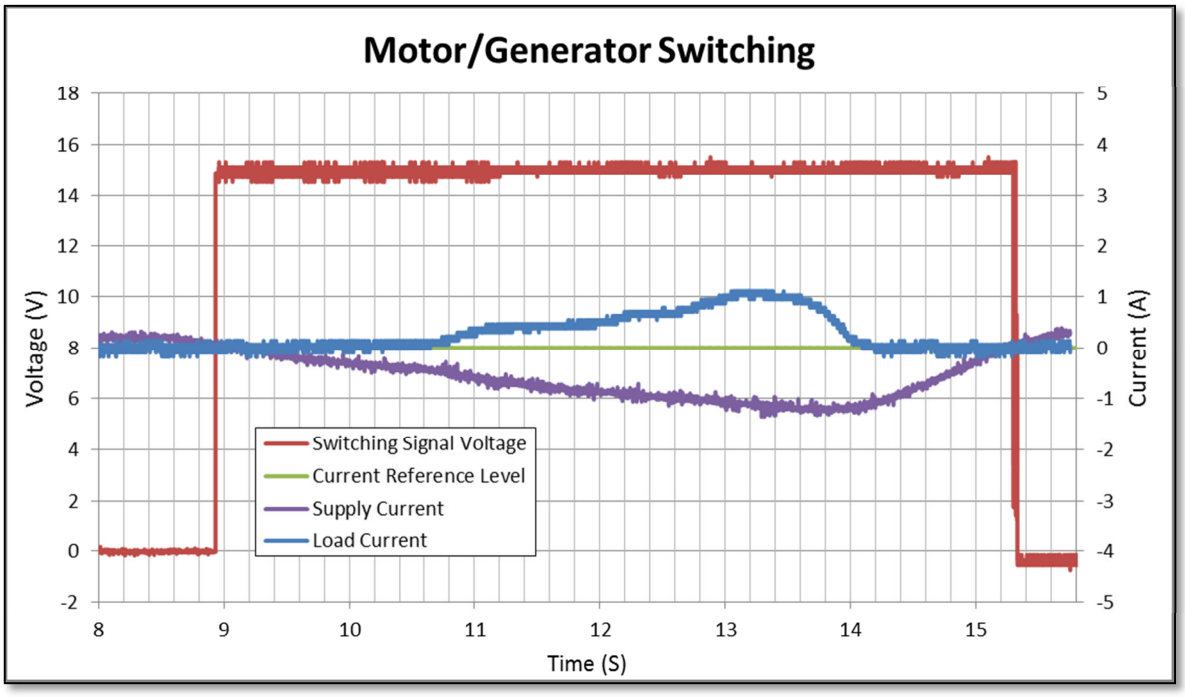

Figure 5.7: Illustrates the switching of the resistive load when the supply current drops below a reference point

Figure 5.8 shows the phase currents and voltages in both motoring and generating modes. The orange and red traces represent a single phase voltage in motoring and generating modes respectively. The green and blue traces represent a single phase current in motoring and generating modes respectively, with a resistive load of $25\,\Omega$ in generating

mode. The 180° phase shift in the current shows the change in the direction of power transfer.

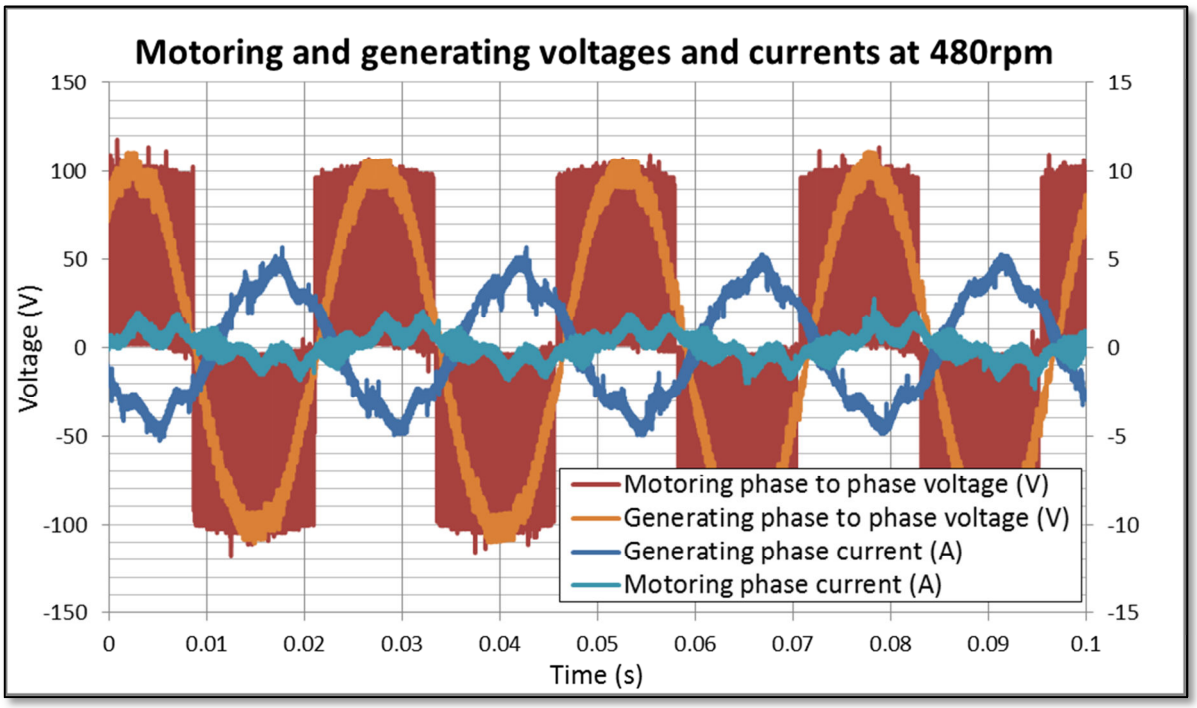

Figure 5.8: Motoring and generating voltages and currents when running at 480rpm with 25Ω load

5.3 Discussion

Initially the components in the switching circuit were chosen to handle the generator phase-neutral voltage rating of $48\,V$. After preliminary testing it was discovered that a higher dc supply voltage was required for the generator to reach the design speed of $480\,rpm$. In the final setup, with the generator wired in a delta configuration, a dc voltage of $105\,V$ was required to reach the desired speed, as seen in Figure 5.8. This meant that several components in the load switch circuit had to be replaced to ensure they were operating within their voltage specifications.

When the switch is activated the generator is dumping its output into a resistive load. During testing the largest resistive loads that could be found were variable resistors with a limit of 50V and 1.5A. With three of these in series, the maximum power that could be dissipated was 225W. When running with the Stirling engine the resistive load has to be capable of dissipating up to 500W for extended periods. To achieve this either more resistors or higher power resistors will be required.

When used in the final setup the switching circuit should be placed inside the protective cover of the inverter, as the voltages produced by the generator can exceed $250\ V_{pk-pk}$ depending on the resistive load used.

6. INSTRUMENTATION SETUP

To assess the performance of the engine once the construction has been completed, measurement systems were developed. Although pressure transducers were previously acquired in [14], the design and implementation of the associated circuitry was still required to provide accurate measurement systems. This chapter covers the circuit design, calibration and testing of these pressure transducer circuits. It also includes the testing and analysis of the previously acquired TC-08 temperature thermocouple data logger [14].

6.1 PRESSURE SENSOR DESIGN

Four pressure sensors were chosen to provide feedback on the operating pressure conditions of the engine. These included the 40PC150G1A $150\,psi$ gauge pressure sensor, 40PC001B1A $\pm 50\,mmHg$ gauge pressure sensor, MPXM2010GS $10\,kPa$ pressure sensor and the XPCL04DTC $\pm 4\,"H_2O$ differential pressure sensor.

Table 6.1: Sensor pressure ranges

Sensor	Pressure range	Pressure range in kPa
40PC150G1A	$0 - 150\,psi$	$1034.21\,kPa$
MPXM2010GS	$0 - 10\,kPa$	$10\,kPa$
40PC001B1A	$\pm 50\,mmHg$	$\pm 6.66\,kPa$
XPCL04DTC	$\pm 4\,"H_2O$	$\pm 0.997\,kPa$

Table 6.1 shows the four pressure sensors that will be used to track pressure fluctuations in the engine, along with their associated pressure ranges. Figure 6.1 is a board level Altium Designer schematic of how the sensors were wired. Power was provided to the sensor boards via a regulated power board to prevent fluctuations in sensor measurements. The sensor output voltages were then connected to a data logger, where the data could be converted from a voltage to a pressure measurement and stored for analysis.

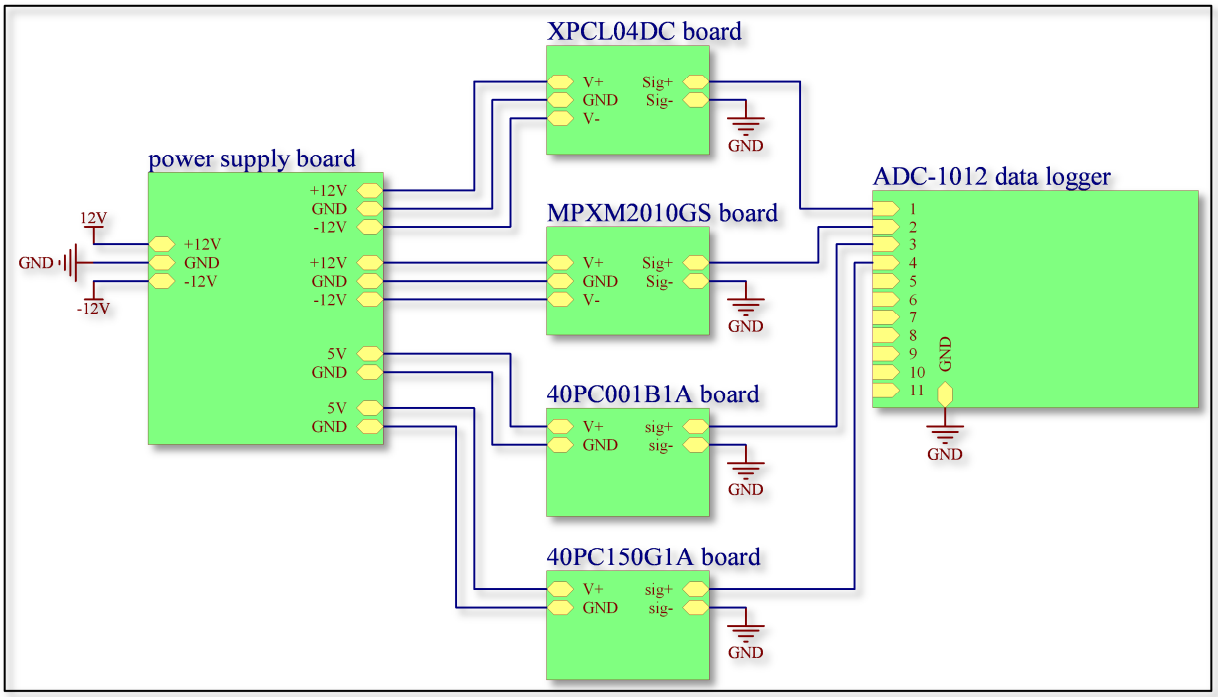

Figure 6.1: Board level schematic of pressure sensor setup

By recording both the pressure in the compression and expansion spaces and the angle of rotation of the engine, graphs similar to those shown in Figure 6.2 (a) and Figure 6.2 (b) can be obtained. Figure 6.2 (a) can be used to determine the difference in pressure between the compression and expansion spaces, which is due to flow losses in the heat exchangers (predominantly the regenerator) [55]. This information can be used to calculate the power loss associated with the flow losses in the heat exchangers. PV diagrams can also be constructed with this information, as seen in Figure 6.2 (b), from which the mechanical work produced by the engine can be calculated [55].

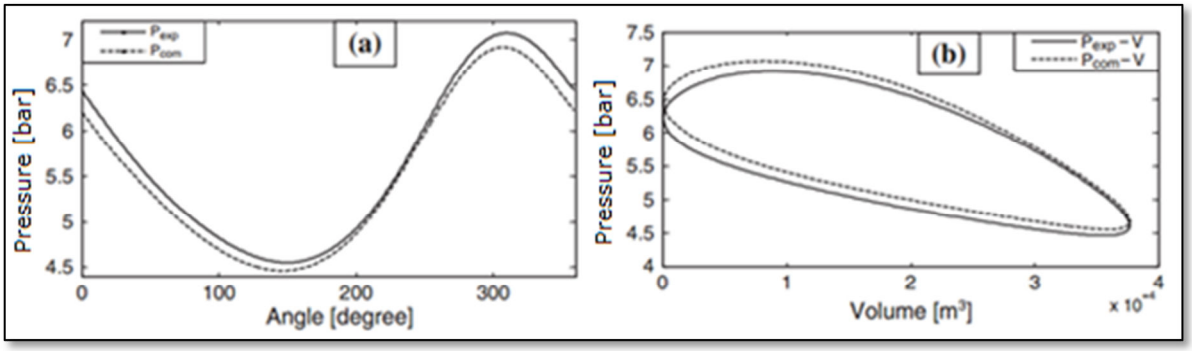

Figure 6.2: (a) Example of pressure vs angle of rotation, (b) Example of pressure vs volume [55]

To gather these measurements the transducer itself will be placed on one side of the pressure gradient, this will provide the reference pressure. A tube will then be attached to the transducer's input port, with the tube's open end terminating on the opposite side of the pressure gradient. For example, to measure the pressure variations in the expansion space the transducer will be placed in the buffer pressure space, above the displacer chamber. The tube will then be passed through the steel plate separating these two chambers and terminated within the expansion space, as shown in Figure 6.3.

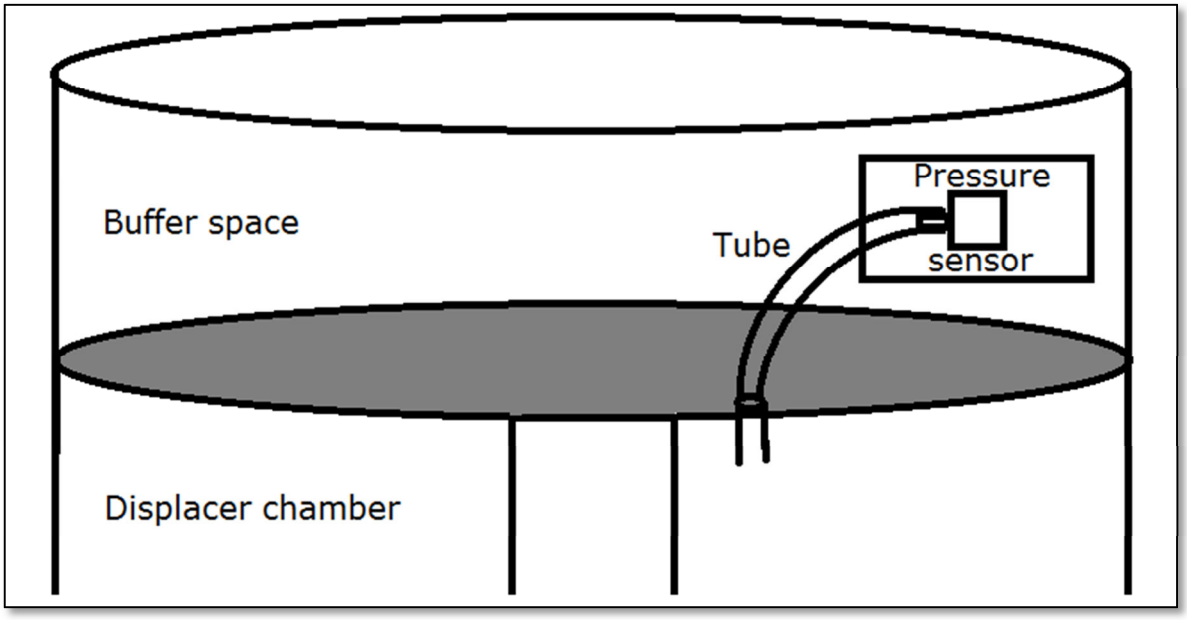

Figure 6.3: Example of pressure sensor placement for measuring pressure fluctuations within the expansion space

6.1.1 40PC001B1A Pressure Sensor

The 40PC001B1A is a piezoresistive pressure transducer that requires a supply voltage of $5\,V$ with an operating pressure of $\pm 50\,mmHg$. The output voltage ranges from $0.5\,V$ at $-50\,mmHg$ to $4.5\,V$ at $50\,mmHg$ with a response time of $1\,ms$. To scale the output voltage to the $2.5\,V$ limit for the ADC-1012, a resistor divider network was used. An input capacitor and passive low pass output filter with a cut-off frequency of $31\,Hz$ were also added for noise suppression, as seen in Figure 6.4.

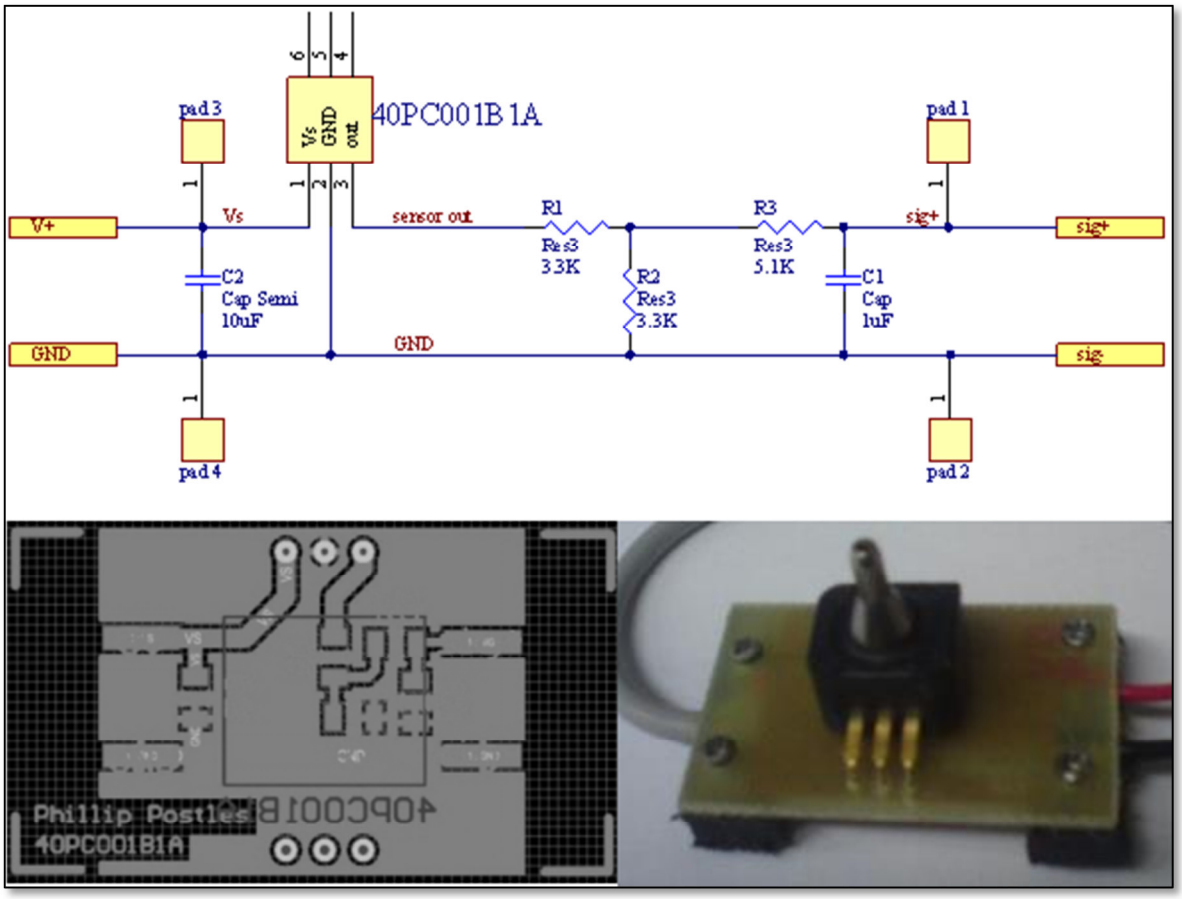

Figure 6.4: 40PC001B1A schematic, PCB and final implementation

6.1.2 40PC150G1A Pressure Sensor

The 40PC150G1A was intended to be used to measure the overall pressurisation of the engine and not the dynamic operating pressure changes. It was unable to be tested with a syringe as the pressures generated were not sufficient. It was decided that a more robust analogue gauge would be more suitable for the final engine.

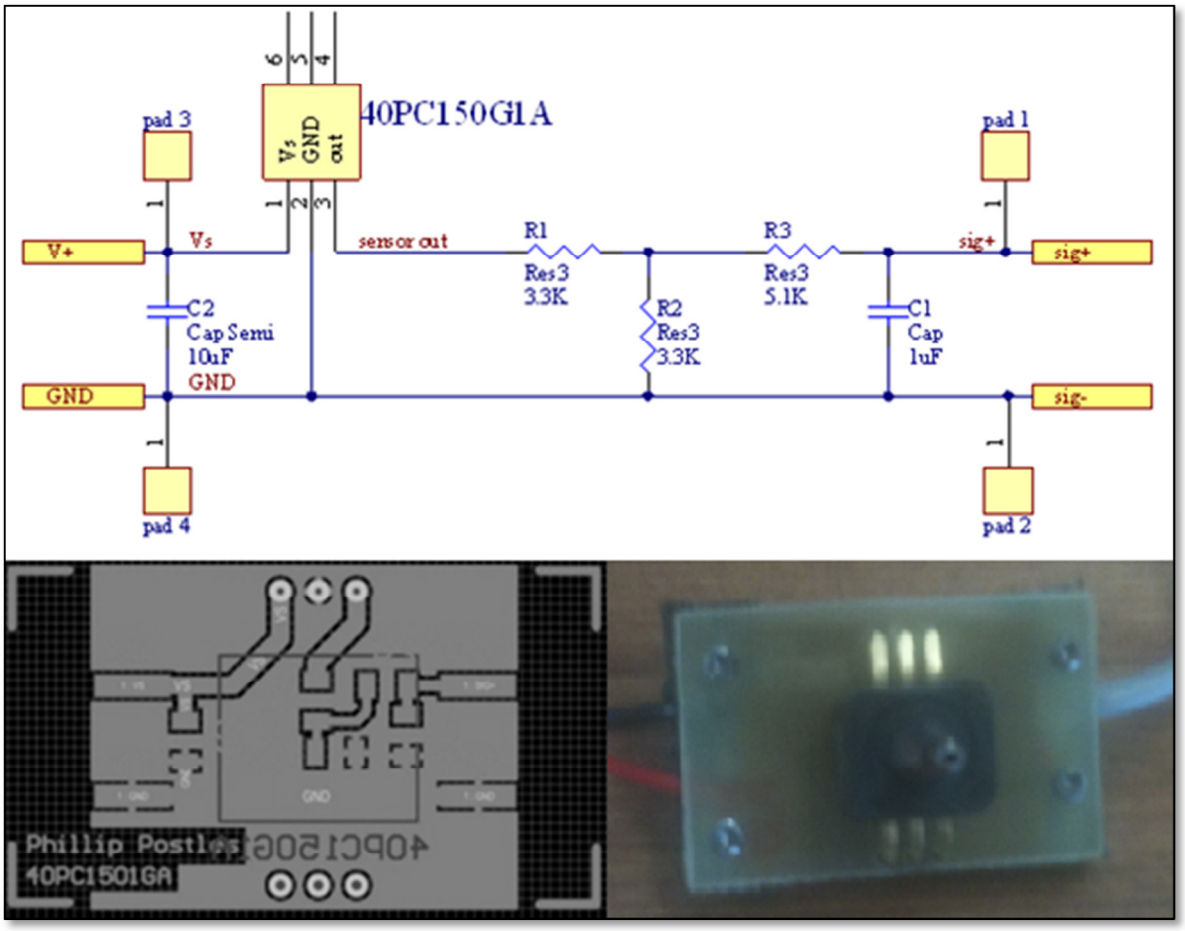

Figure 6.5: 40PC150G1A schematic, PCB and final implementation

6.1.3 MPXM2010GS Pressure Sensor

The MPXM2010GS is a silicon piezoresistive pressure sensor with a supply voltage of 10 to $16\,V$. It produces a differential ratiometric output voltage of $25\,mV$ from a differential pressure of 0 to $10\,kP_a$. To achieve the required output voltage an INA131 general purpose instrumentation amplifier was used, as shown in Figure 6.6. The INA131 has an internally set gain of 100, which increased the full scale output voltage to the required $2.5\,V$.

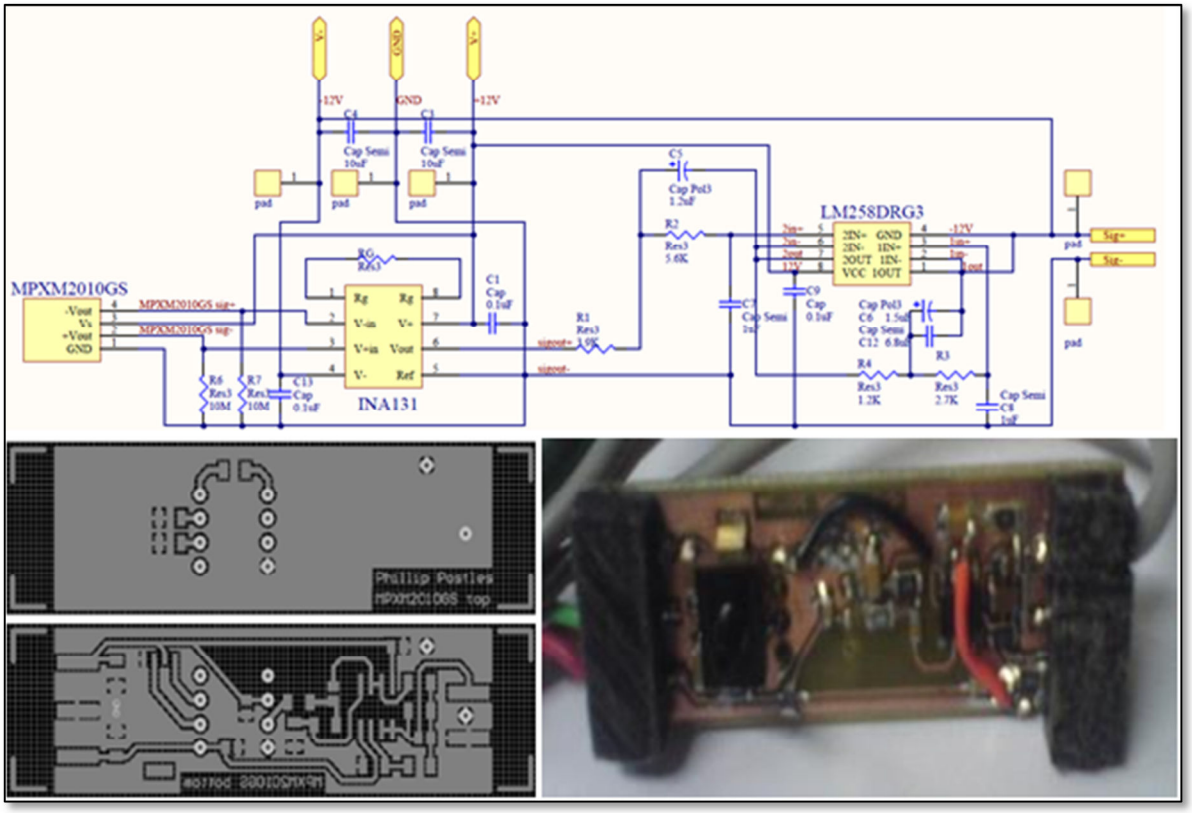

Figure 6.6: MPXM2010GS schematic, PCB and final implementation

TI's FilterPro tool was used to design a 2 stage, fourth order, Sallan-Key, active low pass output stage filter for noise suppression. The filter design and frequency response are shown in Figure 6.7. The filter was designed with a unity pass band gain, cut off frequency of $30\,Hz$, pass band ripple of less than $1\,dB$ and a stop band attenuation of $-25\,dB$ at $70\,Hz$.

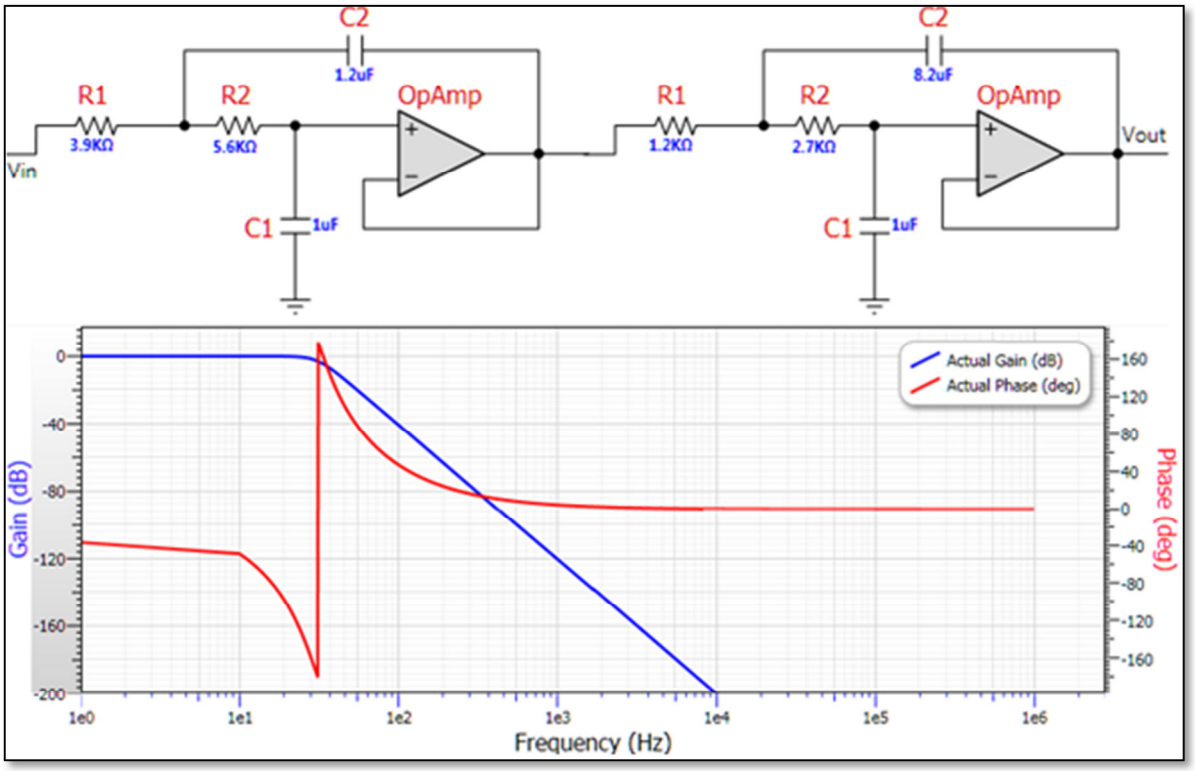

Figure 6.7: Unity gain 30Hz low pass output filter for noise suppression

6.1.4 XPCL04DTC Pressure Sensor

The XPCL04DTC is a precision compensated differential pressure transducer with an operating pressure of 0 to 4 inches of H_2O and a supply voltage of 0 to $16\,V$. The output voltage is ratiometric and has a full scale span of $0\,V$ to $25\,mV$, with a response time of $500\,\mu s$. The same amplifier and output filter stages were used as described earlier for the MPXM2010GS pressure transducer.

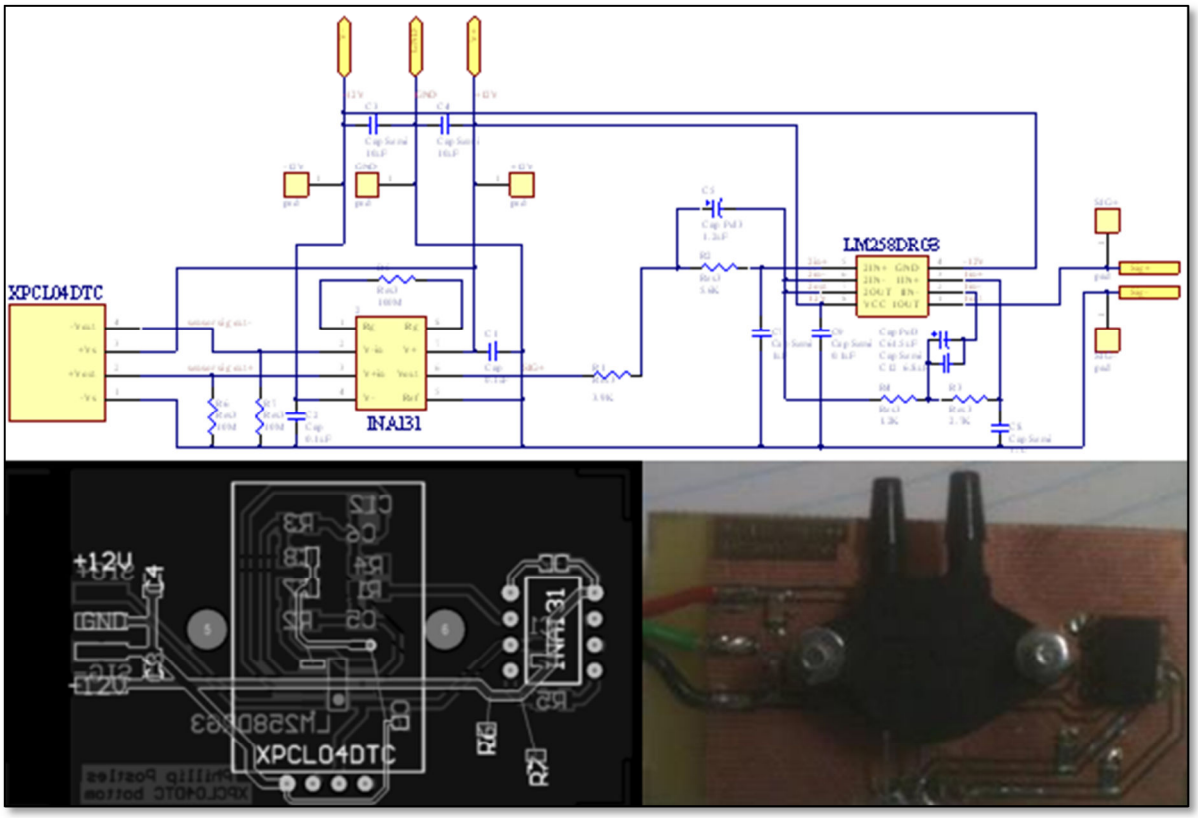

Figure 6.8: XPCL04DTC schematic, PCB and final implementation

6.2 Pressure Sensor Testing

To make sure that the sensors were ready to be used in the engine, testing was undertaken to assess their reliability and capabilities in terms of accuracy and response time.

6.2.1 Calibration

The pressure transducers were calibrated using a Perfect Aneroid analogue pressure gauge which measured from 20 to $300\,mmHg$ in $2\,mmHg$ increments. By connecting both the digital and analogue pressure gauges to a syringe the pressure was slowly increased in

$2\,mmHg$ increments (with an accuracy of $\pm 0.25\,mmHg$), while recording both the analogue pressure reading and transducer output voltage. A linear transformation could then be applied to the data in the PicoLog recorder software to adjust for any offset in the digital reading. This resulted in an accurate digital representation of the applied pressure that could be recorded with the Picolog software. Figure 6.9, Figure 6.10 and Figure 6.11 show the calibration data collected off the XPCL04DTC, MPXM2010GS and 40PC001B1A transducer circuits respectively. The x axis is the pressure read off the analog sensor and the y axis is the voltage measured at the output of the transducer circuits. All three sensors provided a linear output within their specified operating ranges.

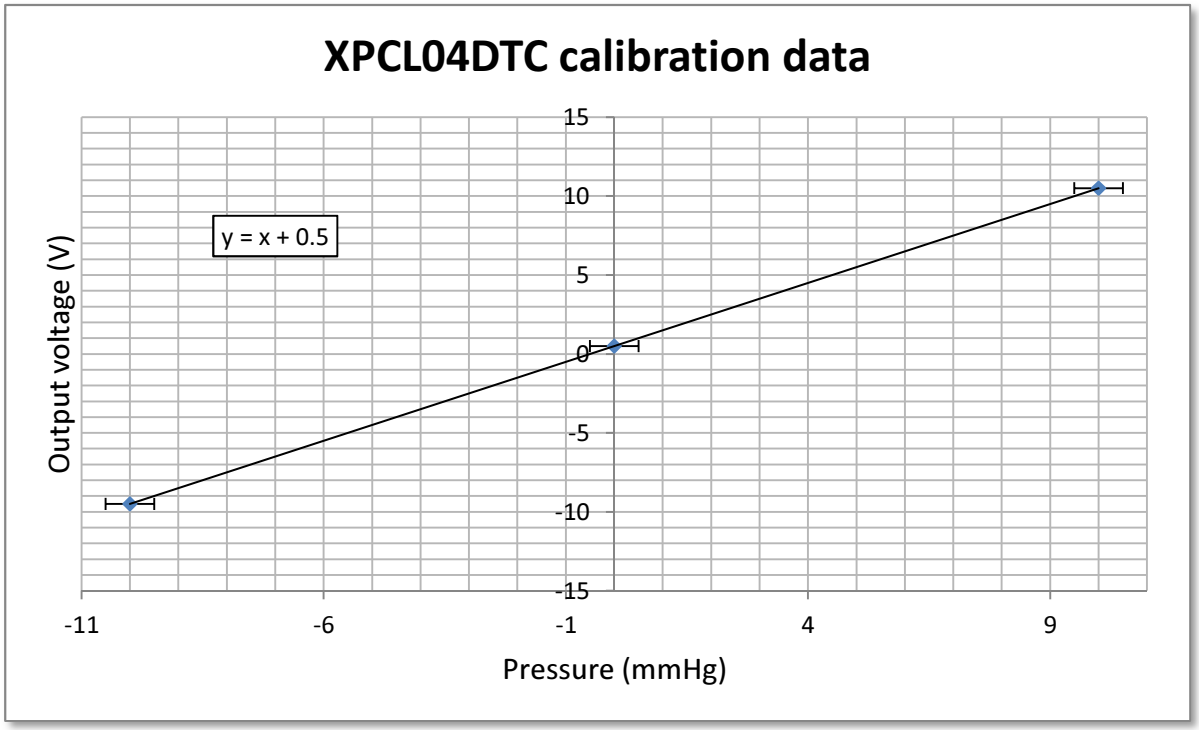

Figure 6.9: XPCL04DTC Calibration Data

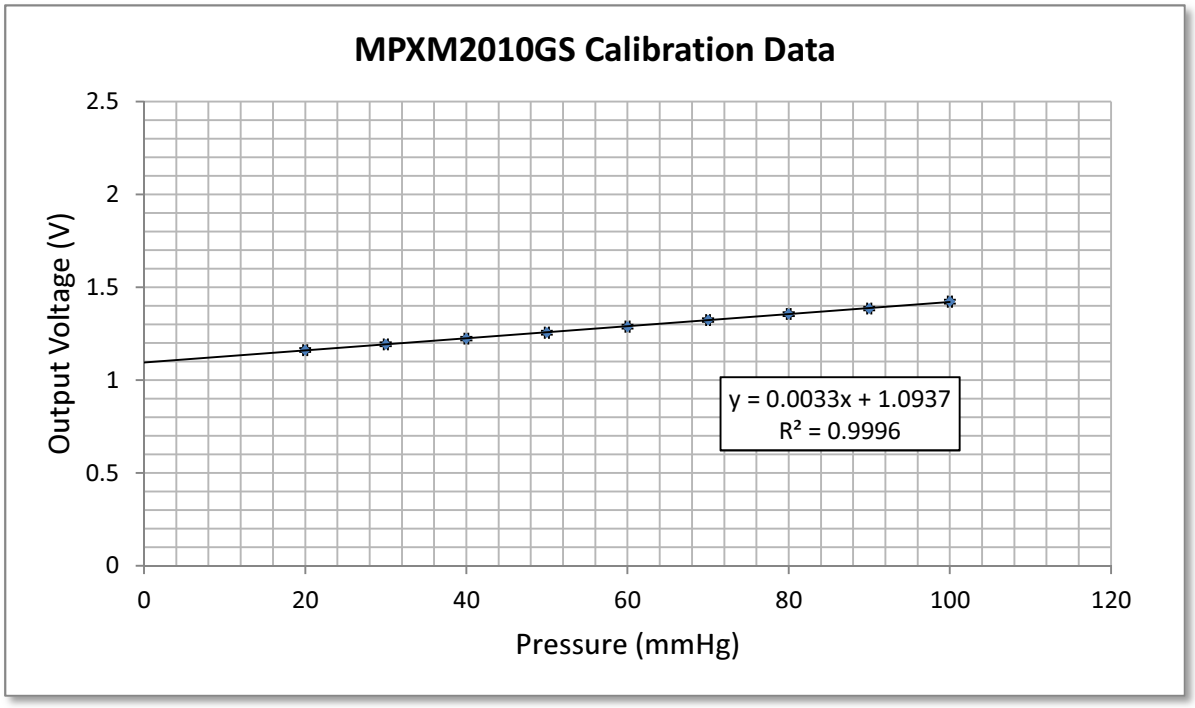

Figure 6.10: MPXM2010GS Calibration Data

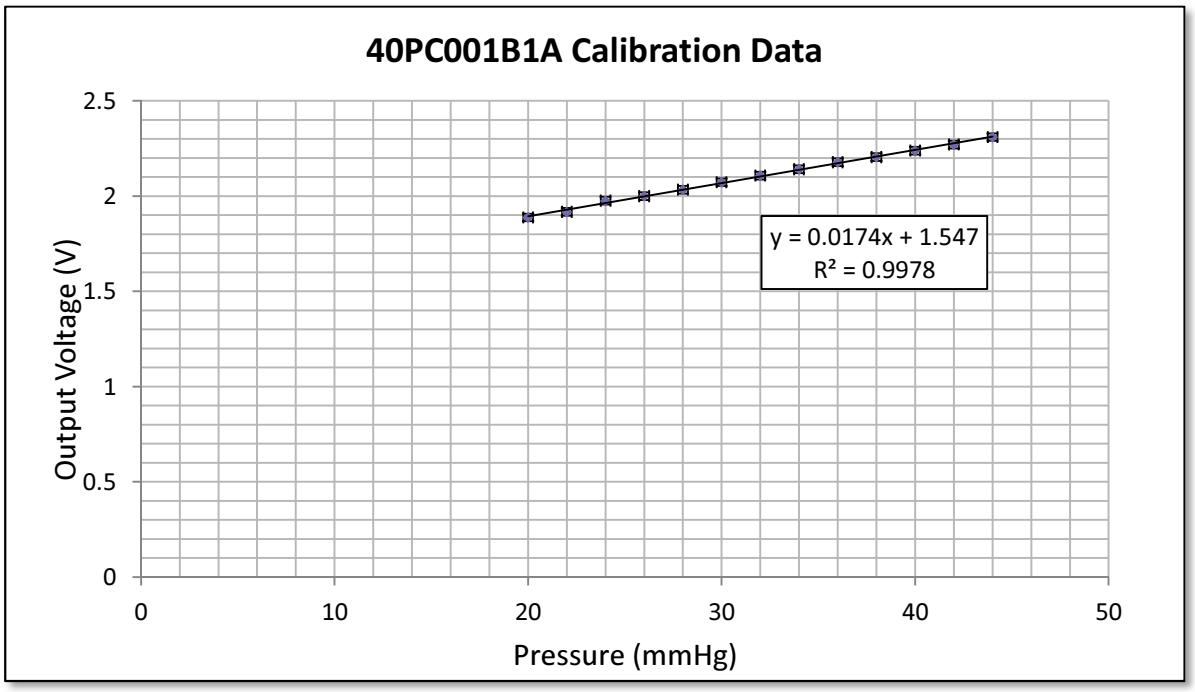

Figure 6.11: 40PC001B1A Calibration Data

6.2.2 Dynamic Response

The PiocLog1012 analog to digital converter （ADC） is capable of 12 bit precision at 1000 Samples per second from up to 10 channels. Using Pico Technology's Pico Scope software, the data in Figure 6.12, Figure 6.13 and Figure 6.14 were recorded whilst each

sensor was attached to an air filled syringe. To test the dynamic capabilities of the system the syringe was extended and retracted by hand to simulate the fluctuating pressure inside the engine. As the engine will be running at 2Hz each sensor was tested at or above this frequency. The plots in Figure 6.14, Figure 6.13 and Figure 6.14 show that these systems are capable of accurately tracking pressure fluctuations up to and above 2Hz.

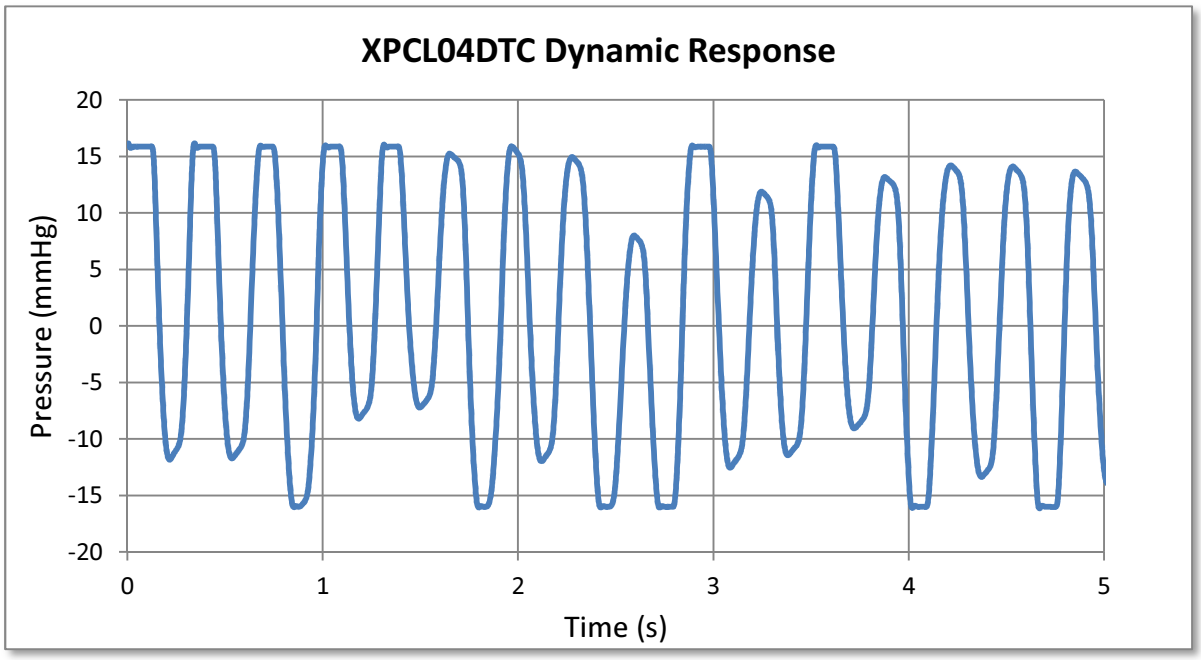

Figure 6.12: XPCL04DTC Dynamic Signal Response

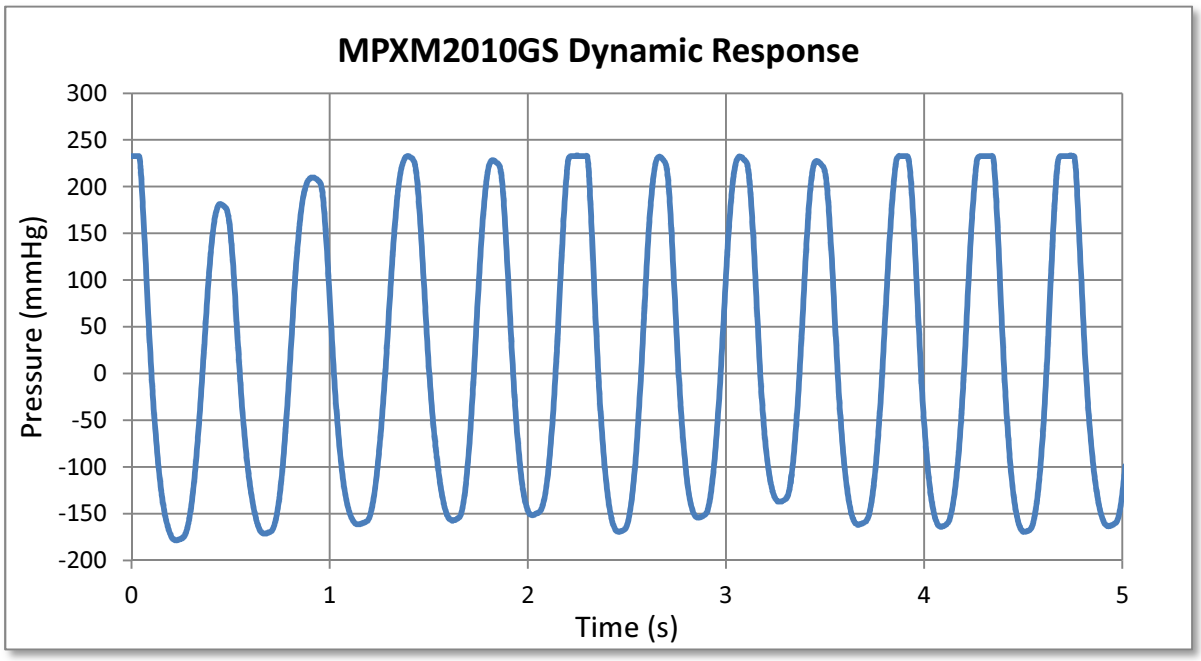

Figure 6.13: MPXM2010GS Dynamic Signal Response

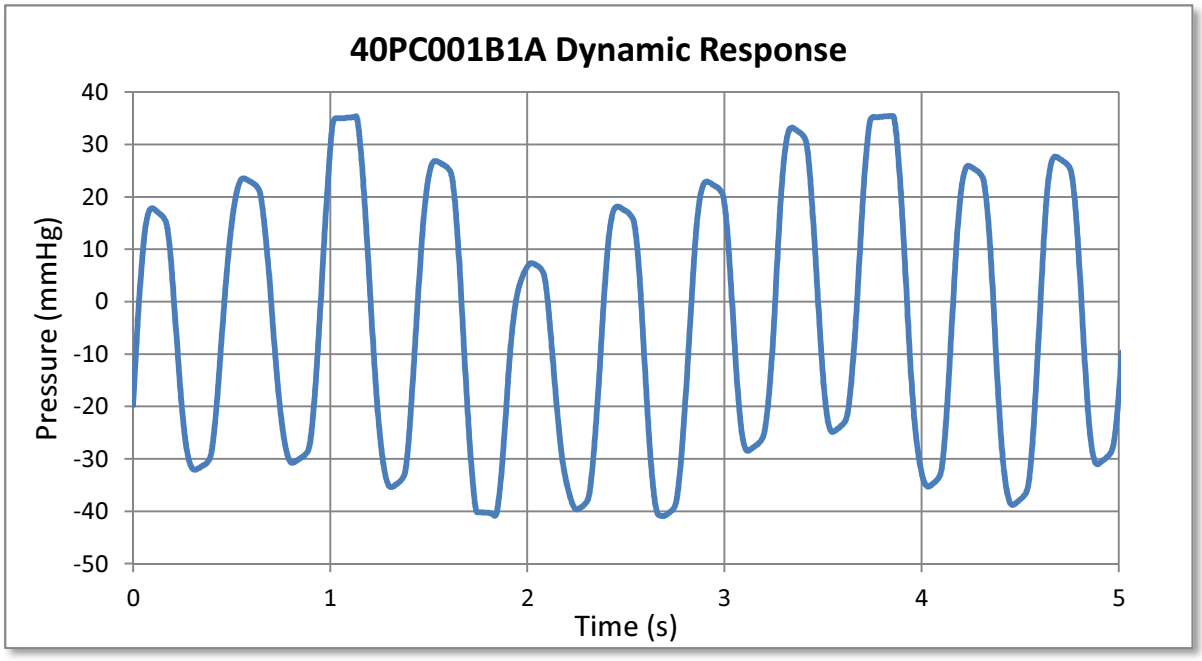

Figure 6.14: 40PC001B1A Dynamic Signal Response

6.3 TEMPERATURE SENSOR DESIGN

To measure the operating temperature of the engine, eight K type thermocouples were purchased. These were connected to a Pico Technologies TC-08 temperature thermocouple data logger, which in turn was connected to a laptop via USB. Pico-Log Recorder software was used to collect and store the data. These temperature sensors will be used to measure the temperatures of the heating and cooling fluid. If the temperature at the inlet and outlet of the heat exchangers are known, then the thermal energy transferred to the working fluid can be calculated, and subsequently the engine efficiency. They may also be used to measure the working fluid temperature in the compression and expansion spaces, or the temperature variation across the regenerator. These however would be average values as the sampling resolution of the data logger is greater than that of the designed engine period.

6.4 TEMPERATURE SENSOR TESTING

To test the accuracy of the Pico Technology TC-08 temperature thermocouple data logger, eight K-type thermocouples were connected and the unit was hooked up, via USB, to a computer running Pico Log Recorder software. The eight probes were held in the air in close proximity, but not touching. They were then placed into a glass of warm water with a temperature of $36.8\,°C \pm 0.4\,°C$. Figure 6.15 shows the transient response to this change in temperature giving an average $10-90$ response time of 1.8 seconds. Using the TC-08 with all eight probes, the maximum sampling rate is one sample per second, which somewhat limits the response time of the system.

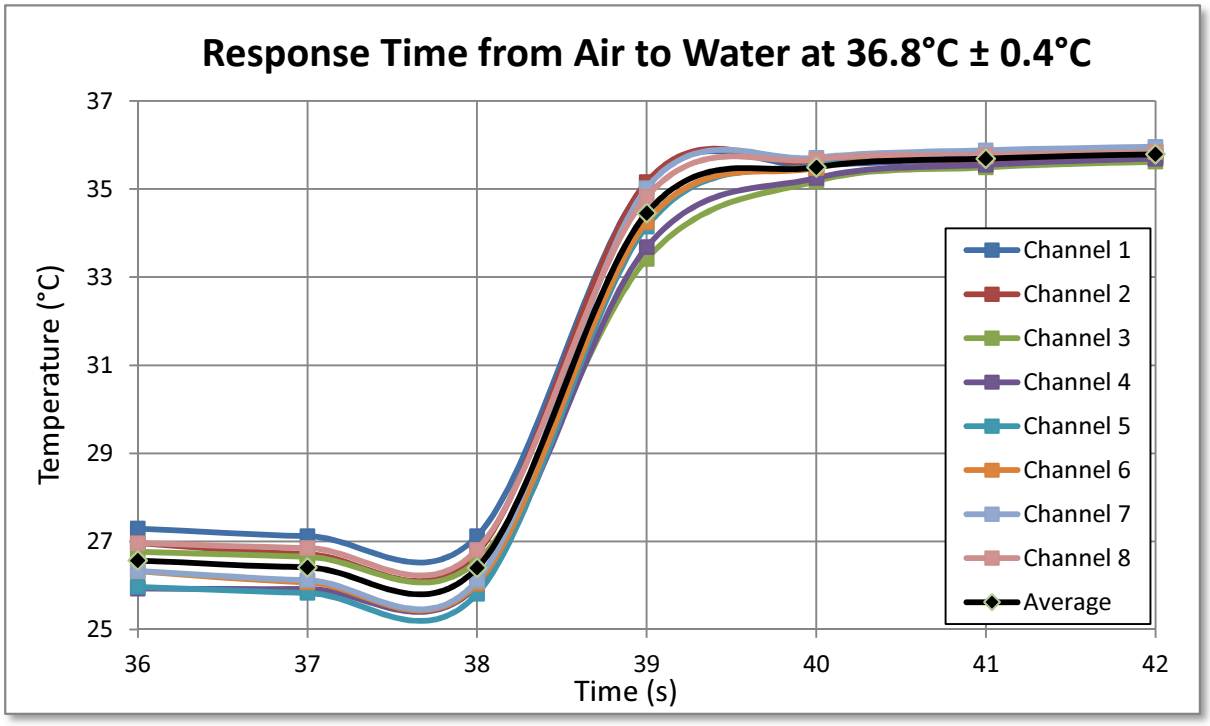

Figure 6.15: Temperature sensor transient response

The probes were then held in the water for one minute before a second 60 second sample was taken to ascertain the steady state accuracy. The standard margin of error for a K type thermocouple is whichever is greater of $\pm 0.75\%$ or $\pm 2.2°C$ [56]. In Figure 6.16 it can be seen that in this case there was a variance of about $0.5°C$ in the probe recordings, with a standard deviation of $0.16°C$.

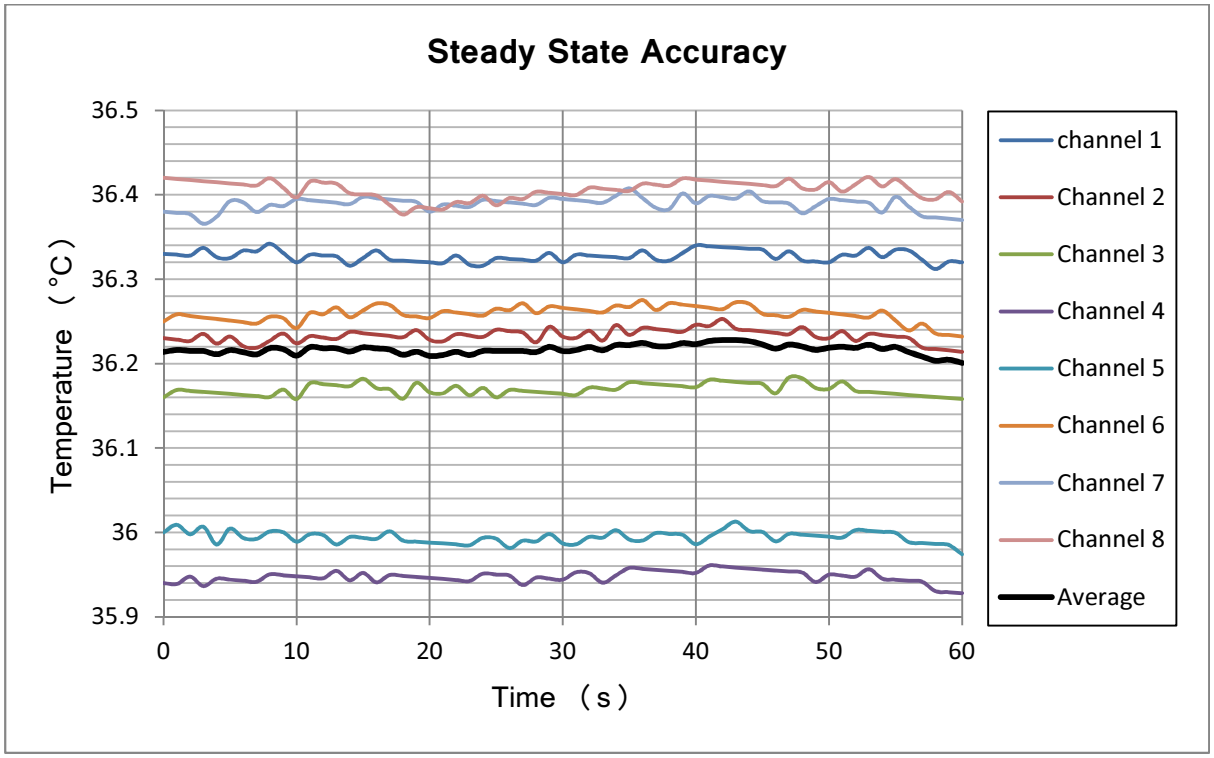

Figure 6.16: Steady State Accuracy of 8 thermocouple probes and TC-08 data logger

6.5 DISCUSSION

It was decided that the $150\,psi$ sensor would be replaced with an analogue pressure gauge, as the sensor is only required to measure the engine buffer pressure and an accurate measurement would not be required for analysing engine performance. This eliminated the need for one compression fitting, which is to be replaced with a cheap and simple threaded analogue pressure gauge.

One issue with the calibration of the XPCL04DTC pressure sensor was that the analogue pressure gauge, used to verify accuracy, only started at $20\,mmHg$ with increments thereafter of $2\,mmHg$. The XPCL04DTC's specified pressure range was only $\pm 10\,mmHg$. To overcome this limitation a linear interpolation of the needle position was used by marking on the analogue gauge half way between $0\,mmHg$ and $20\,mmHg$. This made it possible to get three points that were within the XPCL04DTC's operating range to calibrate with, resulting in a measurement accuracy of $\pm\,0.5mmHg$.

Using the TC-08 with all eight probes, the maximum sampling rate is one sample per second, which somewhat limits the response time of the system. This means that it is

only useful for measuring the inlet and outlet temperatures of the heating and cooling fluid or the average temperatures of the hot and cold side of the working fluid. For a more complete engine analysis it would be nice to have a faster response time, which would allow analysis of things like working fluid or regenerator temperature variations within a single cycle. The National Instruments NI9213E 16 channel thermocouple input module could be utilised in conjunction with LabVIEW to create a system capable of measurement accuracy down to $0.02\,°C$ at a sampling rate of $75\,S/s$.

7. CONSTRUCTION

This chapter describes all the general construction tasks that did not warrant their own chapter, as well as integration between various component sections. The phase angle control between the displacer and power piston is outlined. The research and acquisition of suitable compression fittings, required to pass signal and power wires through the pressurised cylinder walls is discussed. The design and manufacturing of heat exchanger end caps to reduce dead space is described. Finally general acquisition and construction tasks needed to complete the build are outlined.

7.1 PHASE ANGLE CONTROL

To provide closed loop control of the displacer element, detection of the rotational position of the crank shaft was necessary. This was achieved with the use of two Infrared (IR) OPTEK OPB775TZ reflective object sensors mounted perpendicular to the crank shaft, as shown in Figure 7.1. Reflective tape placed on the crank shaft provided a signal that the stepper motor controller could then use to time the movements of the displacer. The first sensor had two pieces of tape placed 180° apart which provided the activation signals to rotate the displacer. In order to distinguish which direction the displacer should rotate upon activation, a second sensor was utilised. This sensor was placed 90° out of phase and offset from the first sensor. As shown in Figure 7.1 this second signal was active during one of the activation signals and inactive during the other.

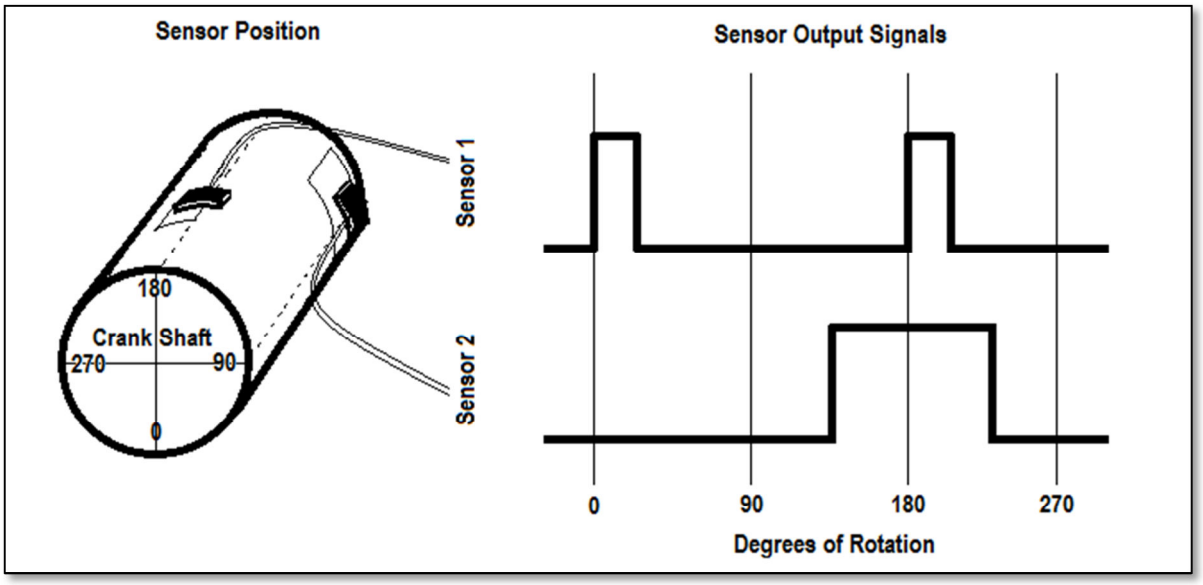

Figure 7.1: Shaft sensor position design

Figure 7.2 depicts the implementation of the IR sensors for testing. The sensors were mounted to the motor casing with aluminium brackets.

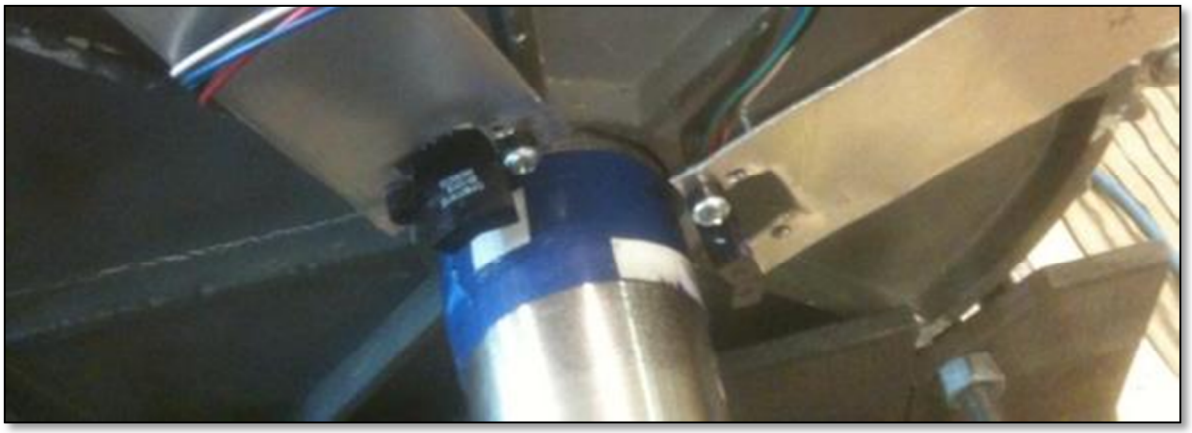

Figure 7.2: Implementation of IR sensors

Figure 7.3 shows the output signals generated from testing. The black trace is the activation signal which indicates when the displacer should rotate. The red trace represents the direction signal which determines the direction the displacer should rotate. The blue trace indicates the rotation of the stepper motors which control the displacer.

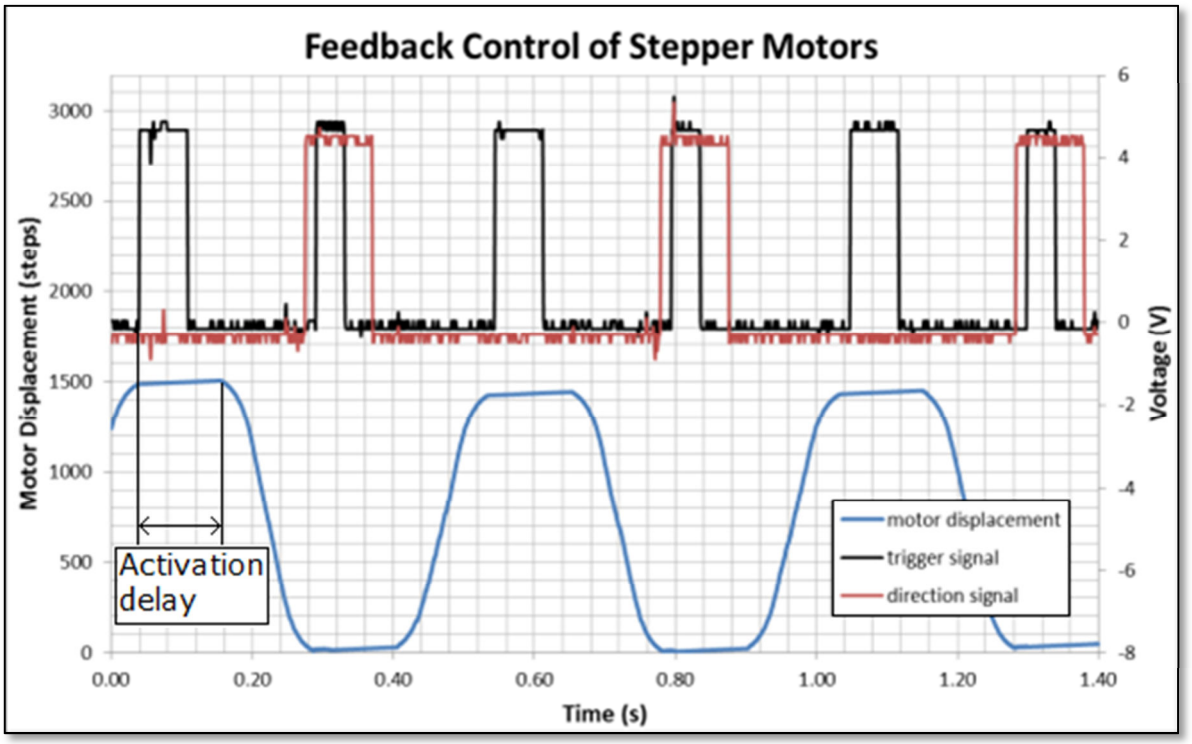

Figure 7.3: Feedback Control of Stepper Motor running at 2 Hz

There is an inherent delay between the detection of the activation signal and the movement of the stepper motors, as seen in

Figure 7.3. In the final implementation this can be adjusted for by manipulating the placement of the reflective tape. In general it is desired that the power piston should lead the displacer by 90° [57], however for optimisation it is advantageous to be able to adjust this phase delay between around 70° to 110°. Testing was undertaken to assess whether it would be possible to accurately manipulate the phase delay by initiating a delay in the control code between the detection of the activation signal and the activation of the stepper motors. To achieve this, a wait command was implemented in the motor control code between the detection of the trigger signal and the activation of the motors. Figure 7.4 shows the results of incrementing the wait command in the smallest steps possible while the shaft was rotating at $1.58\,Hz$. When running at $2\,Hz$ the longer wait times extended past the following activation signal, this resulted in some activation signals being missed. The specified delay time for the "wait" command was $10\,ms$. This was verified experimentally with each integer increasing the delay an average of $10.96\,ms$, which

resulted in an increased phase delay of 6.25°. If the time delay was consistent at $2\,Hz$ then this would constitute a minimum phase delay resolution of 7.89°

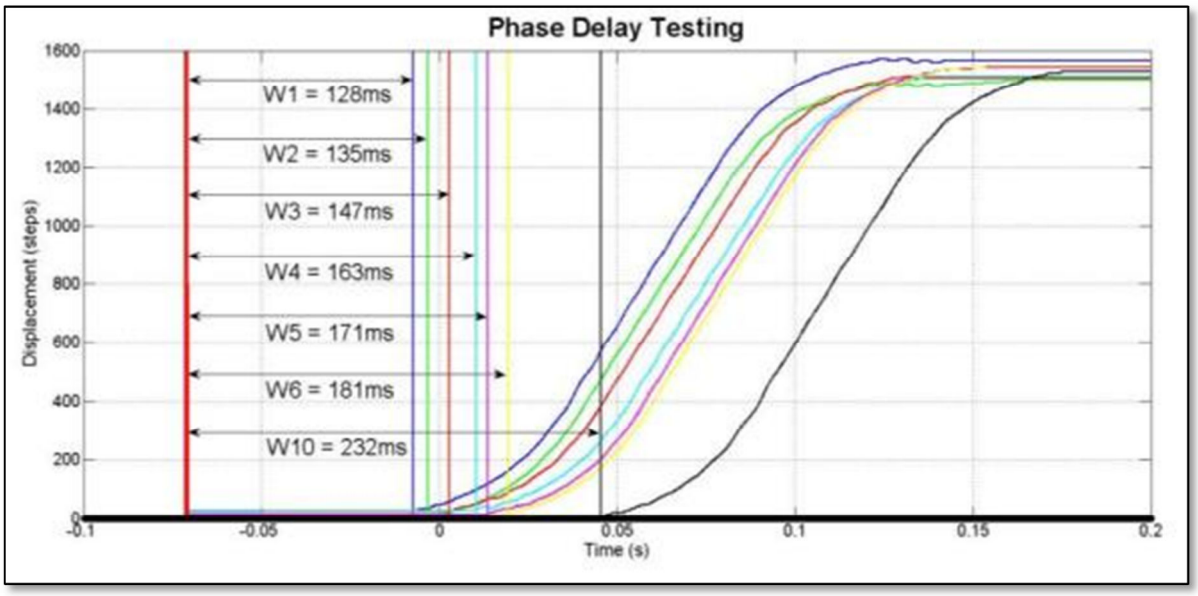

Figure 7.4: Average phase delay between detection and activation

Unfortunately when tested over multiple trigger events the variability of the delay was found to be rather large as shown in Figure 7.5. This could be due to several factors, including variability in detection of the control signal, variability of the delay time within the control code and variability in the activation timing of the motors. The only method of detecting an input signal with the IBC400 is to "loop on port", which means that the controller will wait until it detects a change in the state of a specified pin. Once this is detected the controller jumps to the next piece of code. The "loop on port" function has a sampling period of $2-3\,ms$ and the "wait" command has a specified delay of $10\,ms$. This implies that the most likely cause of this variability is the production of the control signal or the activation of the stepper motors.

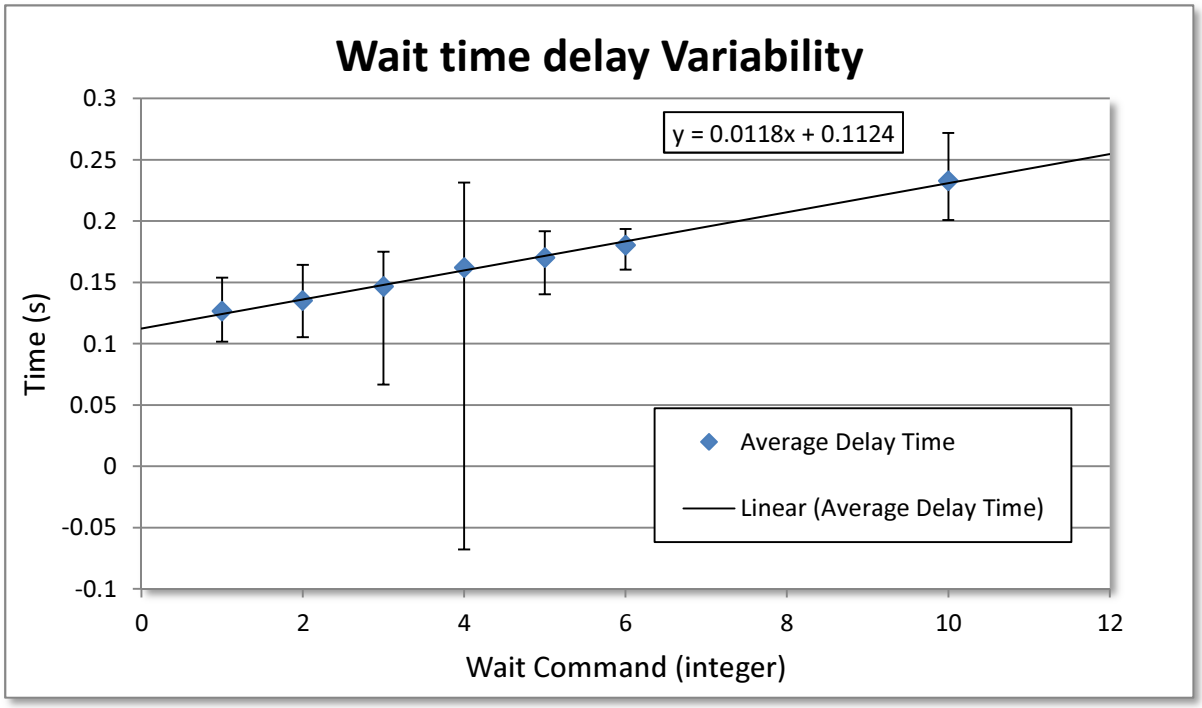

Figure 7.5: Variability in delay between signal detection and stepper motor activation

7.2 Compression Fittings

To pass wires into the pressurised displacer and generator chambers, compression seal fittings were required. A compression seal fitting is used to pass an element such as a wire, pipe or probe through a pressure boundary. The fitting is comprised of several parts as shown in Figure 7.6. These in general consist of the body, seat, sealant, follower and cap. The body is the base of the fitting to which all the other parts are attached. It is fixed to the pressure boundary wall, usually via a threaded connection. The seat fits inside the body and provides a surface for the sealant to compress against. The sealant is a flexible material that is placed around the element to be sealed and is positioned against the seat. The follower is used to compress the sealant from the cap end. The cap is threaded onto the body and wound down, which forces the follower to compress the sealant. This provides an axial force onto the element and stops the pressure differential from moving the element, or the working fluid from escaping around it.

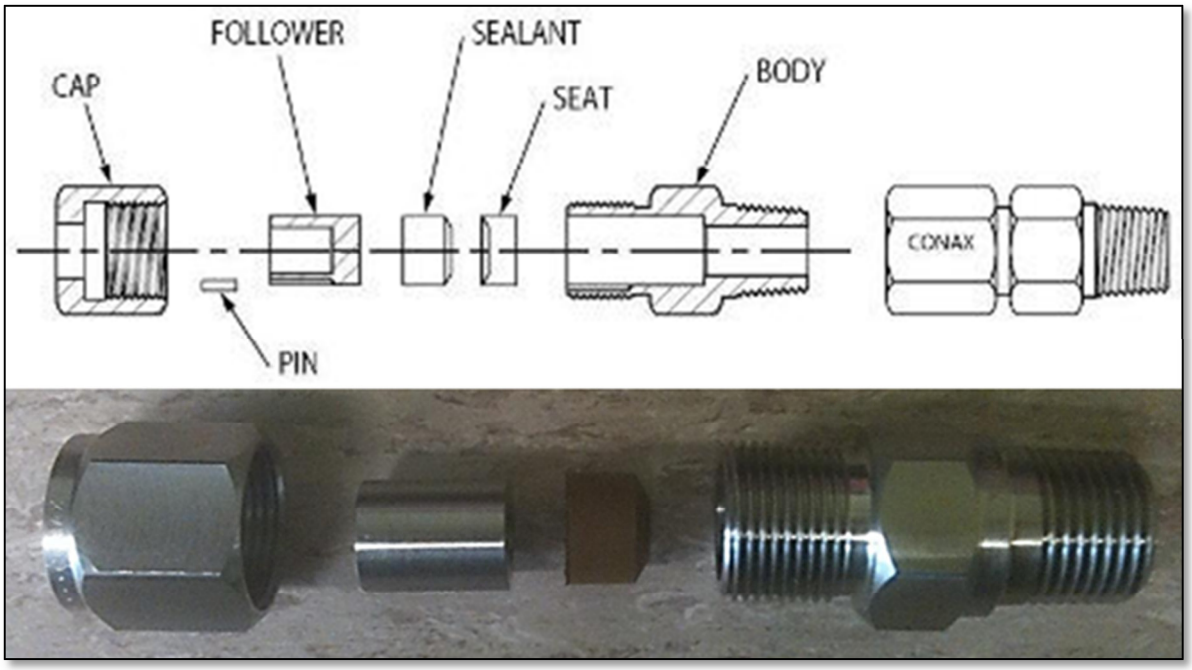

Figure 7.6: Compression fitting components [58]

Several wires and pressure tubes were required to enter the pressure vessels in order to transmit power to the motors and transmit measurements of the engine operating conditions back to a laptop for data collection. After investigation it was found to be more cost effective to use standard single element fittings rather than custom multi element designs. With this in mind the setup in Table 7.1 was developed to minimise cost. This setup consists of 5 compression fittings in the displacer chamber and 2 in the generator chamber. Because the external dimension of the wire passing through the compression fittings is important to create an air tight seal, wire was also specially sourced and ordered as shown in Table 7.2.

Table 7.1: Final set of compression fittings ordered

Displacer chamber					
Feed through #	Compression fitting	Wire type	Number of cores/wires	Outside diameter (mm)	Compression fitting cost (US$)
1 (Temp sense)	PG2-187-A-V	AWG24	Shielded 4	4.8	$29.00
3 (Position sense1)	PG2-187-A-V	AWG24	Shielded 4	4.8	$29.00
4 (limit switches)	PG2-187-A-V	AWG24	Shielded 4	4.8	$29.00
6 (Motor 1 power)	PG5-390-A-V	AWG13	Shielded 4	9.9	$148.00
7 (Motor 2 power)	PG5-390-A-V	AWG13	Shielded 4	9.9	$148.00
Generator chamber					
8 (generator power)	PG4-295-A-V	AWG16	3	7.5	$93.00
9 (position sense2)	PG2-187-A-V	AWG24	Shielded 4	4.8	$29.00
Total cost (US $)					$505

Table 7.2: Wire elements and costs

Displacer chamber					
Feed through #	Wire type	Cable length (m)	Number of cores/wires	Outside diameter (mm)	Cost/m (NZ $)
1 (Temp sense)	K-type thermocouple	1	8 Twisted pairs	1	-
2 (Pressure sense1)	AWG24	2	Shielded 6	5.5	$7.44
3 (Position sense1)	AWG24	2	Shielded 4	4.8	$2.62
4 (limit switches)	AWG24	2	Shielded 4	4.8	$2.62
6 (Motor 1 power)	AWG13	1.5	Shielded 4	9.9	$7.41
7 (Motor 2 power)	AWG13	1.5	Shielded 4	9.9	$7.41
Generator chamber					
8 (generator power)	AWG16	2	3	7.5	$4.26
9 (position sense2)	AWG24	4	Shielded 4	4.8	$2.62

7.3 General Acquisition and Construction

7.3.1 Heat Exchangers

As described in section 2.6.6 Heat Exchangers, the heat exchangers had been constructed and required installing into the displacer chamber. This required holes to be drilled through the bottom plate of the displacer chamber. An electromagnetic drill press was utilised which

provided both stability and accuracy in the confined space. Unfortunately the placement of the holes either coincided with one of the reinforcing struts that prevented the bottom plate from bulging under pressure, or one of the castor wheels used to move the engine around. It was decided to avoid the strengthening strut so as to not compromise the structural integrity of the displacer chamber. Presently two holes have been drilled in order to install one heat exchanger and the castor wheel must be removed in order to complete the installation of the second.

To prevent the space at each end of the heat exchangers becoming dead space, end caps were designed to fill these spaces with insulating material. Firstly $3\,mm$ acrylic was cut into four pieces. The inside and outside pieces were then bent to the inside and outside radius of the heat exchanger. These four pieces were then glued together to form a perimeter the same shape as the exterior dimensions of the heat exchangers, as seen in Figure 7.7. In order to complete the construction closed cell expanding foam should be poured into the void space and either caped with acrylic or cut off level and painted with a sealant.

Figure 7.7: Construction of heat exchanger end caps

7.3.2 Crank Shaft

To complete the crank shaft another thrust bearing is required for the bottom end. The shaft needs to be cut and the crank rods secured to the shaft. The counter balance weights need to be machined and attached.

7.3.3 Power Piston

The power piston is mostly completed however the friction between the piston rings and the cylinder wall is excessive at present. A thinner piston ring may be required and or some lubricant, possibly silicone. Alternatively, some piston rings could be manufactured from Rulon.

7.3.4 Generator

The generator needs to be installed into the generator chamber. A plate has been machined and needs to be welded into place. The generator can then be bolted into place and the crank shaft connected via the 6:1 gearing ratio.

7.3.5 Displacer

A second circular $3\,mm$ polycarbonate insulation panel is still required for the top of the displacer chamber, to provide a thermal barrier between it and the buffer space above. The three pine frames for the displacer have been constructed but the rest of the design still needs completing. The next step is to cut the three ribs that secure the frames in place. The entire frame can then be secured to the central PVC cylinder. Once the depron foam has been sourced it can be glued to the frame completing an air tight structure. Some testing still needs to be completed on the best type of seal to use, once this has been completed the seals can be attached and the displacer installed.

7.3.6 Compression Fittings

The compression fittings and wire have arrived but still require installing. The exact positioning of the compression fittings still needs to be decided on. The best option is probably to evenly distribute them around the top plate to preserve its structural integrity as

much as possible. The fittings are either ½, ¼ or ¾ National Pipe Thread (NPT). To install the fitting holes will have to be drilled and tapped with the appropriate thread.

7.4 DISCUSSION

Unfortunately when tested over multiple trigger events the variability of the delay between activation signal on the crank shaft and movement of the stepper motors was found to be rather large. This could be due to several factors, including variability in the timing of the control signal and variability in the activation timing of the motors. Further investigation is required to determine the exact cause of this variability and a decision made as to what parts of the control system need upgrading.

Presently the only points securing the heat exchangers and the regenerator to the displacer chamber are the four pipes passing through the base plate. Because there will be a sliding seal on the inside radius of these components it may be necessary to provide some method holding these components more rigidly in place. This would prevent any torque applied from the displacer seal putting undue stress on the copper pipes. Ideally this method should not penetrate the insulative barrier of the polypropylene plastic sheet as this would provide a leak in the thermal barrier reducing engine efficiency.

8. DISCUSSION

Currently one of the major areas of concern with respect to a successful testing is the displacer design and actuation system. Currently the central components of the original displacer piston have been retained with a lighter weight frame and skin added. This approach was taken to reduce both cost and time of manufacture. Unfortunately the current design's moment of inertia is still calculated to be just short of the calculated actuation system limit, meaning that the actuation system will have to run at close to 100% capacity to achieve the desired displacement motion. This is likely to cause issues while running the Stirling engine, either by producing an unreliable displacement motion or failing to achieve the engine design frequency. Additionally there are around $2.9\,m$ of sliding seals on the current design whose friction has not yet been included in the loss calculations. If the current design is not capable of achieving the desired operational frequency of 2Hz either the displacer may need to be completely redesigned or the power of the actuation system may need to be increased.

With respect to the regenerator design, one additional factor that was not tested is fringe flow. This is where the wire wool is compressed against the side wall and can create unwanted, lower flow resistance channels for the working fluid to pass through. With more working fluid passing through these channels and not through the wire, the effectiveness of the regenerator can be affected. By adding the extra curved panels into the regenerator design the risk of this occurring is increased. This is due to the larger surface area of the wire wool acrylic boundary. If this phenomenon does become an issue one possible solution is to glue a rough material to the acrylic panels. This should reduce the chance of high flow channels being created by presenting an uneven surface for the wire wool to mesh into. To fully test the regenerator's performance a full scale test rig would be required; alternatively sensors could be placed inside the engine to assess its performance under real world operating conditions.

With the current regenerator design it would be possible to vary the wire diameter in different sections of the regenerator. Introducing variable wire diameters would allow greater

manipulation of the individual sections operational characteristics. A smaller diameter wire would increase the heat transfer area with decreased porosity, while a larger wire diameter would allow a greater thermal capacity with increased porosity. It was decided for ease of simulation, construction and cost to keep the same diameter wire throughout, however this could be reconsidered if the current design does not perform to the desired specifications.

The model developed to simulate the regenerator was only for steady flow and not oscillating flow. This was done for simplicity and also under the assumption that for a low speed engine the pressure drop in the regenerator may be predicted adequately from the correlations developed for steady unidirectional flow [51]. For more accuracy an oscillating flow model could be developed, this may be necessary if the current design does not perform as expected.

Using the TC-08 with all eight probes the maximum sampling rate is one sample per second which somewhat limits the response time of the system. This means that it is only useful for measuring the inlet and outlet temperatures of the heating and cooling fluid or the average temperatures of the hot and cold side of the working fluid. For a more complete engine analysis it would be nice to have a faster response time which would allow analysis of things like working fluid or regenerator temperature variations within a single cycle. If cost was not an issue it would be advantageous to have a complete set of measurement and control systems all integrated within a LabVIEW environment.

Dead space losses can be extremely detrimental to the efficiency of a Stirling engine. The dead space volumes at the top and bottom of each heat exchanger have been minimised with the use of foam caps. There will also be spaces surrounding the regenerator where imperfections in the construction cause working fluid pockets between the regenerator and displacer chamber walls. To eliminate this problem these gaps could be filled with a material such as closed cell foam or resin. It must be considered however that it is desirable that the regenerator is removable so that different packing materials and densities can be tested.

9. CONCLUSIONS

This thesis presents the design and construction of a LTD Stirling engine for power generation. The target power sources were geothermal, industrial waste heat or solar heated water. These sources would supply a source temperature of around 90°C. Assuming that the sink temperature of 20°C, the engine was designed based on a temperature difference of 70°C. The initial design and basic structure of the engine was completed in a previous project utilising first order design methods [14]. The goal was to produce a low cost prototype engine capable of producing up to 500W electrical output. A novel gamma type engine was proposed utilising a rotary displacer and industrial steam piping to form a low cost pressurised chamber. This project concentrated on advancing the design and construction towards completion with particular emphasis on the electrical control and measurement components.

The original displacer and displacer actuation system designed in [14] could not achieve the desired engine frequency of $2\,Hz$. The cause was found to be that the moment of inertia of the displacer was too great for the electric stepper motors to accelerate and decelerate at the required rate. At the completion of this project the displacer actuation system has been redesigned. The displacer's moment of inertia has been decreased by designing a lighter weight frame and skin, while also removing any unnecessary components. Additionally a secondary motor was added to the actuation system to increase its acceleration capability.

The unusual shape of the regenerator in this engine meant that its design was very experimental. In order to produce an even working fluid flow throughout the regenerator, a lot of time was spent designing and testing to try and overcome these shape peculiarities. Once the construction materials were chosen, simulations were developed to optimise the wire mass and number of segment baffles and placement. This process resulted in a curved panel structure capable of producing a relatively even pressure drop over varying regenerator lengths. At the completion of this project the regenerator has been designed, built and installed to the specifications of the simulations.

Because the Stirling engine will not be self-starting a starter motor/generator control system was designed. This system had to provide motive power to get the Stirling engine up to its design speed of $2\,Hz$. The system was designed such that once the Stirling engine was running under its own power, it could switch into generation mode to produce an electrical output from the mechanical power provided. Such a system has been successfully designed, constructed and tested in an external rig to the design specifications of the engine.

The pressure and temperature measurement system designs were updated, constructed and tested to the design specifications of the engine. All pressure transducers are operational and provide the capability to capture and store data in multiple pressure ranges. This information can be used to calculate the power loss associated with the flow losses in the heat exchangers and also the mechanical work produced by the engine. The temperature transducers are operational and capable of measuring and storing data collected from eight different locations. These measurements can subsequently be used to calculate the engine efficiency. They may also be used to measure the working fluid temperature in the compression and expansion spaces, or the temperature variation across the regenerator. These however would be average values as the sampling resolution of the data logger is greater than that of the designed engine period.

Unfortunately completion of the engine assembly was not achieved within the scope of this project and therefore complete engine testing was not carried out. Most of the work that still needs to be completed is general mechanical construction and assembly. This includes crank shaft construction, power piston installation, generator installation, heat exchanger installation, displacer and displacement actuation system installation, compression fittings and measurement system installation.

The limited budget for this project has had an influence on both the quality and duration of the build. In terms of quality, better components such as motor controllers, pressure sensors and temperature sensors could have been used. This would have allowed higher precision both in terms of accuracy of measurements and timing of control signals. The time spent researching low cost options could also have been reduced. For example, when

it was discovered that the stepper motor would not be powerful enough to actuate the displacer it would have been easier to upgrade the motors rather than redesign the displacer, however this would have been a much more expensive option so it was discounted. Because the stepper motor controller was an older model a lot of time as spent finding workarounds for programming and control issues, this could have been eliminated by purchasing a more modern controller. A more advanced control and measurement system could have been implemented, such as a LabVIEW system. This way control and measurement of all systems could be collected and controlled in a single software package. This would allow higher precision both in terms of accuracy of measurements and timing of control signals.

With the advances in computing over the past decade developing and running Stirling engine simulations is no longer such a costly or time consuming task. It is would possibly be both more cost and time effective to develop a computer model and run simulations to assess whether the engine has any potential.

REFERENCES

[1] T.F. Stocker, D. Qin, G.K. Plattner, M.Tignor, S.K. Allen, J. Boschung, A. Nauels, Y. Xia, et al, "IPCC, 2013: Summary for Policymakers. In: Climate Change 2013: The Physical Science Basis. Contribution of Working Group I to the Fifth Assessment Report of the Intergovernmental Panel on Climate Change," Cambridge University Press, Cambridge, United Kingdom and New York, NY, USA..

[2] Bindoff, Nathaniel L. Stot, Peter A. AchutaRao, Krishna Mirle Allen, Myles R. Gillett, Nathan Gutzler, David Hansingo, Kabumbwe Hegerl, Gabriele; Hu, Yongyun Jain, Suman Mokhov, Igor I. Overland, James JudithPerlwitz Sebbari, Rachid Zhang, et al, "Climate Change 2013, The Phyusical Science Basis. Chapter 10, Detection and Attribution of Climate Change: from Global to Regional," IPCC, 2013.

[3] B Gabriel, K A Alfred, et al, "Climate Change 2014, Working Group III – Mitigation of Climate Change, Chapter 5," IPCC, Worldwide Scientific Collaboration, 2014.

[4] A.B Igor, et al, "Climate Change 2014, Working Group III – Mitigation of Climate Change, Chapter 7 Energy Systems," IPCC, World Wide Colaboration, 2014.

[5] Valgardur Stefansson , "World Geothermal Assessment," World Geothermal Congress , Reykjavik, Iceland , April 2005 .

[6] "Carbon Neutral," The Carbon Neutral Company, 2012. [Online]. Available: http://www.carbonneutral.com/interface/files/projects/Geothermal_energy_overview.pdf. [Accessed 13 2 2015].

[7] F. S. Janet L. Sawin, " Renewables 2014 Global Status Report," REN21 Secretariat, Paris, 2014.

[8] L. L. Felicito Gazo, "Low Enthalpy Geothermal Energy - Technical Review," GNS Science, Taupo, 2010.

[9] Ahmed Elsayed, Mebrahtu Embaye, Raya AL-Dadah, Saad Mahmoud, Ahmed Rezk, "Thermodynamic performance of Kalina cycle system 11 (KCS11): feasibility of using alternative zeotropic mixtures," Oxford University Press, 2013.

[10] H. M. Sadiq J. Zarrouka, "Efficiency of geothermal power plants: A worldwide review," Elsevier Ltd, 2013.

[11] “Renewable Energy Essentials: Geothermal,” International Energy Agency, 2010.

[12] C. D. Fitzgerald, “AN ECONOMIC EVALUATION OF BINARY CYCLE GEOTHERMAL ELECTRICITY PRODUCTION,” Air Force Institute of Technology , Ohio , 2003 .

[13] B. Hoegel, “THERMODYNAMICS-BASED DESIGN OF STIRLING ENGINES FOR LOW-TEMPERATURE HEAT SOURCES,” University of Canterbury, Christchurch, 2014.

[14] Caleb C Lloyd, “A LOW TEMPERATURE DIFFERENTIAL STIRLING ENGINE FOR POWER GENERATION,” University of Canterbury, Christchurch, 2009.

[15] “Wikipedia: External combustion engine,” Wikimedia Foundation, Inc., 5 January 2015. [Online]. Available: http://en.wikipedia.org/wiki/External_combustion_engine. [Accessed 15 2 2015].

[16] “Wikipedia: Compression seal fitting,” [Online]. Available: http://en.wikipedia.org/wiki/Compression_seal_fitting. [Accessed 29 April 2013].

[17] C. S. Vineeth, Stirling Engines: A Beginners Guide, 2012.

[18] C.M.Hargreaves, in *The Phillips Stirling Engine*, Eindhoven, Elsevier Science Publishering Company inc, 1991, p. 457.

[19] G. Walker, Stirling-cycle machines, Oxford: Claredon Press, 1973.

[20] “Wikipedia: Stirling engine,” Wikimedia Foundation, Inc., 14 January 2015. [Online]. Available: http://en.wikipedia.org/wiki/Stirling_engine#Functional_description. [Accessed 15 2 2015].

[21] M. Keveney, “Animated Engines,” Animated Engines, 2011. [Online]. Available: http://www.animatedengines.com/vstirling.html. [Accessed 15 2 2015].

[22] M. Keveney, “Animated Engines,” Animated Engines, 2011. [Online]. Available: http://www.animatedengines.com/stirling.html. [Accessed 15 2 2015].

[23] M. Keveney, “Animated Engines,” Animated Engines, 2011. [Online]. Available: http://www.animatedengines.com/ltdstirling.html. [Accessed 15 2 2015].

[24] D. Haywood, “AN INTRODUCTION TO STIRLING-CYCLE MACHINES,” Cambridge University, 2007.

[25] “Wikipedia: Thermodynamic cycle,” Wikimedia Foundation inc, 2013. [Online]. Available: http://en.wikipedia.org/wiki/Thermodynamic_cycle. [Accessed 14 June 2013].

[26] “Wikipedia: Carnot's theorem,” Wikimedia Foundation, Inc., 5 February 2015. [Online]. Available: http://en.wikipedia.org/wiki/Carnot%27s_theorem_(thermodynamics). [Accessed 15 2 2015].

[27] “Wikipedia: Beale number,” Wikimedia Foundation, Inc., 19 December 2013. [Online]. Available: http://en.wikipedia.org/wiki/Beale_number. [Accessed 15 2 2015].

[28] “Wikipedia, Beale number,” Wikimedia Foundation, Inc., 19 December 2013. [Online]. Available: http://en.wikipedia.org/wiki/Beale_number. [Accessed 15 December 2014].

[29] B. Kongtragool and S. Wongwises, “Investigation on power output of the gamma-configuration low temperature differential Stirling engines,” Renewable Energy, Bangkok, 2004.

[30] K. Kraitong, “Numerical Modelling and Design Optimisation of Stirling Engines for Power Production,” Doctoral thesis, Northumbria University, 2012.

[31] P. Fette, “A Twice Double Acting a - Type Stirling Engine Able to Work with Compound Fluids Using Heat Energy of Low to Medium Temperatures.,” 19 February 2010. [Online]. Available: http://www.stirling-fette.de/english.htm. [Accessed 16 2 2015].

[32] “ Saitama University,” [Online]. Available: http://www.bekkoame.ne.jp/~khirata/academic/kiriki/yama1/index.html. [Accessed 4 March 2013].

[33] I. Kolin, Stirling Motor, History - Theory - Practice., Dubrovnik: Zagreb University Publications, LTD., 1991.

[34] P. Pavlinovich, “Steam and Engine of Australia,” 02 October 2009. [Online]. Available: http://www.steamengine.com.au/index.php/stirling/models/91-a-low-temperature-stirling-engine-by-penn-clower. [Accessed 22 08 2014].

[35] I. F. Iwamoto, K. Toda, M. Hirata, Takeuchi and T. Yamamoto, “Comparison of

low- and high temperature differential Stirling engines," National Institute for Research and Environment, Japan, 1997.

[36] "Sunvention," [Online]. Available: http://www.bsrsolar.com/sv/produkte3_e.html. [Accessed 27 March 2013].

[37] D. Conner, "Solar heat engines," 10 January 2012. [Online]. Available: http://www.solarheatengines.com/2012/01/10/tamera-video-of-sunvention-sunpulse-engine. [Accessed 3 April 2013].

[38] "Suction," 5 September 2012. [Online]. Available: http://www.suction.co.jp/stirling/ya2.html. [Accessed 2 April 2013].

[39] Cool Energy, "Cool Energy," Cool Energy, Inc., 2014. [Online]. Available: http://coolenergy.com/. [Accessed 24 November 2014].

[40] "Youtube," 13 9 2011. [Online]. Available: http://www.youtube.com/watch?v=D3JMsm7Q8LQ. [Accessed 27 5 2013].

[41] Vinod Kumar Gopal, Dr. Richard Duke, Dr. Don Clucas, "Active Stirling Engine," IEEE, Christchurch, 2009.

[42] "Depron Foam," 2012. [Online]. Available: http://www.depronfoam.com/index.html. [Accessed 22 1 2015].

[43] M. B.Ibrahim and J. Roy C.Tew, Stirling Converter Regenerators, USA: CRC press, 2012.

[44] B. K Mansoor, Investigations With A Small Air Charged Stirling Engine, Yorkshire: The British Library, 1984.

[45] G. Trivella, T. Belforte, V. Raparelli, A. Viktorov, "Permeability and Inertial Coefficients of Porous Media for Air Bearing Feeding Systems," *Journal of Tribology*, vol. 129, pp. 705 - 711, 2007.

[46] R. G. ZHENGWEN ZENG, "A Criterion for Non-Darcy Flowin Porous Media," Petroleum Recovery Research Center, New Mexico Institute of Mining and Technology, Socorro, 2005.

[47] "Wikipedia: Darcy's law," Wikimedia Foundation, Inc., 17 January 2015. [Online]. Available: http://en.wikipedia.org/wiki/Darcy's_law#Darcy.27s_Law_for_Gases_in_Fine_Media_.28K

nudsen_Diffusion_or_Klinkenberg_Effect.29. [Accessed 26 January 2015].

[48] Aydin Nabovati, Edward W. Llewellin, Antonio C.M. Sousa, "A general model for the permeability of fibrous porous media based on fluid flow simulations using the lattice Boltzmann method," *Composites,* vol. Part A 40, p. 860–869, 2009.

[49] G Belforte, T Raparelli, V Viktorov, A Trivella, "Permeability and Inertial Coefficients of Porous Media for Air Bearing Feeding Systems," *Journal of Tribology,* vol. 129, pp. 705-711, 2007.

[50] "Ohio University," Russ College of Engineering and Technology, 5 June 2010. [Online]. Available: http://www.ohio.edu/mechanical/stirling/simple/regen_simple.html. [Accessed 11 2 2015].

[51] Norbert C. J. Chen, Fred P Griffin, "Effects of Pressure-Drop Corrilations on Stirling Engine Predicted Performance," Oak Ridge National Laboratory, Tennessee, 1983.

[52] "Wikipedia: Beta transformation," Wikimedia Foundation, 29 08 2013. [Online]. Available: http://en.wikipedia.org/wiki/Alpha%E2%80%93beta_transformation. [Accessed 21 10 2013].

[53] "Wikipedia: s transformation," Wikimedia Foundation, 23 Aug 2013. [Online]. Available: http://en.wikipedia.org/wiki/Dqo_transformation#Park.27s_transformation. [Accessed 22 Oct 2013].

[54] S. Partyka, "DC Link Voltage Control," Aalborg University, Aalborg, 2008.

[55] Ramla Gheith, Fethi Aloui, Mohand Tazerout, Sassi Ben Nasrallah, "Experimental investigations of a gamma Stirling engine," John Wiley & Sons, Ltd, Nantes, 2011.

[56] "Thermometrics Precision Temperature Sensors," Thermometrics Corporation, 2013. [Online]. Available: http://www.thermometricscorp.com/thertypk.html. [Accessed 04 09 2014].

[57] F. Normani, "Stirling Engine Manual," real-world-physics-problems, 2013.

[58] "Wikipedia: Compression seal fitting," Wikimedia Foundation, Inc., 25 February 2013. [Online]. Available: http://en.wikipedia.org/wiki/Compression_seal_fitting. [Accessed 25 08 2014].

10. APPENDICES

10.1 REGENERATOR MODEL MATLAB CODE

```
function [t,ns,Cm,u,Cp,Cw,P] = initalise_operational_parameters()

%period (s)
t = 0.25;
%revolutions per second (Hz)
ns = 2;
%heat capacity of the steel (J/kg degC)
Cm = 437;
%dynamic viscosity of air at 10bar
u = 0.0000185;
%specific heat capacity of air at 10bar (J/Kg K)
Cp = 1000;
%friiction factor
Cw = 0.4;
%density of air at 1Mpa
P = 12;

end

function [Wm_total,Wd,WD,Rw,Rh,Ro,Ri,Npr,Ve,Vc] =
initalise_physical_parameters()
% initalises physical parameters of stirling engine

%wire mass total(kg)
Wm_total = 5;
%wire diamiter(m)
%Wd = 0.000005;
Wd = 0.00003;
%Wd = 0.00005;
%wire density (kg/m^3)
WD = 7800;
%regenerator width (m)
Rw = 0.3;
%regenerator height (m)
Rh = 0.806;
%outside radiius (mm)
Ro = 392;
%inside radius (mm)
Ri = 93;
%Prandtl number (diimensionless)
Npr = 0.7;
%expansion volume (m^3)
Ve = 0.005;
%compression volume (m^3)
Vc =0.083;

End

clear all
close all
format long

[Wm,Wd,WD,Rw,Rh,Ro,Ri,Npr,Ve,Vc] = initalise_physical_parameters();
[t,ns,Cm,u,Cp,Cw,P] = initalise_operational_parameters();
```

```
    num_segments_vec = [5];
    plot_vec = num_segments_vec - 1;
    num_segments_vec_len = length(num_segments_vec);
    num_segments_vector = zeros(1,num_segments_vec_len);
    Nreg_set_vec = 1:100;
    Nreg_set_vec_len = length(Nreg_set_vec);
    Nreg_vec = zeros(1,num_segments_vec_len);
    Ploss_vec = zeros(1,num_segments_vec_len);
    Nreg_set = 30;

for zz = 1:num_segments_vec_len
    num_segments = num_segments_vec(zz);
    Wm = [0.31 0.65 1.33 2.74];
    Wd = zeros(1,(num_segments-1));
    Mf_new = zeros(1,(num_segments-1));
    wire_diamiter_seg_new = zeros(1,num_segments);
    wire_mass_seg_new = Wm;
    step = 0.01;
    count = 1;
    seg_radius = zeros(1,num_segments);
    Ploss_max = 700;
    Nreg_min = 20;
    mass_flow_increment = 0.0001;
    max_count = 10000;
    max_wire_mass = 4.96;
    seg_radius(1) = 93;
    segment_width = [0 0 0 0];

    for rr = 1:(num_segments-1)
        Wd(rr) = 0.0001;
        wire_diamiter_seg_new(rr) = 0.0001;
        seg_radius(rr+1) = (93+(((392-93)/((num_segments-1)))*(rr)));
    end

    while count < max_count

        arc_length = 40*pi/180.*seg_radius;
        for jj = 1:(num_segments-1)

            %mass of gas that flows through regenerator segment every half
cycle (kg)
            if (count == 1)
                Mf(jj) = ((((pi*(seg_radius(jj+1)/1000)^2)-
(pi*(seg_radius(jj)/1000)^2))*Rh*(1/3))*P);
            end
            %Mass flow rate (kg/s)
            M(jj) = 2*ns*Mf(jj);
            %volume of regenerator segment (m^3)
            Vreg(jj) =(((pi*(seg_radius(jj+1)/1000)^2)-
(pi*(seg_radius(jj)/1000)^2))*Rh*(1/9));
            %segment width (mm)
            segment_width(jj) = seg_radius(jj+1)-seg_radius(jj);%(Ro-
Ri)/num_segments;
            %cross sectional area (m^2)
            Ra(jj) = (segment_width(jj)/1000)*Rh;
            %regenerator porosity
            E(jj) = 1-(Wm(jj)/(WD*Vreg(jj)));
            %free flow area (m^2)
```

```
            Aff(jj) = E(jj)*Ra(jj);
            %Mass flow rate per unit area
            Mo(jj) = M(jj)/Aff(jj);
            %regenerator heat transfer surface area (m^2)
            Sreg(jj) = 4*((1-E(jj))/E(jj))*Vreg(jj)/Wd(jj);
            %hydrolic diiamiiter (m)
            dh(jj) = 4*Vreg(jj)/Sreg(jj);
            %Reynolds number
            Nre(jj) = Mo(jj)*dh(jj)/u;
            %for E = 0.95
            Y3(jj) = 2.75*Nre(jj)^-0.48;
            %convective heat transfer coefficiient
            h(jj) = Y3(jj)*Cp*M(jj)*Npr^-(2/3);
            %number transfer units
            NTU(jj) = (h(jj)*Sreg(jj))/(M(jj)*Cp);
            %reduced length
            A(jj) = NTU(jj);
            %regenerator effectiveness (%)
            Nreg(jj) = (NTU(jj)/(NTU(jj)+2))*100;
            %redused period
            H(jj) =(h(jj)*Sreg(jj)*t)/(Wm(jj)*Cm);
            %Tmax
            TH = 90;
            %Tmin
            TC = 20;
            %temperature ratio
            temp_ratio = TC/TH;
            Cv = 718;
            %compression ratio
            rv = 1.06;
            %engine efficiency
            engine_efficiency(jj) = ((Nreg(jj)*(1-temp_ratio))+(((Cp/Cv)-
temp_ratio)*log(rv)))/((Nreg(jj)*(1-temp_ratio))+(((Cp/Cv)-1)*log(rv))) ;

    %%%%%%%%%%%%%%%%%% Pumpiing losses
%%%%%%%%%%%%%%%%%%%%%%%%%%%%%%%%%%%%%%%%%%%%

            %arc length (mm)
            %La = 40*pi/180*seg_radius(;
            %regenerator length max (m)
            Lmax = arc_length(jj+1)/1000;
            %regenerator length min (m)
            Lmin = arc_length(jj)/1000;
            dL = (Lmax-Lmin)/100;%0.001;
            L = (Lmin:dL:Lmax);
            %regenerator length min (m)
            %L = ((Lmax+Lmin)/2);

            %hydrauliic radius
            hr(jj) = dh(jj)/4;

            c = [1.94E-02 1.64E-02 1.31E-02 1.02E-02];
            C1 = 0.491;
            C2 = 2.31;
            phi_c = 0.0743;
            K(jj) = (C1*(sqrt((1-phi_c)/(1-E(jj))))^C2)*(Wd(jj)/2)^2;

            air_speed_seg(jj) = M(jj)/(P*Ra(jj));

            for ii = 1:length(L)
```

```
                %darcy-forechiemer pressure difference (mmHg)
                delP(ii,jj) =
((((u*air_speed_seg(jj))/K(jj))+((c(jj)*(P*air_speed_seg(jj)^2)/K(jj)^0.5))
)*L(ii))*0.0075006168;

                % pressure diifference (Pa)
                % delP(ii,jj) = (Mo(jj)^2*Cw*L(ii))/(2*hr(jj)*P);
                delP_Pa = delP./0.0075006168;
                %power loss
                Ploss(ii,jj) = 2*ns*delP_Pa(ii,jj)*Ve;

            end

            pressure_span(jj) = Ploss(end,jj)-Ploss(1,jj);
            pressure_span_average = mean(pressure_span);
            Ploss_means(jj) = mean(Ploss(:,jj));


%%%%%%%%%%%%%%%%%%%%%%%%%%%%%%%%%%%%%%%%%%%%%%%%%%%%%%%%%%%%%%%%%%%%%%%%%%%%%%%

    %%%%%%%%%%%%function to equilise mass flow rate based on pressure
loss%%%%%

            Ploss_means;
            Ploss_avg = mean(Ploss_means);
            Ploss_total = sum(Ploss_means);
            Mf_total = sum(Mf);

            if (mean(Ploss(:,jj)) >= Ploss_avg)
                %Mf_new(jj) = Mf(jj)- mass_flow_increment;
                Wm(jj) = Wm(jj)-0.01;
            elseif (mean(Ploss(:,jj)) < Ploss_avg)
               % Mf_new(jj) = Mf(jj)+ mass_flow_increment;
               Wm(jj) = Wm(jj)+0.01;
            else
                Mf_new = Mf;
            end
            if (sum(Wm) >= max_wire_mass)
                Wm(jj) = Wm(jj)-0.008;
            end
            if (sum(Wm) <= max_wire_mass)
                Wm(jj) = Wm(jj)+0.008;
            end


%%%%%%%%%%%%%%%%%%%%%%%%%%%%%%%%%%%%%%%%%%%%%%%%%%%%%%%%%%%%%%%%%%%%%%%%%%%%%%%

            if count == 1
                figure(1)
                %subplot(3,1,1),
                subplot(3,1,1),plot(L,delP(:,jj), 'b-', 'linewidth',2)
                grid on
                xlabel('Length (m)')
                ylabel('pressure drop (mmHg)')
                hold on
                subplot(3,1,2), plot(L,Mf(jj), 'b-', 'linewidth',2)
                grid on
```

```
                xlabel('Length (m)')
                ylabel('mass flow rate (Kg)')
                hold on
                subplot(3,1,3), plot(L,Wm(jj), 'k-', 'linewidth',2)
                xlabel('regenerator length (m)','FontSize',16)
                ylabel('wire mass (kg)','FontSize',16)
                zoom xon
                grid on
                hold on

            elseif count == max_count-1
                figure(2)
                subplot(3,1,1),plot(L,delP(:,jj), 'b-', 'linewidth',2)
                grid on
                xlabel('regenerator length(m)','FontSize',12)
                ylabel('pressure drop (mmHg)','FontSize',12)
                hold on
                subplot(3,1,2), plot(L,Mf(jj), 'b-', 'linewidth',2)
                grid on
                xlabel('Length (m)')
                ylabel('mass flow rate (Kg)')
                hold on
                subplot(3,1,3), plot(L,Wm(jj), 'k-', 'linewidth',2)
                xlabel('regenerator length (m)','FontSize',16)
                ylabel('wire mass (kg)','FontSize',16)
                zoom xon
                grid on
                hold on

            end

        end

        Mf_total_new = sum(Mf_new);

        if (Mf_total_new < Mf_total)
            Mf_new = Mf_new + (Mf_total - Mf_total_new)/(num_segments-1);
        elseif (Mf_total_new > Mf_total)
            Mf_new = Mf_new - (Mf_total_new - Mf_total)/(num_segments-1);
        end

        Mf = Mf_new;

%%%%%%%%% equilise Nreg by altering wire mass %%%%%%%%%

%         wire_mass_total = sum(Wm);
%         Nreg_avg = mean(Nreg);
%
%         for gg = 1:num_segments-1
%             if (Nreg(gg) <= Nreg_avg)
%                 if (wire_mass_total <= max_wire_mass)
%                     wire_mass_seg_new(gg) = Wm(gg)+0.01;
%                 end
%             elseif (Nreg(gg) > Nreg_avg)
%                 if (Wm(gg)>= 0)
%                     if (wire_mass_total >= 4.96)
%                         wire_mass_seg_new(gg) = Wm(gg)-0.01;
%                     end
%                 end
%             end
```

```
% %              if Ploss_total >= Ploss_max
% %                  wire_mass_seg_new(gg) = Wm(gg)-0.1;
% %              elseif Ploss_total <= Ploss_max
% %                      if (wire_mass_total <= 7)
% %                  wire_mass_seg_new(gg) = Wm(gg)+0.1;
% %                      end
% %                  end
%
%          Wm = wire_mass_seg_new;
%          end

%%%%%%%%%%%%%%%%%%%%%%%%%%%%%%%%%%%%%%%%%%%%%%%%%%%%%%%%%%%%%%%%%%%%%%%%%%%

% % % % %     %%%%%%%%%%% equilise effectiveness by altering wire mass
%%%%%%%%%%
% % % %
%          wire_mass_total = sum(Wm);
%          Nreg_avg = mean(Nreg);
%          Nreg_total = sum(Nreg);
%
%          for gg = 1:num_segments-1
%              if (Nreg(gg) <= 30)
%                  if (wire_mass_total <= max_wire_mass)
%                      wire_mass_seg_new(gg) = Wm(gg)+0.01;
%                  end
%              elseif (Nreg(gg) > 30)
%                      wire_mass_seg_new(gg) = Wm(gg)-0.01;
%              end
%          Wm = wire_mass_seg_new;
%          end
%%%%%%%%%%%%%%%%%%%%%%%%%%%%%%%%%%%%%%%%%%%%%%%%%%%%%%%%%%%%%%%%%%%%%%%%%%%

    %%%%%%%%% equilise effectiveness by altering wire diamiter %%%%%%%
%
%          Nreg_avg = mean(Nreg);
%          Nreg_total = sum(Nreg);
%
%          for ll = 1:num_segments-1
%          if (Nreg(ll) <= Nreg_avg)
%              if (Wm >= 0.1)
%                  wire_diamiter_seg_new(ll) = Wd(ll)-0.1;
%              end
%          else if (Nreg(ll) > Nreg_avg)
%                  wire_diamiter_seg_new(ll) = Wd(ll)+0.1;
%              end
%          end
%      %     if Nreg(ll) > Nreg_min
%      %         %wire_diamiter_seg_new(ll) = Wd(ll)-0.1;
%      %     else if Nreg(ll)<= Nreg_min
%      %             wire_diamiter_seg_new(ll) = Wd(ll)+0.000001;
%      %         end
%      %     end
%
%      Wd = wire_diamiter_seg_new;
%      end
%
%%%%%%%%%%%%%%%%%%%%%%%%%%%%%%%%%%%%%%%%%%%%%%%%%%%%%%%%%%%%%%%%%%%%%%%%%%%

%%%%%%% equilise pressure span by altering segment width %%%%%%%%
```

```
        for kk = 1:num_segments-2
            if pressure_span(kk) >= pressure_span_average
                if seg_radius(2)-seg_radius(1) >= 30
                    seg_radius(kk+1) = seg_radius(kk+1)-step;
                end
            elseif pressure_span(kk) < pressure_span_average
                seg_radius(kk+1) = seg_radius(kk+1)+step;
            end
        end
        if (num_segments >= 4)
            if pressure_span(num_segments-2) >= pressure_span_average
                seg_radius(kk-1) = seg_radius(kk-1)+step;
            else
                seg_radius(kk-1) = seg_radius(kk-1)-step;
            end
        end
    seg_radius(1) = 93;
    seg_radius;


%%%%%%%%%%%%%%%%%%%%%%%%%%%%%%%%%%%%%%%%%%%%%%%%%%%%%%%%%%%%%%%%%%%%%%%%%%%%
        count = count+1;
    end
 Wm = [0.68 0.97 1.40 1.90];

end
```

10.2 STEPPER MOTOR CODE

The following code was used to test the link between the detection of the shaft position and rotate the displacer accordingly.

```
########## General ###############
# used to access the code file in cygwin
# cd/cygdrive/c/users/pap40/documents/2013/"stepper motor"/"code files"
# sed command used to compile code
# sed -e '/#/g' -e '/^$/d' -e 's/$/^M/' input.txt >> output.txt
#(to get ^M for line above type CTRL+V followed by CTRL+M)
##############################
#########setup initial conditions##########
# Divide step rates Divider (1-255) (default= 4)
D 3
# set Settle delay 5-255 (time *.01 sec)
#E 100
# Initial SPS SPS (0, 56 to 65,535)SPS
I 6000
# set ramp accerleration/deceleration 0-255
K 2 2
# set Slew speed SPS (56- 65,535) (default= 10,000)
V 50000
# Options (a, d)
```

```
I 8
# display position
#Z 1
#########encoder setup###########
# Set Deadband and Enable
d 10
# Set Line Count (Enable Encoder)e0 = off
e 500
# e 0
# Motor Resolution
h 2000
# Set Stall Retry Count
r 5
# Sampling Distance
s 10
# Stall Tolerance (0-100%)
t 10
# Hunt Velocity
v 2
# Hunt Timeout Fault (seconds) 0 = disable
w 0
# Hunt Distance Fault (steps) 0 = disable
x 0
########### code ##############
# start programming
P 0
# find home (speed, direction) pin 8
F 1000 1
# Wait until complete
W 0
# soft stop
@
# Set origin
O 0
# set direction flag to clockwise
A 0
# loop until port 2 goes high
L 13 3
# wait
# =10x+60ms delay
# 10rpm = W 10
# 20rpm = W 10
# 30rpm = W 3
# 40rpm = W 1
# W 1
```

```
# branch based on ports
g 0 1
P
########[branch code for input ports]##########
#____________(port 1,2,3 = 0,0,0)_________
# enter programming mode
P 256
W 20
# move 120 degrees clockwise
R 0
# Wait until complete
#W 0
# @
# Correct position using optocoupler data
# y
#set direction flag to clockwise
#A 8
# Rotate to CCW endpoint
G 13 1
P
#_____________________________________________

#____________(port 1,2,3 = 1,0,0)__________
# enter programming mode
P 272
W 20
# move 120 degrees clockwise
R 1333
# Wait until complete
# W 0
# @
# correct position using optocoupler data
# y

#set direction flag to clockwise
#A 8
# Goto 13
G 13 1
P
#_____________________________________________

#____________(port 1,2,3 = 0,1,0)__________
# enter programming mode
P 288
W 20
```

```
# move 120 degrees clockwise
R 0
# Wait until complete
# W 0
# @
# correct position using optocoupler data
# y
#set direction flag to clockwise
#A 8
# Goto 13
G 13 1
P
#_____________________________________________

#___________(port 1,2,3 = 1,1,0)_________
# enter programming mode
P 304
#W 0
# move 120 degrees clockwise
R 1333
# Wait until complete
#W 0
# @
# correct position using optocoupler data
# y
#set direction flag to clockwise
#A 8
# Goto 11
G 13 1
P
#_____________________________________________

#___________(port 1,2,3 = 0,0,1)_________
# enter programming mode
P 320
# Goto 13
G 100 1
P
#_____________________________________________

#___________(port 1,2,3 = 1,0,1)_________
# enter programming mode
P 336
# Rotate to CCW endpoint
G 100 1
```

```
P
#_____________________________________________

#___________(port 1,2,3 = 0,1,1)_____________
# enter programming mode
P 352
# Goto 13
G 100 1
P
#_____________________________________________

#___________(port 1,2,3 = 1,1,1)_____________
# enter programming mode
P 368
# Goto 112
G 100 1
P
#_____________________________________________

P 384
G 368 1
P
P448
G 320 1
P
P464
G 336 1
P
P480
G 352 1
P
P496
G 336 1
P
###############[End of go branch code]###############
```

10.3 INVERTER CODE

There is too much code for the FOC inverter to put it all in the appendices. The following is the definition of the parameters for the generator used in this project.

```
/*====================================================================
File name  : HVPM_Sensorless-Settings.h
Description: Incremental Build Level control file.
```

```
==========================================================================*/
#ifndef  PROJ_SETTINGS_H

//Following is the list of the Build Level choices.
#define  LEVEL1  1    // Module check out (do not connect the motors)
#define  LEVEL2  2    // Verify ADC, park/clarke, calibrate the offset
#define  LEVEL3  3    // Verify closed current loop and PIDs and speed measurement
#define  LEVEL4  4    // Verify speed estimation and rotor position est.
#define  LEVEL5  5    // Verify close speed loop and speed PID
#define  LEVEL6  6    // Verify close speed loop sensorless

#define  BUILDLEVEL  LEVEL6
#ifndef  BUILDLEVEL
#error   Critical: BUILDLEVEL must be defined !!
#endif   // BUILDLEVEL
//--------------------------------------------------------------------------

#ifndef  TRUE
#define  FALSE  0
#define  TRUE   1
#endif
#define  PI  3.14159265358979

// Define the system frequency (MHz)
#if (DSP2803x_DEVICE_H==1)
#define  SYSTEM_FREQUENCY  60
#elif (DSP2833x_DEVICE_H==1)
#define  SYSTEM_FREQUENCY  150
#endif

// Define system Math Type
// Select Floating Math Type for 2833x
// Select IQ Math Type for 2803x
#if (DSP2803x_DEVICE_H==1)
#define  MATH_TYPE  0
#elif (DSP2833x_DEVICE_H==1)
#define  MATH_TYPE  1
#endif
// Define the ISR frequency (kHz)
#define  ISR_FREQUENCY  10

// Define the electrical motor parametes (Estun Servomotor)
#define  RS   0.693          // Stator resistance (ohm)
#define  RR                  // Rotor resistance (ohm)
#define  LS   0.004539       // Stator inductance (H)
```

```
#define LR    0.004539      // Rotor inductance (H)
#define LM                  // Magnatizing inductance (H)
#define POLES       10      // Number of poles

// Define the base quantites
#define BASE_VOLTAGE     236.14 // Base peak phase voltage Vdc/sqrt(3)
#define BASE_CURRENT     15     // Base peak phase current,
#define BASE_TORQUE             // Base torque (N.m)
#define BASE_FLUX               // Base flux linkage (volt.sec/rad)
#define BASE_FREQ        200    // Base electrical frequency (Hz)
#endif
```